

Symmetry, Invariant Manifolds and Flow Reversals in Active Nematic Turbulence

Ángel Naranjo,¹ Rumayel Pallock,¹ Caleb Wagner,² and Piyush Grover^{1,*}

¹*Department of Mechanical and Materials Engineering,
University of Nebraska–Lincoln, Lincoln, NE 68588, USA*

²*Parsons Corporation, USA*

(Dated: March 13, 2026)

We investigate how symmetry, exact coherent structures (ECSs), and their invariant manifolds organize spontaneous flow reversals in a 2D active nematic confined to a periodic channel. In minimal flow units commensurate with the intrinsic active vortex scale, we use equivariant bifurcation theory to trace the origin of dynamically relevant ECSs via a sequence of symmetry-constrained local and global bifurcations. At low activity level, we identify relative periodic orbits, created via a sequence of SNIPER, homoclinic and heteroclinic bifurcations, whose invariant manifolds provide robust heteroclinic pathways between left- and right-flowing nearly uniaxial states. These result in several symmetry-dictated reversal mechanisms in the preturbulent regime, with and without vortex-lattice intermediate states. In the active turbulent regime, this ECS skeleton persists and organizes chaotic attractors exhibiting persistent two-way reversals. By classifying ECSs through their symmetry signatures, we relate a small set of ECSs embedded in turbulence back to the preturbulent branches, and show that typical turbulent trajectories repeatedly shadow these ECSs and their unstable manifolds, resulting in near-heteroclinic transitions between opposite-flow states. Our results establish that channel confined active nematic turbulence is organized by a low-dimensional, symmetry-governed network of invariant solutions and their manifolds, and identify dynamical mechanisms that could be exploited to design, promote, or suppress flow reversals in active matter microfluidic devices.

I. INTRODUCTION

Active fluids serve as a paradigmatic class of non-equilibrium systems displaying a rich phenomenology, including spontaneous coherent flows, dynamical vortex patterns, and chaotic hydrodynamics (‘active turbulence’) [1–3]. Of particular recent interest among active fluids are active nematics (ANs), which are suspensions of rod-like units that convert energy into mechanical work at the individual level [4]. Examples of ANs include suspensions of elongated bacteria, kinesin-microtubule mixtures, and synthetic rod-like materials activated by chemical, optical or acoustic stimuli. These systems have attracted significant attention because they closely mirror biological processes from subcellular to multicellular scales and offer promising avenues for engineering applications.

Several continuum descriptions of active nematics have been derived using a variety of microscopic, phenomenological and data-driven techniques [5–8]. The dynamic behavior of the continuum models is usually studied via a mix of numerical simulations [9, 10], and linear stability analysis of the analytically derivable steady ‘base’ states [6, 11, 12]. These base steady states are usually the simplest equilibria, or in certain cases, traveling wave solutions. Some works extend the analysis to predict periodic states [13, 14], and/or apply weakly nonlinear analysis [15, 16] to predict first few bifurcations from the base states [17]. Other recent works have explored the role of nonlinearity and non-reciprocity in characterizing vortical and traveling flow patterns in general active systems [18–20]. There have also been recent theoretical and computational efforts to derive coarse-grained statistical descriptions [3, 21–23] of active turbulence, focusing on energy spectra and spatial organization of statistically steady states, rather than deterministic dynamics.

* Corresponding author. Email: piyush.grover@unl.edu

While these studies provide invaluable insight into certain deterministic and statistical aspects of motion of active fluids, our understanding of the complexities of active turbulence in confinement remains limited [24, 25]. In this context, a deterministic, dynamical systems based approach to studying active turbulence was initiated in our prior works [26, 27]. The basic premise is that the infinite-dimensional phase space of an active fluid is populated by *Exact Coherent Structures* (ECS), which are exact solutions of the physical dynamics with distinct and regular spatiotemporal structure; examples include equilibria, periodic orbits, and traveling waves. The ECSs are connected by dynamical pathways in phase space, built of intersections of invariant manifolds. While original ideas go back to [28, 29], recent computational and algorithmic advances have resulted in successful application of ECS-based framework to partially resolve the long-standing problem of transition to turbulence in *passive, high-Reynolds number* fluid flows [30]. Specifically, convincing numerical and experimental evidence that turbulent trajectories track certain ‘dominant’ ECSs has been obtained for such *passive, inertial* systems [31].

A priori, there are multiple reasons to expect that ECS framework can be equally useful in understanding *active* turbulence by revealing the underlying, low-dimensional skeleton of the dynamics. First, robust motifs such as defect creation/annihilation events and vortical flows recur across experiments and simulations. Second, the lack of energy cascade in active turbulence [3] implies a narrower band of dynamically relevant scales as compared to inertial turbulence. By identifying the ECSs and heteroclinic connections that scaffold the turbulent attractor, one can: (i) clarify which nonlinear mechanisms are essential for active turbulence, (ii) provide a reduced description in terms of transitions between a small number of organizing states, and (iii) potentially control or design active flows via targeted perturbations that steer the system between selected coherent structures.

In our prior work [26], we analyzed the dynamics of the 2D AN periodic channel flow at a single, preturbulent activity level, identifying several dominant ECSs and the associated heteroclinic network. In the follow-up work [27], we extended this effort by computing a larger collection of ECSs spanning both preturbulent and turbulent activity levels in the same system, and showed numerically that typical trajectories in the preturbulent regime repeatedly shadow various ECSs before ultimately decaying into an attractor. However, the sheer number of ECSs present in the turbulent regime made it impossible to unambiguously detect shadowing by turbulent trajectories, leaving open the question of how ECSs and their invariant manifolds structure active turbulence. Moreover, the question of how the ECS repertoire is organized and how the different ECSs are related to one another was left unresolved.

Our present work is based on the key observation that, for a given geometry and boundary conditions, many continuum models of active nematics share the same symmetry group and the same action of this group on the relevant fields. Equivariant bifurcation theory then implies that the *types* of primary and secondary bifurcations, and the symmetries of their branches are dictated largely by the system symmetry and isotropy structure rather than by microscopic details of the model [32, 33]. Thus, a symmetry-based classification of ECSs and their bifurcations in one representative active nematic model can provide a template that is expected to be broadly applicable across different continuum descriptions (e.g. for microtubule–kinesin mixtures, bacterial suspensions, or actomyosin layers) that share the same symmetry class.

In the present work, we use equivariant bifurcation theory to systematically trace the origins of dynamically relevant ECSs such as dancing disclinations, oscillatory nearly unidirectional states, and sustained vortices, and to provide a symmetry-based organization of this ECS zoo within a minimal flow unit (MFU). The MFU is chosen to be large enough to support sustained active turbulence, yet small enough to permit a systematic ECS-based analysis. Guided by this framework, we investigate a robust and striking phenomenon reported in active nematic channel flow (and more generally active fluid) simulations and experiments: spontaneous flow reversals between nearly unidirectional flow states in active turbulence. We identify a phase space skeleton, consisting of ECSs and their heteroclinic connections, that captures the essential mechanisms behind flow reversals in the preturbulent regime. The relative simplicity of the MFU then allows us to extend this picture into the turbulent regime, where we uncover the corresponding organizing skeleton consisting of ECSs whose origin can be traced back to the preturbulent regime using their symmetry signatures. Finally, we provide direct numerical evidence that typical turbulent trajectories shadow these ECSs and their invariant manifolds in active turbulence.

In summary, our results show that active nematic turbulence in 2D channels is organized by a low-dimensional, symmetry-governed network of invariant solutions and manifolds, and we outline a general strategy for identifying similar symmetry-based mechanisms in other active turbulent flows.

The remainder of this paper is organized as follows. In Section II, we introduce the system model, summarize our previous ECS-based analysis of active nematic channel flow, and review experimental and theoretical work on flow reversals in active and passive fluids. In Section III, we use the symmetries of the 2D AN equations to carry out an equivariant bifurcation analysis in minimal flow units, tracing primary and secondary local and global bifurcations, and constructing a symmetry-organized catalog of dynamically relevant ECSs. In Section IV, we use this catalog to describe transient flow reversals in the preturbulent regime, identifying a small number of ECS families and their heteroclinic connections as the main mechanisms by which trajectories switch between opposite nearly unidirectional states. In Section V, we extend this picture into the active turbulent regime in two MFUs, characterize the chaotic and quasiperiodic sets that arise at high activity, and demonstrate that persistent two-way reversals are organized by a reduced ECS skeleton whose members can be related back to the preturbulent branches via their symmetry signatures.

II. MODEL DESCRIPTION AND PRIOR WORK

A. Governing Equations

We consider the 2D Beris–Edwards continuum model for AN confined in a 2D periodic channel, a setup that has been used in several previous studies. [9, 26, 27, 34, 35]. It models the evolution of the velocity field $\mathbf{u}(\mathbf{x}, t) = (u, v)$ and the nematic alignment tensor $\mathbf{Q}(\mathbf{x}, t)$. The field \mathbf{Q} is a traceless tensor defined as $Q_{ij} = q(n_i n_j - 0.5 \delta_{ij})$, where q is the scalar order parameter describing the degree of nematic alignment, and the unit vector \mathbf{n} denotes its direction.

The domain is taken to be a two-dimensional channel of size $[0, \tilde{L}] \times [0, h]$, with $x \in [0, \tilde{L}]$ the streamwise (horizontal) direction and $y \in [0, h]$ the wall-normal (vertical) direction. We impose no-slip boundary conditions on the velocity field \mathbf{u} and perpendicular (homeotropic) anchoring on the nematic director \mathbf{n} at the confining walls. We employ the nondimensionalized equations obtained in [27]:

$$\begin{aligned} \text{Re}_n (\partial_t + \mathbf{u} \cdot \nabla) \mathbf{u} &= -\nabla p + 2(\nabla \cdot \mathbf{E}) - \frac{\text{Ra}}{\text{Er}} (\nabla \cdot \mathbf{Q}), \\ (\partial_t + \mathbf{u} \cdot \nabla) \mathbf{Q} + \mathbf{W} \cdot \mathbf{Q} - \mathbf{Q} \cdot \mathbf{W} &= \lambda \mathbf{E} + \mathbf{H}, \end{aligned} \quad (1)$$

$$\nabla \cdot \mathbf{u} = 0,$$

$$\mathbf{H} = \mathbf{Q} - b \text{Tr}(\mathbf{Q}^2) \mathbf{Q} + \nabla^2 \mathbf{Q}. \quad (2)$$

The boundary conditions are:

- **Velocity:** No-slip at $y = 0, h$, and periodic in x :

$$\mathbf{u}(x, 0, t) = \mathbf{u}(x, h, t) = \mathbf{0}, \quad \mathbf{u}(x + \tilde{L}, y, t) = \mathbf{u}(x, y, t).$$

- **Nematic tensor:** Homeotropic anchoring with $q = 1$ at $y = 0, h$ and periodic in x :

$$\mathbf{Q}(x, 0, t) = \mathbf{Q}(x, h, t) = \frac{1}{2} \begin{pmatrix} -1 & 0 \\ 0 & 1 \end{pmatrix}, \quad \mathbf{Q}(x + \tilde{L}, y, t) = \mathbf{Q}(x, y, t).$$

In Eq. (1), $\mathbf{W} \cdot \mathbf{Q} - \mathbf{Q} \cdot \mathbf{W}$ captures the effect of flow rotation on the nematic director, and $\lambda \mathbf{E}$ is the flow-alignment term. The \mathbf{H} term is the gradient of a free energy functional that promotes the creation of nematic order. We neglect

the passive elastic stress which is subdominant compared to active and viscous stress. Here, Re_n is the Reynolds number, R_a the dimensionless activity, and Er the Ericksen number. Following [4, 27], we fix $\text{Re}_n = 0.0136$ and $\text{Er} = 1$. As in the previous work [27], we also ignore the flow alignment to focus on the most relevant parts of the system and set the channel size to $\tilde{L} = 80$ and $h = 20$.

B. Exact Coherent Structure Framework for AN Channel Flow

In our previous works [26, 27], we recast the equations (1) as a dynamical system

$$\frac{dX}{dt} = F(X; R_a), \quad (3)$$

where $X = [\mathbf{u}, \mathbf{Q}]$, the activity number R_a is taken as the bifurcation parameter, and the associated flow map is given by $f^t(X_0) = X_0 + \int_0^t F[X(\tau)]d\tau$. We developed an open-source computational toolbox titled ‘Exact Coherent Structures in Active Matter’ (ECSAct) [36] using the open-source pseudospectral code Dedalus [37] to compute ECSs and heteroclinic connections. The problem of computing each ECS is posed as a fixed-point equation (FPE), and these high-dimensional FPEs are solved via modified Newton-Raphson algorithms using adaptive ‘hookstep’ method and the matrix-free GMRES method [38].

In the first work [26], this computational framework was used to identify 46 ECSs (up to symmetry), including the unidirectional flow (UNI), the bidirectional flow (LAN), 11 unstable POs, and 33 RPOs in the preturbulent regime, see Fig. 2. We deem a parameter value to be preturbulent if there exists a regular (i.e., non-chaotic) attractor, i.e., a *stable* ECS in the phase space. Several heteroclinic connections between various ECSs were also computed, allowing the phase space to be organized as a directed graph with ECSs as nodes. The follow-up work [27] confirmed the previously reported general sequence of attractors that are observed while increasing activity: zero flow, unidirectional flow, vortex lattice, and the transition to turbulence. In the preturbulent regime, we identified several ‘shadowing events’, which are defined as finite time intervals over which a trajectory stays close to an ECS, and the trajectory and the ECS have quantitatively similar time evolution. While more than 200 ECS were found in the turbulent regime, no evidence of shadowing was found in that regime.

C. Flow Reversals in Active Nematics and Other Active Fluids

The Ph.D. thesis [39] reported experimental results on AN systems in long, narrow channels whose open ends were connected to an external chaotic AN reservoir. Persistent, nearly unidirectional flows were observed, and the direction of these uniaxial flow states (UNI) was selected at random via spontaneous symmetry breaking of the zero-flow (ZF) state, as expected. More importantly, spontaneous and repeated reversals were also observed between the left- and right-flowing UNI states, and the reversal frequency depended on the channel dimensions. The author used the channel-averaged streamwise velocity $\langle u \rangle$ as an order parameter to quantify these reversals. In these experiments, a typical reversal proceeded via an intermediate state: the UNI state with a parabolic velocity profile ($\langle u \rangle \approx \pm u_0$) first collapsed into a vortex-dominated configuration with negligible net flow ($\langle u \rangle \approx 0$), and then evolved into a UNI state whose mean flow was opposite in direction to the original one (see Fig. 1).

These reversals were attributed to a bend-instability mechanism. Starting from a nematic that is predominantly aligned along the streamwise direction, a bend instability will develop in the transverse direction [12] and reorient the director accordingly. The resulting transversely aligned state is, in turn, unstable to bend perturbations along the streamwise direction, leading to repeated switching between the two streamwise-aligned configurations. To capture this behavior statistically, the author derived and used a single-degree-of-freedom Langevin dynamics model with a double-well potential, fitted to the experimental data. The well minima corresponded to the two UNI states, and noise-driven fluctuations induced transitions between them.

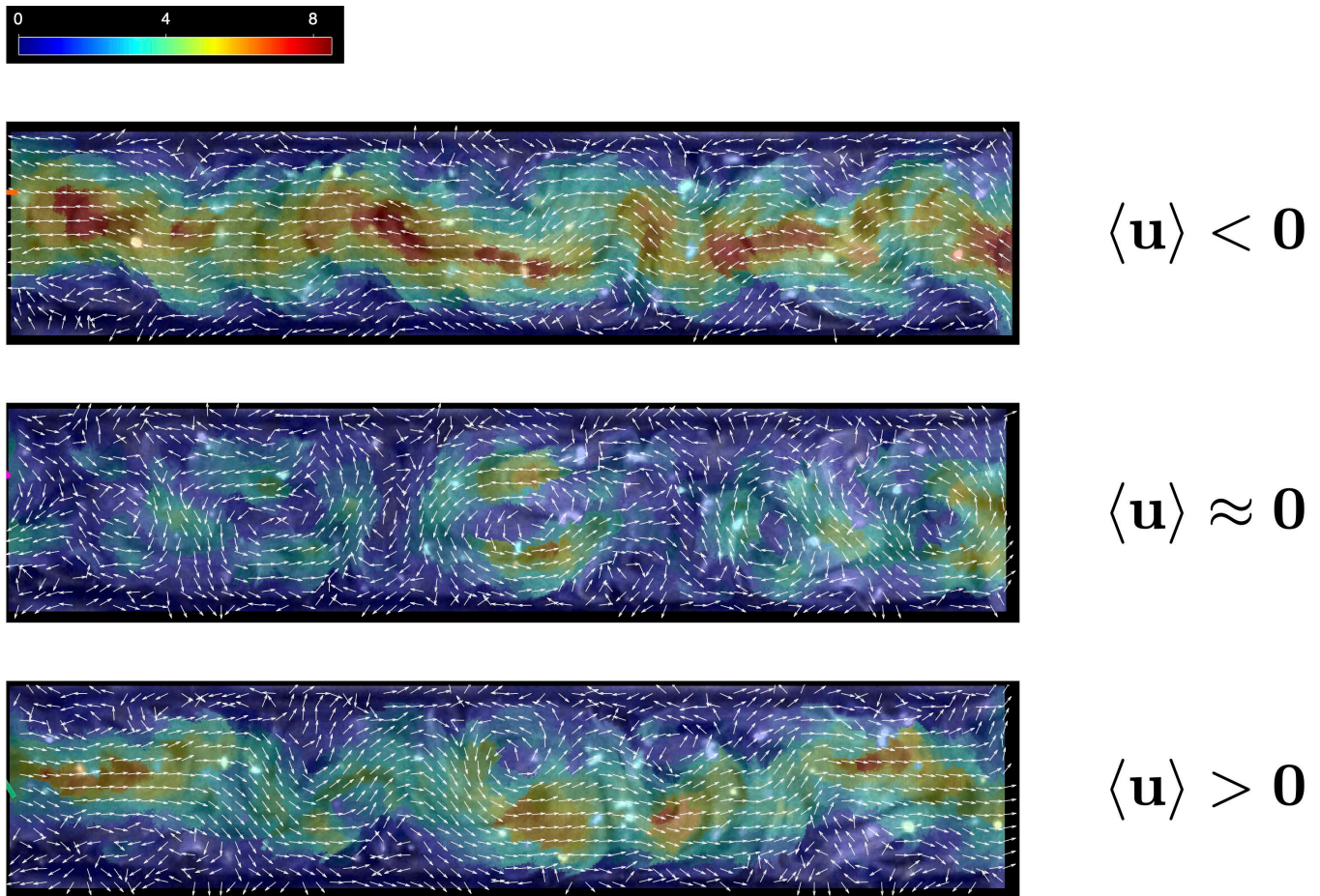


Figure 1: Velocity field snapshots from active nematic experiments of Doré [39] of a reversal event in a channel of size $500\mu\text{m} \times 100\mu\text{m}$. The colormap shows the speed ($\mu\text{m/s}$). The flow evolves from a left-flowing UNI-like state ($\langle u \rangle < 0$) to a right-flowing UNI-like state ($\langle u \rangle > 0$) via an intermediate vortex-dominated configuration ($\langle u \rangle \approx 0$). Reproduced with permission of the author.

AN flow reversals have also been observed in simulations of an (infinitely long) AN layer sandwiched between viscoelastic walls [14]. For sufficiently soft confinement, the authors found that the zero flow state undergoes a Hopf bifurcation to an oscillating flow state, in which the channel-averaged velocity reverses sign *periodically* in time, whereas stiffer walls produce steady unidirectional flow.

In polar active fluids, recent experimental, computational and analytical work [40] has argued that flow reversals are a precursor to active turbulence. The authors found that a dense suspension of swimming *Bacillus subtilis* confined to a cylindrical wells exhibit a single vortex steady flow at small radii. This state, which is analogous to the UNI in channel flow, loses stability as the radius is increased beyond a threshold. In the resulting oscillatory state, the vortex *periodically* reverses its direction. Using simulations and weakly nonlinear analysis of a Toner–Tu–Swift–Hohenberg model, it was shown that the onset of reversals is controlled by a global infinite-period bifurcation mediated by a resonant nonlinear interaction of the three lowest modes of the flow.

D. Possible Generic Dynamical Mechanisms Underlying Flow Reversals

Beyond active fluids, flow reversals have been extensively observed and studied in various settings [41–44]. A prominent example is that of turbulent Rayleigh-Benard convection (RBC) [45], in which large-scale convection (LSC) reversals between the clockwise and anticlockwise vortical states are robustly observed [46]. In addition to numerical simulations, such reversals have been studied using both deterministic and stochastic reduced-order dynamical

models [42, 47].

Regardless of their physical origins, systems that exhibit flow reversals are expected to share certain dynamical features. Typically, a quiescent base state first loses stability through spontaneous symmetry breaking, most naturally via a supercritical pitchfork bifurcation, producing two mirror-symmetric steady states. Exactly periodic reversals then imply the existence of a stable periodic orbit that alternately approaches these symmetry-related states, which may arise through a heteroclinic bifurcation or an infinite-period (global) bifurcation involving the two steady states. In turbulent regimes, where reversals are irregular and no simple periodic attractor exists, several possibilities arise. The turbulent trajectory may shadow a *robust heteroclinic cycle* [48–51] built from the two symmetry-related states, possibly together with an intermediate state, although such cycles typically require strong symmetry constraints.

A more likely scenario is that turbulent trajectories are shadowing two-way heteroclinic connections between a pair of mirror-image unstable periodic orbits, each of which passes close to one of the steady states. Similar heteroclinic structures, in which each of two unstable periodic orbits passes near a different steady state and the two orbits are linked by two-way heteroclinic connections, have been found in numerous other *low-dimensional* settings [52, 53]. This reversal scenario could also involve additional ‘intermediate’ states and their invariant manifolds. This mechanism was shown to be the dynamical skeleton responsible for LSC reversals in a 2D forced Navier-Stokes system recently [54]. In that work, the author computed the two mirror-image asymmetric periodic orbits, and a symmetric ‘intermediate’ orbit. In a reduced phase space projection, turbulent trajectories are shown to shadow one asymmetric periodic orbit, then depart along its unstable manifold towards the intermediate periodic orbit, and finally either fall back to the original side, or cross-over towards the other asymmetric periodic orbit.

The main goal of the current work is to identify such dynamical structures organizing the reversals in the active turbulent regime, and establish their shadowing by typical turbulent trajectories. As a first step, the next section presents a local and global bifurcation analysis in the low-activity, preturbulent regime, clarifying how symmetry dictates the emergence of the most common ECS families in active nematic channel flows. The system naturally favors an intrinsic active vortex scale, resulting in threefold or fourfold symmetry of vortex lattice states in our chosen domain [27]. Hence, we carry out the equivariant analysis in shorter MFUs [55, 56], specifically $L = \tilde{L}/3$ and $L = \tilde{L}/4$, with a particular emphasis on the former due to its relevance in reversal dynamics.

III. LOCAL AND GLOBAL BIFURCATIONS IN 2D AN CHANNEL FLOW: ROLE OF SYMMETRY

The systematic way to perform bifurcation analysis of systems with symmetry is by using equivariant bifurcation theory [32, 57]. We begin this section by recalling some group theoretic definitions, and listing the symmetries of the AN 2D channel flow system. Then we revisit the equivariant analysis of primary bifurcations of the zero flow (ZF) state [33]. This prior work explains the emergence of UNI and LAN-like solutions in AN channel flows. We significantly extend the analysis of [33] to secondary local and global bifurcations, providing a partial but insightful explanation of the origin of dynamically relevant solutions and a classification based on their symmetry properties. Along the way, we highlight the consequences of symmetry-breaking, symmetry-preserving and symmetry-restoring bifurcations. A summary of the ECSs examined in this section, together with their symmetries, is provided in Table V in the appendix. Videos of the spatiotemporal evolution of these ECSs are provided in the Supplemental Material.

A. Preliminary definitions

A dynamical system of the form given by Eq. (3) is said to be equivariant under a group action σ if the time evolution and the group operation commute, i.e. for every state X and time T , the relationship $\sigma(f^T(X)) = f^T(\sigma X)$ is satisfied [58]. For an equivariant system, if X is a solution, then σX is also a solution. Now, let the system Eq. (3) be equivariant under a group G , which implies that the above two properties are valid for all $\sigma \in G$.

We need to introduce additional definitions and notations from group theory that we use in the equivariant analysis. First, we denote $GL(\mathbb{R}^n)$ as the group of all real invertible $n \times n$ matrices. The subgroup $O(n) \subset GL(\mathbb{R}^n)$ is the set of matrices A satisfying the orthogonality condition $A^T A = 1$. We are primarily interested in groups that are isomorphic to $O(n)$ or to any closed subgroup of $O(n)$, i.e., compact Lie groups. Strictly speaking, the linear action of the symmetry σ on the state X is given by a matrix $\rho(\sigma)$, where the function ρ is called a representation of G :

Definition 1 (Group Representation) *Let G be a group and V a vector space. A representation of G on V is a homomorphism*

$$\rho : G \rightarrow GL(V),$$

where $GL(V)$ is the group of invertible linear transformations on V . For $\sigma \in G$ and $X \in V$, we will often write $\sigma X := \rho(\sigma)X$.

If it is clear in the context, we will use the same symbol to denote the group element and the corresponding matrix.

We will say that a vector X has σ symmetry if it is *invariant* under the action of a group element σ , i.e., $\sigma(X) = X$. A solution of an equivariant system can have all, some or none of the symmetries G . Usually, we are interested in the group elements that act fix a specific vector X , motivating the following definition.

Definition 2 (Isotropy Group) *Let G act on a set V . For an $X \in V$, the isotropy group (or stabilizer) of X is the subgroup*

$$\Sigma_X = \text{Stab}_G(X) = \{\sigma \in G \mid \sigma X = X\}.$$

On the other hand, it is also relevant to know which vectors are invariant under the action of a specific subgroup.

Definition 3 (Fixed Point Subspace of a Subgroup) *Let $\Sigma \subset G$ be a subgroup. The fixed point subspace of Σ , denoted $\text{Fix}(\Sigma)$, is defined as*

$$\text{Fix}(\Sigma) = \{X \in V \mid \sigma X = X \text{ for all } \sigma \in \Sigma\}.$$

An important property of fixed point subspaces is that they are *flow invariant*, i.e., if $X(0) \in \text{Fix}(\Sigma)$, then $X(t) \in \text{Fix}(\Sigma)$, for all $t > 0$. The final definition we introduce in this section is that of the group orbit. Other useful definitions will be introduced as needed in the subsequent sections.

Definition 4 (Group Orbit) *For a point $X \in V$, the **orbit** of X under the action of G is the set*

$$GX = \{\sigma X \mid \sigma \in G\}.$$

That is, the orbit of X is the set of all points in V to which X can be moved by the action of elements of G .

B. Symmetries in the active nematics equations

The governing equations (1) with the imposed boundary conditions are equivariant under the continuous symmetries $\tau_x(\ell)$ corresponding to x -translation, the discrete symmetry σ_x corresponding to reflection about the midplane x -axis, and the discrete symmetry σ_y corresponding to reflection about the y -axis. The corresponding actions on the physical

fields are:

$$\begin{aligned}
\sigma_x[u, v, Q_{11}, Q_{12}](x, y) &= [u, -v, Q_{11}, -Q_{12}](x, h - y), \\
\sigma_y[u, v, Q_{11}, Q_{12}](x, y) &= [-u, v, Q_{11}, -Q_{12}](L - x, y), \\
\tau_x(\ell)[u, v, Q_{11}, Q_{12}](x, y) &= [u, v, Q_{11}, Q_{12}](x + \ell, y).
\end{aligned} \tag{4}$$

Due to the periodic boundary conditions in x , the set of translations $\tau_x(\ell)$ is isomorphic to the rotational symmetry group $SO(2)$. The reflection symmetry σ_x generates a cyclic group of order 2, which we denote as $\mathbb{Z}_2(\sigma_x)$. Likewise, the reflection symmetry σ_y generates the cyclic group denoted by $\mathbb{Z}_2(\sigma_y)$. The x-translations and y-reflections do not commute, so they form $O(2) = SO(2) \rtimes \mathbb{Z}_2$ (a semidirect product). The x-reflection $\mathbb{Z}_2(\sigma_x)$ commutes with this $O(2)$. Finally, the full symmetry group of the system is

$$G = \mathbb{Z}_2(\sigma_x) \times O(2).$$

Aside from the work of Marzorati and Turzi [33], which we discuss in the next subsection, prior stability and bifurcation studies of active nematic channel flows have not systematically exploited these symmetries. This omission obscures the underlying structure of the infinite-dimensional dynamical system [59]. In this work, we use equivariant bifurcation theory to systematically predict the emergence of new steady and time-dependent solution branches and to determine the symmetries of these solutions.

Some solutions of Eq. (1) have already been classified by their symmetries previously [26]. The ZF inherits all the symmetries of G , but UNI and LAN lack the σ_y and $\sigma_x\sigma_y$ symmetries, respectively. More generally, the plethora of ECSs found in [26] exhibit a rich variety of patterns with observable spatiotemporal symmetries (see Fig. 2). The system selects preferable discrete translation symmetries to form vortex solutions [26, 27], many of them corresponding to oscillatory solutions which maybe traveling waves, periodic or relative periodic orbits. In the rest of this section, we use equivariant bifurcation theory to identify the origins of key ECSs, organize the associated solution branches by their shared symmetries, and assemble a partial isotropy lattice that connects symmetry-distinct branches through sequences of symmetry-breaking bifurcations.

C. Primary bifurcation in active nematics

The generalized equivariant branching lemma [32, 57, 58] described below is a fundamental tool in equivariant bifurcation analysis, and provides the conditions for the existence of a symmetric fixed point branch emerging from a singular fixed point X^* at a bifurcation value $R_a = R_a^*$. To apply this framework to our high-dimensional system (Eqs. 3), we restrict the system to the center manifold, where the evolution is given by $\frac{dY}{dt} = F_c(Y, \mu)$, where $\mu = R_a - R_a^*$, and the system satisfies $F_c(0, 0) = 0$, and $D_Y F_c(0, 0) = 0$. The reduced system F_c is Γ -equivariant, where Γ is the isotropy group of X^* , i.e., $\Gamma = \{\sigma \in G \mid \sigma(X^*) = X^*\}$.

Theorem 1 (Generalized Equivariant Branching Lemma) *Let F_c be as defined above, and let Σ be a isotropy subgroup of Γ . Assume that $D_\mu F_c(0, 0)w \neq 0$ for nonzero $w \in \text{Fix}(\Sigma)$, and $\text{Fix}(\Gamma) = 0$. Then, if $\dim(\text{Fix}(\Sigma)) = 1$ (**axial** subgroup), there exists a smooth branch of fixed points of F_c (and hence, of F) emerging from the origin with symmetry Σ .*

Note that if X^* has all the symmetries of G , then $\Gamma = G$, but otherwise, Γ is a proper subgroup of G . A key observation is that Γ commutes with the Jacobian $L := D_X F(X^*, R_a^*)$, which implies that $\Gamma(\ker L) = \ker L$, i.e., Γ maps the kernel (or the center subspace) back to itself. This fact allows us to study the bifurcation problem via the reduced system F_c by analyzing the action of Γ on the center subspace.

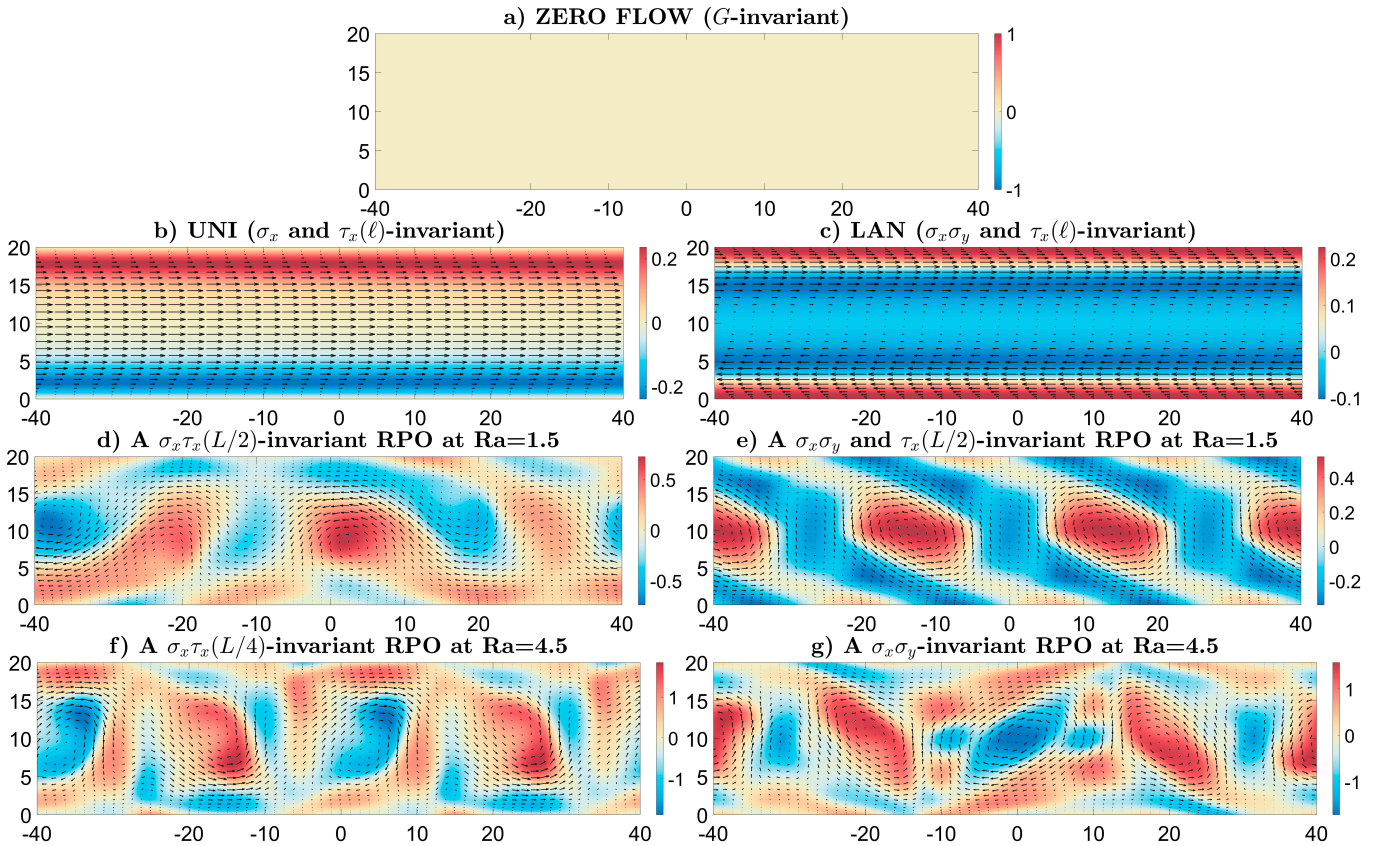


Figure 2: Snapshots of the velocity field for selected ECSs at representative activity numbers $R_a = 1.5$ and $R_a = 4.5$, showing their symmetry generators in the full-length channel, $L = \bar{L}$. The colormap represents vorticity.

Using the EBL, Marzorati and Turzi [33] performed an equivariant bifurcation analysis of the 2D AN channel system to obtain solutions bifurcating from the zero-flow (ZF) state. We discuss their calculations of this primary bifurcation to illustrate the application of the EBL and set the stage for calculation of secondary bifurcations that follow.

By restricting the analysis to (x -) translation invariant solutions, they only considered equivariance with respect to the Klein four-group $\hat{G} = \mathbb{Z}_2(\sigma_x) \times \mathbb{Z}_2(\sigma_y)$. The ZF solution has the full symmetry, and hence $\Gamma = \hat{G}$. The kernel of the Jacobian at ZF has two dimensions that we associate to \mathbb{R}^2 spanned by the two eigenvectors corresponding to zero eigenvalues. In this subspace, the matrix representations of the group $\Gamma = \{I, \sigma_x, \sigma_y, \sigma_x\sigma_y\}$ were computed in the eigenvector basis, and found to be

$$I = \begin{bmatrix} 1 & 0 \\ 0 & 1 \end{bmatrix}, \quad \sigma_x = \begin{bmatrix} 1 & 0 \\ 0 & -1 \end{bmatrix}, \quad \sigma_y = \begin{bmatrix} -1 & 0 \\ 0 & -1 \end{bmatrix}, \quad \sigma_y\sigma_x = \begin{bmatrix} -1 & 0 \\ 0 & 1 \end{bmatrix}.$$

The four proper subgroups of Γ are $\{I\}$, $\mathbb{Z}_2(\sigma_x)$, $\mathbb{Z}_2(\sigma_y)$, and $\mathbb{Z}_2(\sigma_x\sigma_y)$. The corresponding fixed point subspaces are

$$\begin{aligned} \text{Fix}(\{I\}) &= \mathbb{R}^2 : \text{2D fixed point subspace,} \\ \text{Fix}(\mathbb{Z}_2(\sigma_x)) &= \{(a, 0) \in \mathbb{R}^2 \mid a \in \mathbb{R}\} : \text{1D fixed point subspace,} \\ \text{Fix}(\mathbb{Z}_2(\sigma_y)) &= \{(0, 0)\} : \text{0D (trivial) fixed point subspace,} \\ \text{Fix}(\mathbb{Z}_2(\sigma_x\sigma_y)) &= \{(0, b) \in \mathbb{R}^2 \mid b \in \mathbb{R}\} : \text{1D fixed point subspace.} \end{aligned}$$

Hence, there are two axial (i.e. with 1D fixed point subspaces) subgroups Σ , and by the EBL, we have two pitchfork bifurcations. The first bifurcation leads to UNI-like solutions with reflection symmetry $\Sigma_1 = \sigma_x$, and the second to LAN-like solutions with symmetry $\Sigma_2 = \sigma_x \sigma_y$. Due to the pitchfork nature of these bifurcations, each new solution branch has a symmetric counterpart obtained by applying σ_y . Therefore, a total of four nontrivial solution branches emerge.

Building upon this result, we carry out secondary bifurcation analysis from the UNI and LAN states in the following sections.

D. Secondary bifurcations from UNI

The UNI solution loses stability when a ('first') pair of complex eigenvalues crosses the imaginary axis. The corresponding eigenvectors break translation symmetry, and have isotropy group $\Sigma_{p_1(\text{UNI})} = \text{gen}\{\sigma_x \tau_x(L/2)\}$, corresponding to the 'shift-reflect' symmetry [59]. Here, we use the notation $p_1(\text{UNI})$ to denote the first complex pair of eigenvalues (and the corresponding eigenspace) of the UNI. The imaginary nature of the eigenvalues suggest the possibility of a Hopf bifurcation. This bifurcation is expected to lead to oscillatory solutions that respect the underlying symmetry $\Sigma_{p_1(\text{UNI})}$. Such oscillatory states are typically small perturbations of the UNI configuration, and have been reported in previous studies [9, 34, 60–62]. Here, we explore a scenario in which traveling waves emerge from this destabilization of UNI.

Secondary bifurcations are often more challenging to analyze than primary bifurcations, as the standard equivariant bifurcation theorems typically do not apply directly. This difficulty arises when a solution undergoing bifurcation has less symmetry than the full group G , and a resulting continuous group orbit. The presence of the latter can dramatically modify the bifurcation scenario. While UNI (and LAN) have a smaller symmetry than G , their group orbits are discrete, and consist of two points each (the two y-reflections via σ_y). This allows the direct use of standard equivariant bifurcation theory.

1. Traveling waves emerge from UNI

We now state a version of the equivariant Hopf theorem [32, 57, 58] (EHT) which will be used to predict bifurcating oscillatory solutions with symmetry at a singular fixed point with a pair of purely pair of eigenvalues. As in the EBL case, we consider the reduced-dynamics on this 2D center subspace, which we identify as \mathbb{R}^2 spanned by the two eigenvectors. The reduced system $\dot{Y} = F_c(Y, \mu)$ is Γ -equivariant, where Γ is the isotropy subgroup of the fixed point X^* . Let the eigenvalues be $\lambda(\mu) = \sigma(\mu) \pm i\rho(\mu)$, with bifurcation occurring at $\mu = 0$.

Theorem 2 *Let F_c be as defined above, and Γ act simply on the center subspace. Assume $\frac{d\sigma}{d\mu}|_{(\mu=0)}$ is different from zero. Suppose there exists an isotropy subgroup $\Sigma \subset \Gamma \times \text{SO}(2)$ such that $\dim(\text{Fix}(\Sigma)) = 2$. Then there exists a unique branch of time-periodic solutions with period $\approx 2\pi/\omega$ emerging from the origin with spatio-temporal symmetry Σ , where $\omega = \rho(0)$.*

To apply this to bifurcation of UNI, we consider the isotropy subgroup of UNI as the base group, denoted by $\Gamma = \mathbb{Z}_2(\sigma_x) \times \text{SO}(2) \subset G$. According to EHT, we seek a subgroup $\Sigma \subset \Gamma \times \text{SO}(2)$ that fixes pointwise a two-dimensional subspace, which in this case is the entire \mathbb{R}^2 .

Next, we obtain the representation of $\Gamma = \mathbb{Z}_2(\sigma_x) \times \text{SO}(2)$ on \mathbb{R}^2 in the eigenvector basis. On this center subspace, we find that reflection σ_x acts as

$$\sigma_x = \begin{pmatrix} -1 & 0 \\ 0 & -1 \end{pmatrix}, \quad (5)$$

and the translations act as the rotation matrices

$$R(\phi) = \begin{pmatrix} \cos \phi & -\sin \phi \\ \sin \phi & \cos \phi \end{pmatrix}, \quad \phi = \frac{2\pi\ell}{L}, \quad \ell \in [0, L), \quad \phi \in [0, 2\pi), \quad (6)$$

where the angle ϕ parametrizes the spatial rotation. The representation of the temporal group is

$$R_t(\theta) = \begin{pmatrix} \cos \theta & \sin \theta \\ -\sin \theta & \cos \theta \end{pmatrix}, \quad \theta \in [0, 2\pi), \quad (7)$$

where θ parametrizes the ‘rotation’ in time.

The representation of Γ is irreducible but not absolutely irreducible on \mathbb{R}^2 , i.e., it acts simply on \mathbb{R}^2 . Indeed, the only subspaces invariant under the action of all group elements given by Eqs. (5) and (6) are the origin, and the whole space \mathbb{R}^2 , and these matrices commute with each other.

The spatiotemporal isotropy subgroup Σ that fixes \mathbb{R}^2 (pointwise) consists of all group elements whose representation is the identity matrix, which yields:

$$\Sigma = \{I, \sigma_x R(\pi), \sigma_x R_t(\pi), R(\theta)R_t(\theta)\}. \quad (8)$$

Recall that $R(\pi)$ is the $L/2$ spatial shift, and hence the purely spatial discrete symmetry $\sigma_x R(\pi)$ is nothing but the shift-reflect symmetry $\Sigma_{p1(U)}$. As rotation in time $R_t(\pi)$ has the same representation as the spatial $L/2$ shift $R(\pi)$, the discrete spatiotemporal symmetry $\sigma_x R_t(\pi)$ is also the shift-reflect symmetry. Finally, the group elements of the form $R(\theta)R_t(\theta)$ describe continuous spatiotemporal symmetries in which each shift (or rotation) in space is compensated by a corresponding rotation in time.

Then, the EHT says that a unique branch of small-amplitude **time-periodic** solutions bifurcates from the UNI state, with spatiotemporal symmetry group Σ . Concretely, $R(\theta)R_t(\theta)$ symmetry implies the solutions are (small-amplitude) traveling (or equivalently, rotating) waves, while the other two symmetries require that these traveling waves possess the purely spatial shift-reflect symmetry $\sigma_x \tau_x(L/2)$.

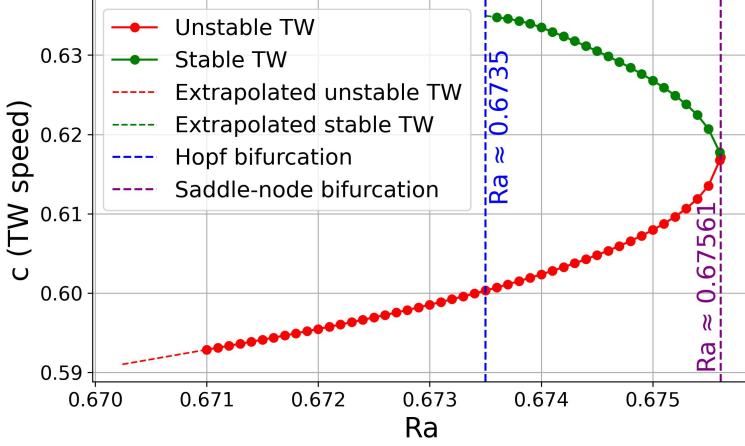


Figure 3: Bifurcation diagram showing TW speed vs R_a for the MFU with length $L = \tilde{L}/4$. As UNI loses stability at $R_a \approx 0.6735$, a stable TW emerges through a Hopf bifurcation. An unstable TW exists prior to this value and collides with the stable TW in a saddle-node bifurcation at $R_a \approx 0.67561$, leading to their mutual disappearance.

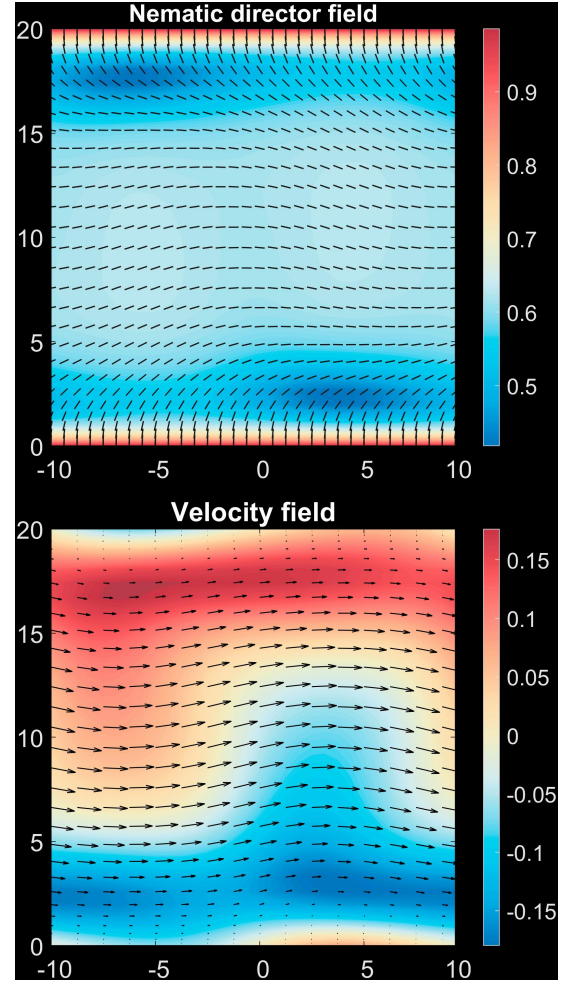


Figure 4: A snapshot of the nematic director and velocity fields of the stable traveling wave at $R_a = 0.67558$ (for MFU with $L = \tilde{L}/4$). This solution lies in the fixed-point subspace of $\Sigma_{p_1(U)}$, i.e., it has the shift-reflect symmetry.

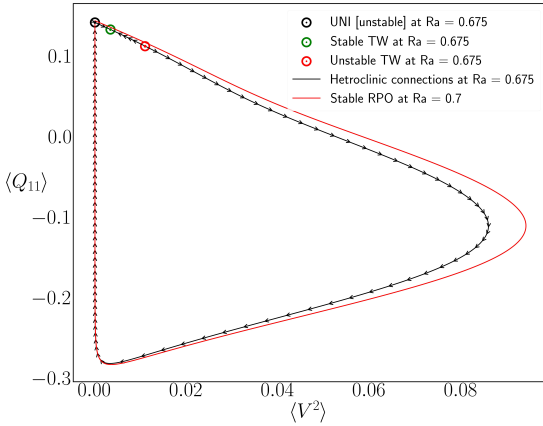


Figure 5: Projection onto the reduced phase space $(\langle Q_{11} \rangle, \langle v^2 \rangle)$, showing the stable and unstable TWs before the SNIPER bifurcation, with a heteroclinic connection passing close to UNI. Here, $\langle \cdot \rangle$ denotes channel average. Note the RPO that emerges after SNIPER has a shape similar to that of the vanished heteroclinic network.

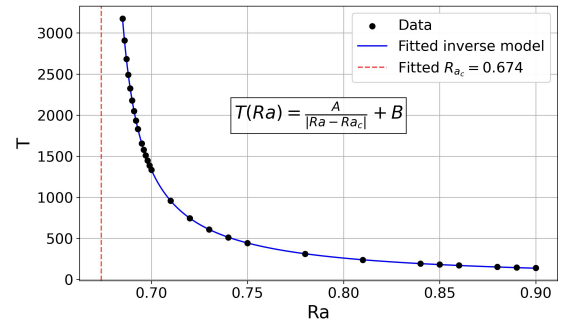


Figure 6: Inverse-scaling-law fit for the period along the emerging RPO branch., supporting the SNIPER bifurcation scenario. Here, $A \approx 35.21$ and $B \approx -20.683$. Notice that the fitted bifurcation value $R_{ac} \approx 0.674$ is quite close to the value $R_{ac} \approx 0.67558$ obtained from the calculations based on data before the bifurcation.

Figure 7: Saddle-node infinite-period bifurcation of traveling waves following the Hopf bifurcation of UNI equilibrium in the MFU with $L = \tilde{L}/4$.

2. Saddle-node bifurcation of traveling waves

The equivariant bifurcation analysis so far is general enough to be applied independently of the channel dimensions. For a MFU of length $L = \tilde{L}/4$, our computations yield the stable TW predicted in the previous section (see Fig. 3). This TW exists in the range $R_a \approx 0.6735$ to $R_a \approx 0.67561$, where it collides with an unstable traveling wave (UTW) and disappears in a saddle-node bifurcation. This is a bifurcation from the TW solution, a *continuous group orbit*. As remarked previously, we need to use an extension of the standard equivariant bifurcation theory that accounts for the effects of the continuous symmetries [63] of the TW solution, in order to theoretically confirm this bifurcation.

For a Γ -equivariant dynamical system, suppose the group orbit ΓX_0 of a point X_0 has dimension at least one (i.e., it is not a discrete set of points), and let Σ_{X_0} be the isotropy subgroup of X_0 . This group orbit can be flow-invariant (even if X_0 is not an equilibrium) when the dynamics of the system cause the solution to evolve purely along the group orbit, in which case the group orbit is referred to as a relative equilibrium. The TW and UTW solutions are both examples of such relative equilibria.

The bifurcation analysis of a relative equilibrium begins by locally decomposing the vector field F into the sum of a normal (to the group orbit) component and a tangential (i.e., along the group orbit) component: $F = F_N + F_T$, near the relative equilibrium ΓX_0 [63]. Roughly speaking, the dynamics of F_N can be understood as the dynamics of F modulo the drift along the group orbit. To analyze the bifurcation, we consider the restriction $H(X, \mu)$ of $F_N(X, \mu)$ to the subspace N_{X_0} , which is normal to the group orbit at the point X_0 . A classical equivariant bifurcation analysis can then be performed on H . The following proposition, which is an extension of EBL, is needed to address the case where Σ_{x_0} acts trivially on a 1D or 2D center subspace [63].

Proposition 1 *Suppose the action of the isotropy subgroup Σ_{X_0} on the eigenspace is trivial.*

- *If $D_X H(X_0, 0)$ has a zero eigenvalue, then generically H undergoes a limit point (saddle-node) bifurcation.*
- *If $D(X_0, 0)$ has a pair of purely imaginary eigenvalues $\pm i\omega$, then generically $\pm i\omega$ are simple and H undergoes a Hopf bifurcation to a unique periodic solution.*

For the case at hand, we approximate the relevant eigenspace by computing the subspace corresponding to the eigenvalue with smallest non-zero real part for linearization around the UTW, close to the saddle-node bifurcation point. As expected, this space is one-dimensional, associated with a small real eigenvalue, and is invariant under the symmetry $\sigma_x \tau_x(L/2)$. This implies that the action of the isotropy subgroup Σ_{x_0} on the eigenspace is trivial, indicating that no symmetry is broken at the bifurcation. By Proposition 1, we conclude that the bifurcation is a saddle-node bifurcation of relative equilibria. This result is consistent with our numerical finding that the two branches of traveling waves coalesce at the bifurcation point.

The rigorous dimension count of the group orbits of equilibria and periodic orbits is given by the following theorem.

Theorem 3 [63] *Consider a Γ -equivariant dynamical system.*

- *Let X be an equilibrium of the normal vector field, with isotropy group let Σ_X . Then the group orbit of X is generically a quasiperiodic solution with k basic frequencies, where $k = \text{rank}(N(\Sigma_X)/\Sigma_X)$.*
- *Let Y be a periodic orbit of the normal vector field, and Σ_Y be the group of symmetries mapping Y to itself. Then the group orbit ΓY is generically a quasiperiodic solution with k basic frequencies, where $k = \text{rank}(N(\Sigma_Y)/\Sigma_Y) + 1$.*

Here, $N(\Sigma_X)$ denotes the normalizer of Σ_X in Γ , and rank refers to the maximum dimension of the resulting torus.

Remark: Under the bifurcation scenario of Proposition 1, the resulting equilibria (X) and periodic orbits (Y) bifurcating from X_0 both inherit the symmetry of X_0 . Hence in such situations, the Theorem 3 dimension counts can be replaced by $k = \text{rank}(N(\Sigma_{X_0})/\Sigma_{X_0})$, and $k = \text{rank}(N(\Sigma_{X_0})/\Sigma_{X_0}) + 1$, respectively.

Using the dimension count formula of Theorem 3 with $\Gamma = \mathbb{Z}_2(\sigma_x) \times \text{SO}(2)$ (inherited from UNI), and isotropy group being the shift-reflect $\Sigma_{X_0} = \mathbb{Z}_2(\sigma_x \tau_x(L/2))$, we get $k = 1$. This is consistent with our observation that the bifurcating solutions are traveling waves, where time evolution coincides with translations $\tau_x(l)X$ ($0 \leq l \leq L$).

3. Saddle-node Infinite-period bifurcation and the origin of homoclinic-like relative periodic orbits

The saddle-node bifurcation of TWs discussed above is part of a global bifurcation scenario involving a saddle-node infinite-period bifurcation (SNIPER), as illustrated in Fig. 7. In the interval $0.6737 \leq R_a \leq 0.67561$, UNI, TW, and UTW coexist, with evidence of heteroclinic connections between them. To investigate whether transversal or tangential intersections among their manifolds are possible, we focus on the activity value $R_a = 0.675$. Generically in an N -dimensional space, an unstable manifold of dimension n_u will intersect a stable manifold of dimension n_s in $d = n_u + n_s - N$ dimensional submanifold [64].

UNI and UTW each have two-dimensional unstable manifolds, which allows for transversal intersections with the stable manifold of TW. However, a transversal connection between the unstable manifold of UTW and the stable manifold of UNI is not possible. Perturbing UNI along its unstable manifold leads TW, while perturbing UTW in an unstable direction also drives the system toward TW. Interestingly, we also found a heteroclinic connection from UTW to UNI very close to $R_a = 0.675$. The various connections are illustrated in Fig. 5.

As the activity increases, the two traveling waves get closer and disappear in the saddle-node bifurcation at $R_a \approx 0.6756$. Beyond this point, a family of relative periodic orbit (RPO) with isotropy group $\Sigma_{p_1(U)}$ emerges, passing very close to UNI. The shape of the resulting RPOs, shown in the reduced phase space in Fig. 5, closely resembles the vanished heteroclinic network, and their periods follow an inverse law characteristic of a SNIPER bifurcation [65] (see Fig. 6).

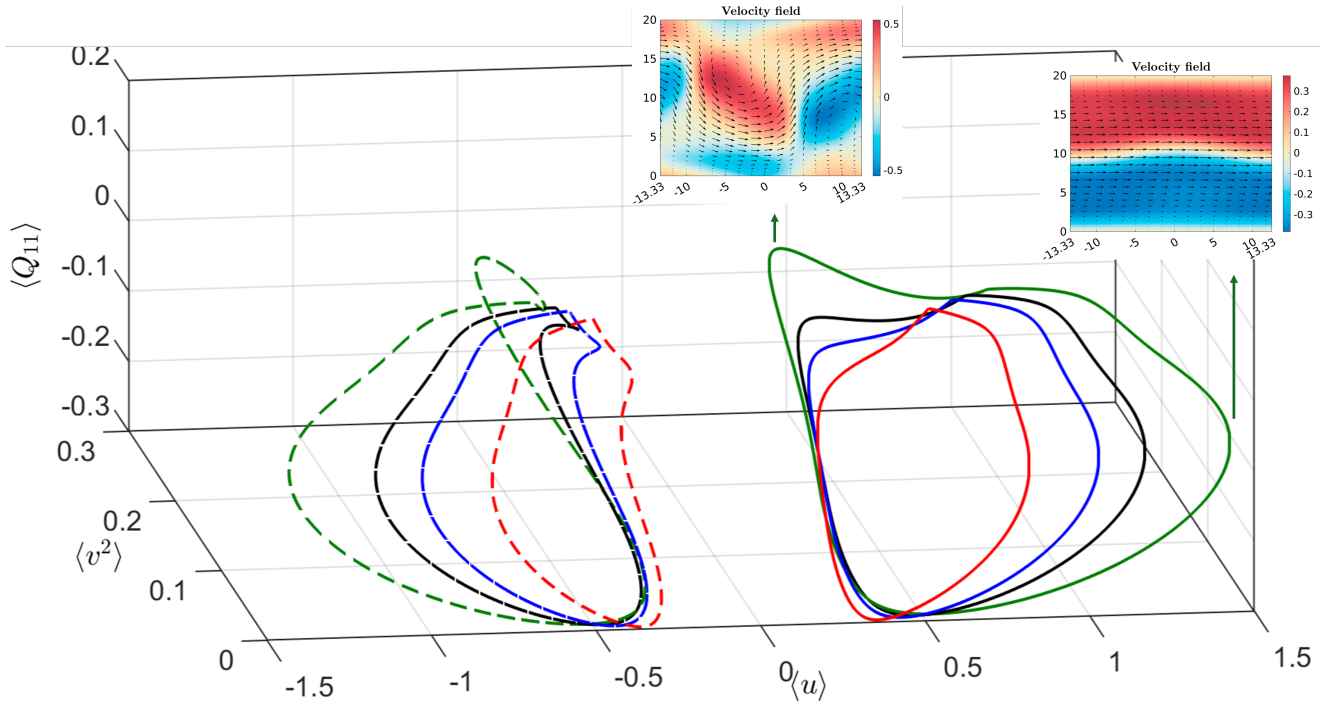
In MFU with length $L = \tilde{L}/3$, the predicted traveling wave (TW) bifurcating from UNI proved elusive to detect. We only found an unstable TW that disappears when UNI loses stability and can be traced back to lower activity numbers, around $R_a \approx 0.55$. In this MFU, the branch of bifurcating RPOs originating near $R_a \approx 0.71$ also exhibits decreasing periods as activity increases, consistent with a SNIPER bifurcation law (see Fig. 8). We therefore conclude that the saddle-node bifurcation likely occurs near $R_a \approx 0.71$ in the MFU with $L = \tilde{L}/3$, although the small-amplitude stable TW is difficult to detect due to the close proximity (in parameter space) of the Hopf and saddle-node bifurcations.

Due to their proximity to UNI in phase space, we refer to these RPOs as *homoclinic-like RPOs* characterized by recurrent processes of defect creation and annihilation. We refer to the RPO family in Fig. 8 as HRPO_{T1a} , where Tk in the subscript implies the L/k translation symmetry, and the following letter distinguishes different families (a, b, \dots). Since the dynamics leading to flow reversals are closely associated with the exact coherent structures (ECSs) that emerge in the channel with $L = \tilde{L}/3$, we henceforth restrict our analysis to this domain (and subdomain $L = \tilde{L}/6$) for the remainder of the paper. The MFU with $L = \tilde{L}/3$ is henceforth referred to as MFU A.

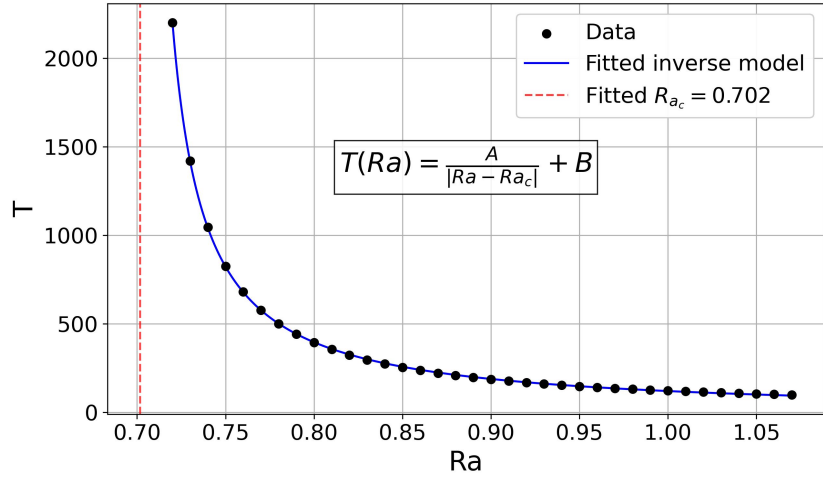
4. From Homoclinic-like RPOs to Heteroclinic-like POs

As activity increases beyond the SNIPER value, the periods of homoclinic-like RPOs initially decrease (as predicted by the inverse law), but eventually the RPOs start to become larger again, until the RPO branch collides with UNI and disappears through a homoclinic bifurcation at approximately $R_a \approx 1.38$. Our computations confirm the characteristic logarithmic scaling associated with this type of bifurcation (see Fig. 9b).

Immediately beyond this point, a branch of heteroclinic-like periodic orbits emerges, passing very close to both UNI and $\sigma_y \text{UNI}$ (see Fig. 9a), via a heteroclinic bifurcation involving these equilibria. For these activity numbers, the period data again fits well to a logarithmic curve, as shown in Fig. 9c. The solutions on this new branch of periodic orbits are denoted as belonging to the HTPO_{T1a} family, where we use the same naming convention as before. The origin of these heteroclinic-like POs is a type of *symmetry-increasing* bifurcation [66, 67] in which the two RPOs,



(a) Reduced phase space projection of four members of the homoclinic-like RPO family $HRPO_{T1a}$ at $Ra = 0.72, 0.90, 1.02,$ and 1.24 , shown in red, blue, black, and green solid curves, respectively. Their σ_y counterparts are shown as dashed curves. For $HRPO_{T1a}$ at $Ra = 1.24$, we show velocity snapshots at two locations along the orbit: one corresponding to a vortex-dominated flow state and the other a nearly unidirectional flow state.

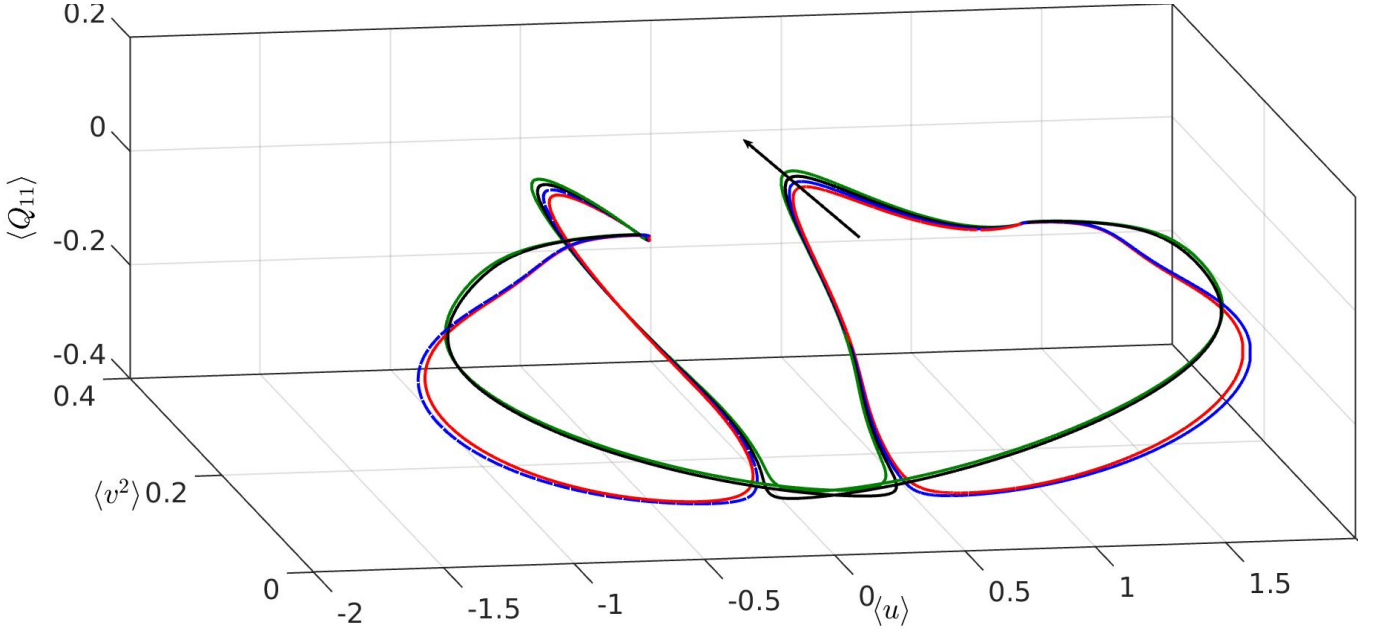


(b) Inverse law scaling fit between the period and the activity. Here, $A \approx 40.399$, $B \approx -16.209$, and $Ra_c \approx 0.702$.

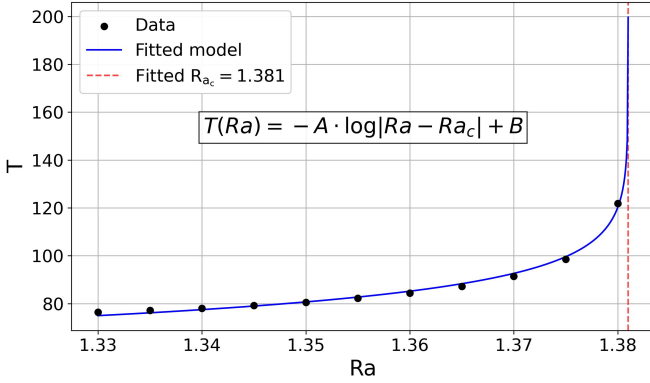
Figure 8: Confirmation that homoclinic-like RPOs (of the $HRPO_{1a}$ family) originate from a SNIPER bifurcation in the MFU A ($L = \tilde{L}/3$).

related by the σ_y symmetry, disappear to create a PO whose orbit is σ_y -symmetric. These kinds of solutions are important because they contain trajectories connecting the two sides of the reduced phase space, i.e., $\langle u \rangle > 0$ and $\langle u \rangle < 0$. The $HTPO_{T1a}$ members are additionally invariant under the symmetry $\sigma_x \tau_x(L/2)$ inherited from the HRPOs.

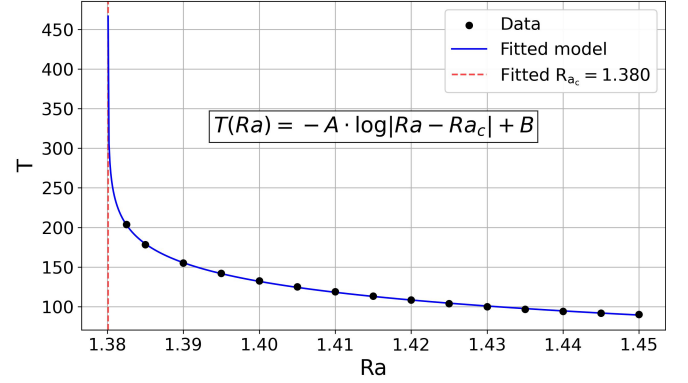
We find another heteroclinic bifurcation again involving UNI and σ_y UNI at approximately $Ra \approx 1.48$, giving rise to a second branch of heteroclinic-like POs $HTPO_{T1b}$ (see Fig. 10a). We have observed that the two branches, $HTPO_{T1a}$ and $HTPO_{T1b}$ coexist in a range of activity numbers. Particularly, they coexist at $Ra \approx 1.5$.



(a) Two homoclinic-like RPO members of the $HRPO_{T1a}$ family at $Ra = 1.35$ and 1.37 shown as solid red and blue curves, respectively, with their σ_y symmetry-related counterparts shown as dashed curves. And two heteroclinic-like PO members of the $HTPO_{T1a}$ family at $Ra = 1.39$ and 1.41 shown as black and green curves, respectively. These POs are also pre-periodic orbits with respect to σ_y , so their orbits are invariant under this symmetry. The black arrow shows the direction of increasing activity (Ra).



(b) Logarithmic scaling of period near homoclinic bifurcation in which the HRPOs disappear. Here, $A \approx 11.515$, $B \approx 40.69$, and $Ra_c \approx 1.381$.



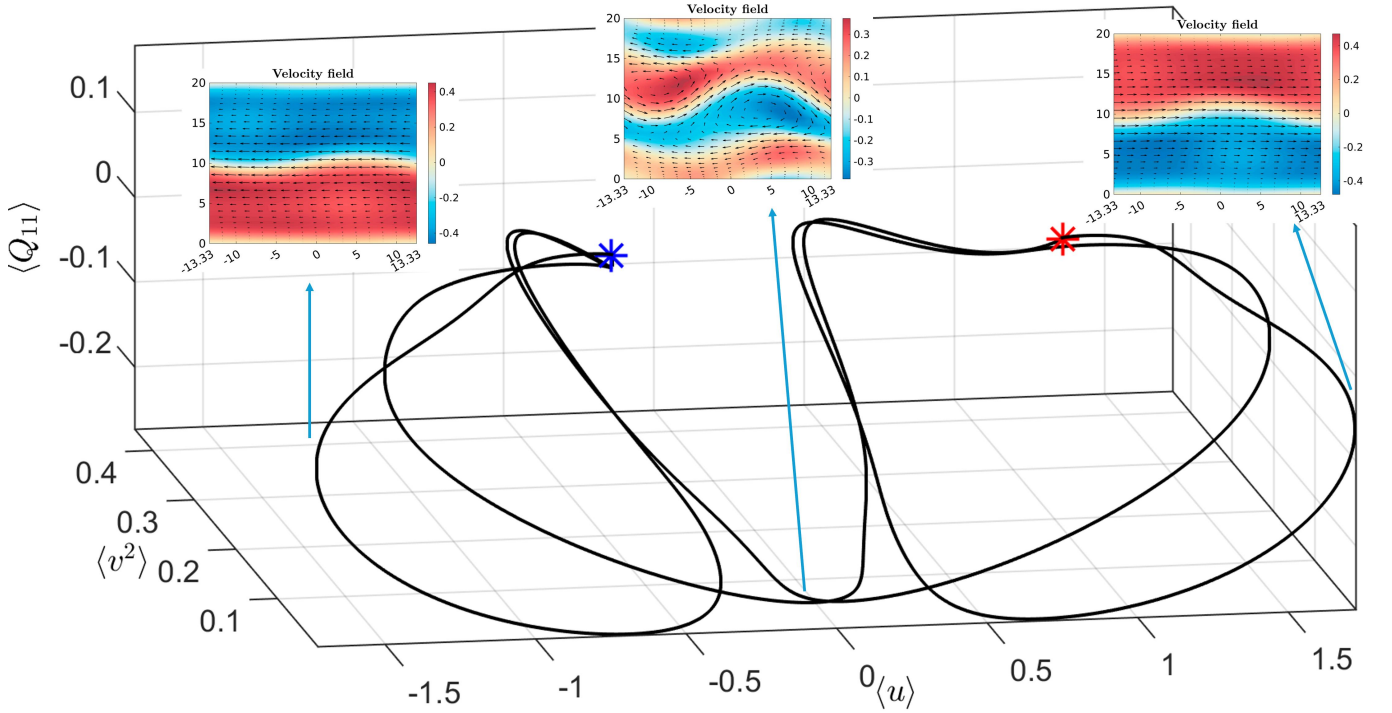
(c) Logarithmic scaling of period near heteroclinic bifurcation after which the HTPOs emerge. Here, $A \approx 33.865$, $B \approx -0.755$, and $Ra_c \approx 1.38$.

Figure 9: Two consecutive global bifurcations, both with logarithmic scaling consistent with homoclinic/heteroclinic bifurcations. The first (homoclinic) bifurcation results in the vanishing of homoclinic-like RPOs. The second (heteroclinic) bifurcation leads to emergence of heteroclinic-like POs. In both cases, the RPOs and POs collide with the UNI (and σ_y UNI) solution at the respective bifurcation points. Note that the estimated bifurcation values Ra_c are very close to each other.

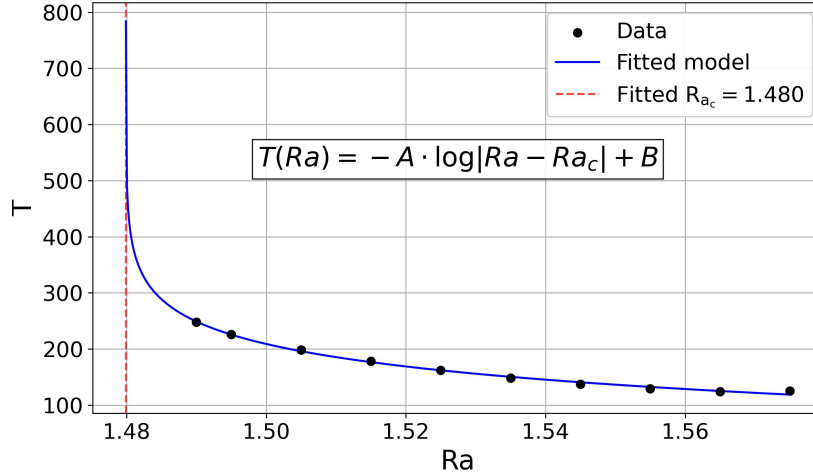
5. Secondary Bifurcations Associated with Higher Unstable Eigenvalues of UNI

Our analysis so far has been limited to bifurcations from the primary unstable eigenspace of UNI. As the activity number is increased to $Ra = 4.5$, a total of seven pairs of complex eigenvalues eventually cross the imaginary axis at various intermediate activity values. The corresponding secondary bifurcations give rise to additional ECSs, each embedded within a distinct symmetry subspace. While a full analysis is out of scope, it is crucial to identify how the symmetries of these other eigenspaces shape the bifurcation structure and the global dynamics deep into the turbulent regime.

Each crossing corresponds to a Hopf bifurcation, and the symmetries of each unstable 2D eigenspace are listed as



(a) A member of the second branch of heteroclinic-like periodic orbits, $HTPO_{T1b}$, which is σ_y -symmetric, shown close to the second heteroclinic bifurcation at $Ra \approx 1.5$, together with UNI and σ_y UNI, indicated by red and blue stars, respectively. Also shown are three velocity snapshots along the orbit: two exhibiting opposite unidirectional flows and one with a vortical flow state.



(b) Confirmation of the logarithmic scaling of period near the second heteroclinic bifurcation. Here, $A \approx 58.084$, $B \approx -18.039$, and $Ra_c \approx 1.48$.

Figure 10: A second branch of heteroclinic-like periodic orbits, $HTPO_{T1b}$, and associated logarithmic scaling near the second heteroclinic bifurcation point.

isotropy groups in Table III in the Appendix. These symmetries constrain the nature of solutions that can emerge from bifurcations. Although it is not practical to trace every secondary bifurcation, we observe that RPOs with the corresponding symmetry commonly emerge, often via bifurcation scenarios similar to the SNIPER bifurcation analyzed in detail for the first eigenvalue pair.

For instance, the second unstable eigenvalue pair leads to a bifurcation scenario closely resembling that of the first pair, resulting in a branch of traveling waves with isotropy group $\Sigma_{p2(v)}$ (Fig. 11). This branch, which looks like two copies of the TW (from the first pair) stacked horizontally, undergoes a saddle-node bifurcation and subsequently a SNIPER bifurcation. The result is a branch of homoclinic-like RPOs that we call $HRPO_{T2a}$. However, in contrast

to the first eigenvalue pair, no subsequent heteroclinic connections between UNI and σ_y UNI were observed upon increasing the activity.

The branches arising from bifurcations associated with the remaining eigenvalues populate the phase space with solutions that inherit the corresponding underlying symmetries. In particular, the second and third unstable eigenspaces have the symmetry $\tau_x(L/2)$, and therefore give rise to solutions confined to the invariant subspace defined by this transformation. As we shall see in the following sections, this subspace plays a crucial role in shaping the dynamics of reversals in the turbulent regime.

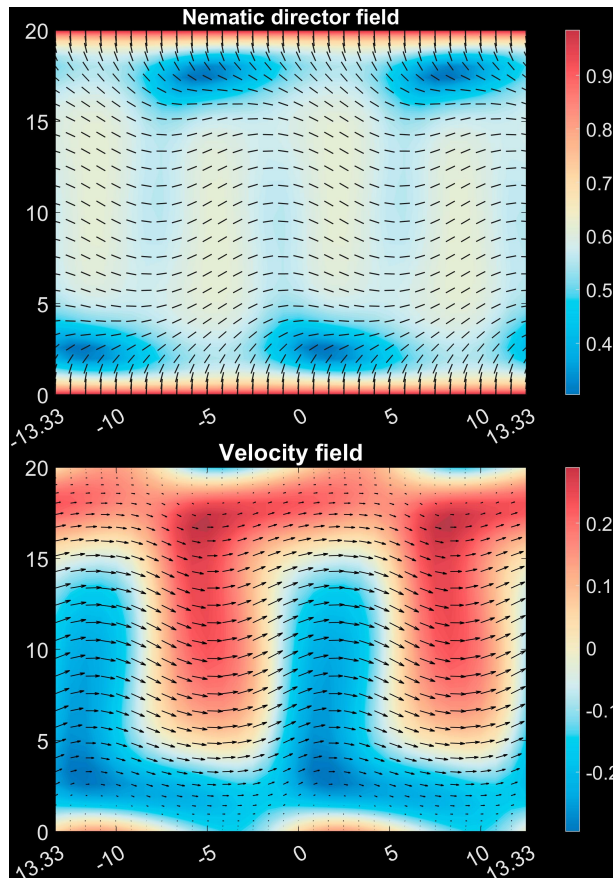


Figure 11: A snapshot of the nematic director and velocity fields of a traveling wave solution with isotropy group $\Sigma_{p_2(U)}$, computed at $R_a = 1.0$. This solution originates from UNI via an equivariant Hopf bifurcation at $R_a \approx 0.97$, associated with the second complex-conjugate pair of eigenvalues crossing the imaginary axis.

E. Secondary bifurcations from LAN

In this subsection, we carry out an equivariant bifurcation analysis of the secondary instabilities emerging from the LAN state in MFU A. Our main aim is to clarify the origin of dynamically relevant vortex–lattice–like ECSs. Oscillatory vortex states have been reported in several experimental and numerical studies [9, 26, 27, 34, 61]; in particular, Wagner *et al.* found vortex patterns whose characteristic length scale adjusts to the channel aspect ratio. A subset of these, termed ‘dancing disclinations’ [9, 68–70], exhibit $+1/2$ defects that form a space–time braid, and appear as POs and RPOs [26, 27]. Here we show that the relevant vortex–lattice solutions are not connected to the previously identified secondary bifurcations of the UNI equilibrium, and instead most likely arise from secondary bifurcations of the LAN equilibrium.

1. One-vortex equilibria

We consider the isotropy subgroup of LAN, $\Gamma_{LAN} = \mathbb{Z}_2(\sigma_x\sigma_y) \rtimes SO(2) \cong O(2)$, as the base group for the equivariant analysis of bifurcations from LAN. The LAN solution first loses stability when a pair of real eigenvalues simultaneously crosses the imaginary axis at $R_a \approx 0.85$. Since the eigenvalues are real, this is a steady bifurcation, and the two-dimensional center subspace is taken as \mathbb{R}^2 . In this center subspace, we can choose v_1 and v_2 such that the reflection $\sigma_x\sigma_y$ is represented by

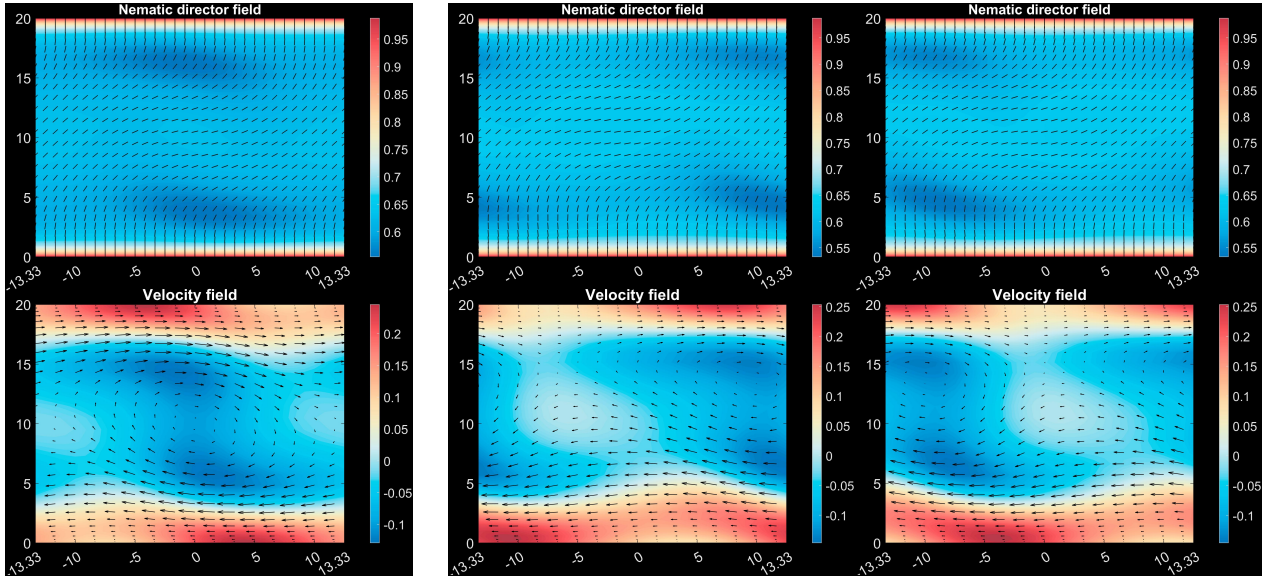
$$\sigma_x\sigma_y = \begin{pmatrix} 1 & 0 \\ 0 & -1 \end{pmatrix}. \quad (9)$$

This is a reflection about the x -axis, which is also its fixed-point subspace. The translations act as the rotation matrices,

$$R(\phi) = \begin{pmatrix} \cos \phi & -\sin \phi \\ \sin \phi & \cos \phi \end{pmatrix}, \quad \phi = \frac{2\pi\ell}{L}, \quad \ell \in [0, L), \quad \phi \in [0, 2\pi). \quad (10)$$

Every subgroup generated by the conjugate reflection $\Sigma_\phi = R(\phi)\sigma_x\sigma_yR(-\phi)$ is axial, and has the line (passing through origin) with slope ϕ as its fixed point subspace. The EBL predicts an infinite number of (pitchfork) branches of solutions bifurcating from LAN, one for each ϕ , and possessing the corresponding Σ_ϕ symmetry.

Indeed, numerically we found a branch of steady one-vortex equilibrium solution (see Fig. 12a), invariant under the reflection $\Sigma_0 = \sigma_x\sigma_y$, emerging from the LAN equilibrium. The other branches of solutions with $\Sigma_{\phi>0}$ symmetry are simply translations of this one-vortex solution. These solutions form a group orbit of equilibria, i.e., a relative equilibrium.



(a) The nematic director and velocity field of a one-vortex **equilibrium** solution bifurcated from the LAN at $R_a = 0.85$. Its set of spatial translations constitutes a **relative equilibrium**.

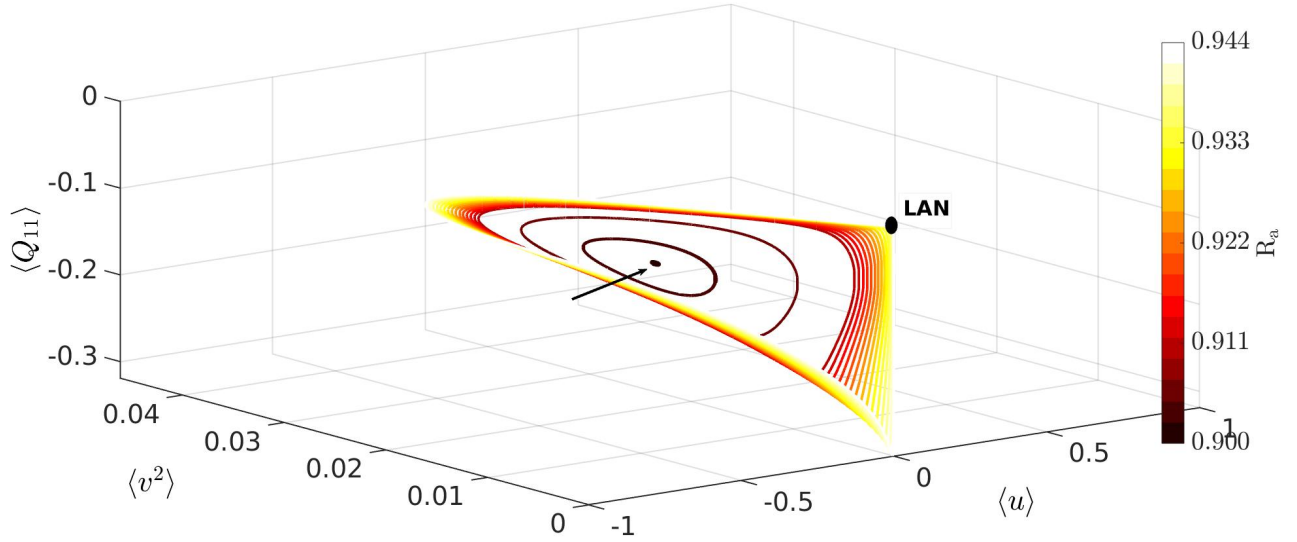
(b) Two snapshots from a time simulation at $R_a = 0.851$ of the stable **one-vortex wave** traveling to the left, separated by an interval of $t = 50\tau$. This wave branch emerges via a steady bifurcation (of the corresponding normal vector field) from the one-vortex relative equilibrium.

Figure 12: One-vortex solutions: relative equilibria and traveling wave originating from the LAN solution in MFU A.

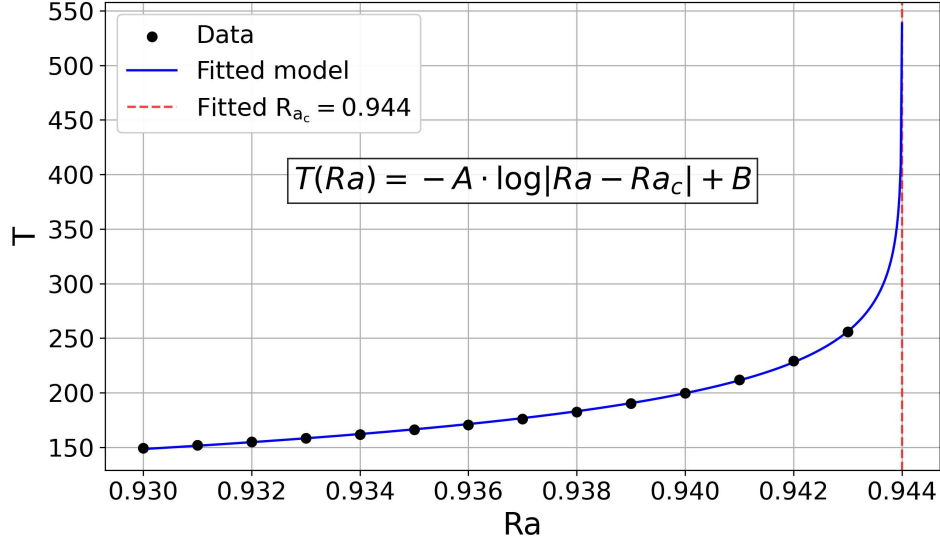
2. One-vortex traveling waves via symmetry-breaking bifurcation

The steady vortex solutions are stable for a small range of activity, $0.85 \lesssim Ra \lesssim 0.851$. Like in the case of TW discussed earlier, the bifurcation occurring at $Ra \approx 0.851$ from the group orbit of the one vortex solution requires analyzing the vector field normal to the group orbit.

We denote any one-vortex equilibrium by X_0 , and consider the corresponding kernel of Jacobian normal vector field, $d_X H(X_0, 0)$, which is one-dimensional and associated with a real eigenvalue in this case. The isotropy group acts nontrivially on this subspace, with the action of $\sigma_x \sigma_y$ given by -1 [32, 63]. To apply the Equivariant Branching Lemma (EBL), we identify the axial group $\Sigma = \{I\}$, and predict a branch of solution with *no symmetry*. To find the group orbit of this solution, we apply Theorem 3 with $\Sigma = \{I\}$ with $\Gamma = O(2)$, the base group for LAN. This yields $N(\{I\})/\{I\} \cong O(2)$, which implies that the group orbit of this bifurcating solution is rank 1, and hence a *traveling (rotating) wave*, consistent with the general analysis for $O(2)$ -equivariant systems [63].



(a) Family of periodic solutions bifurcating from the one-vortex steady state via a symmetry-preserving Hopf bifurcation, with the arrow indicating the parent steady solution. The colormap indicates activity. These periodic orbits grow in size as the activity is increased, and eventually collide with LAN and disappear via a homoclinic bifurcation.



(b) Logarithmic fit of the period near the homoclinic bifurcation, consistent with theory. Here, $A \approx 40.880$, $B \approx -26.107$, and $Ra_c \approx 0.944$.

Figure 13: One-vortex standing wave POs bifurcating from the steady state and terminating at a homoclinic bifurcation with LAN.

Numerically, we found exactly such a traveling wave solution at $Ra \approx 0.851$, which we call *one-vortex traveling wave* (see Fig. 12b). As predicted, this traveling wave has no symmetry. This solution closely resembles the traveling vortices observed in contractile active polar fluids [61]. Note that unlike the UNI case, this TW does *not* arise from a Hopf bifurcation, and this bifurcation is sometimes referred to as a ‘drift-pitchfork’ bifurcation [20, 71]. We also note that the $ZF \rightarrow LAN \rightarrow$ One-vortex equilibrium \rightarrow one-vortex TW sequence is closely related to the bifurcation scenario observed for one-dimensional excitable media [71].

To the best of our knowledge, stable and coherent vortical traveling wave solutions have not been previously reported in active nematics. While active nematics are known to exhibit complex turbulent states characterized by transient vortices, the existence of stable, isolated traveling vortex waves represents a novel finding in this context.

3. One-vortex standing waves via symmetry-preserving bifurcation

The one-vortex TWs are solutions with no spatial symmetry. However, the previously reported dancing disclination solutions which are vortex dominated POs usually have the $\sigma_x \sigma_y$ symmetry [27]. To understand their origin, we look for symmetry-preserving bifurcations of the one-vortex equilibrium. We find that this equilibrium undergoes a second bifurcation at $Ra \approx 0.9$, when a complex pair of eigenvalues crosses the imaginary axis. The symmetry group $\Gamma = \mathbb{Z}_2(\sigma_x \sigma_y)$ again acts trivially on the center subspace of the vector field H normal to the group orbit.

Proposition 1 yields that H undergoes a Hopf bifurcation to a unique time-periodic solution. To obtain the group orbit of the bifurcating solution, we apply Theorem 3 with $\Sigma_{X_0} = \mathbb{Z}_2(\sigma_x \sigma_y)$ being the isotropy subgroup of the one-vortex solution (see Remark following Theorem 3), and $\Gamma = \Gamma_{LAN}$, to get $k = \text{rank} \left(\frac{\mathbb{Z}_2 \times \mathbb{Z}_2}{\mathbb{Z}_2} \right) + 1 = \text{rank}(\mathbb{Z}_2) + 1 = 1$. This rules out RPOs (which have dimension 2), and implies that the bifurcating solutions of the full vector field are either standing waves (POs) or traveling waves (POs). An isotropy subgroup calculation similar to that performed for Hopf bifurcation from UNI shows that these solutions are in fact standing waves. These periodic solutions lie in the subspace defined by $\langle u \rangle = 0$ and persist over a finite range of activity numbers. However, we find that these POs, while having the same symmetry as the dancing disclination solutions, do not have the characteristic braiding of $+\frac{1}{2}$ defects of the latter [70].

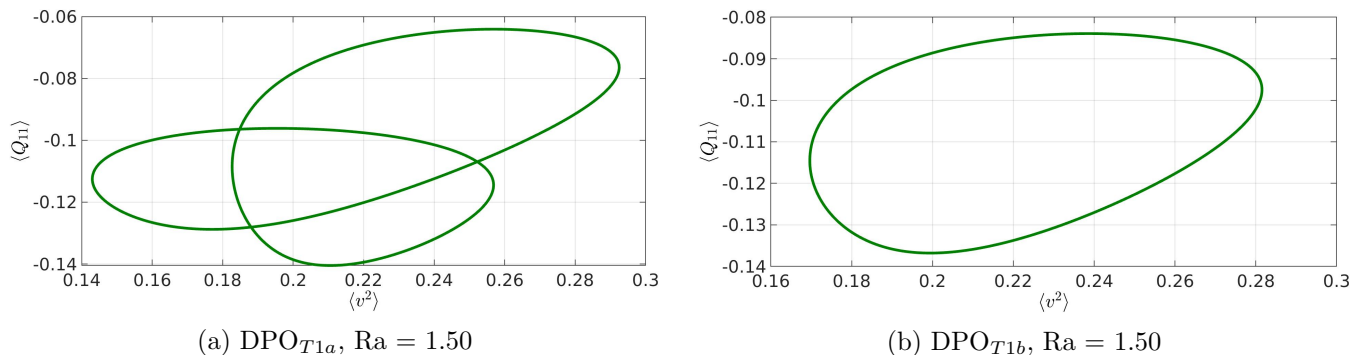


Figure 14: Two dancing-disclination-like POs (DPOs) that co-exist at $Ra = 1.5$, projected onto the reduced phase space $(\langle Q_{11} \rangle, \langle v^2 \rangle)$. Both solutions lie in the $\langle u \rangle = 0$ subspace (i.e., no net streamwise flow) due to the $\sigma_x \sigma_y$ symmetry.

4. Homoclinic bifurcation of the one-vortex POs and the emergence of dancing disclination solutions

As the activity is increased further, the size of one-vortex POs grows; the PO family eventually collides with the LAN and disappears via a homoclinic bifurcation at $Ra \approx 0.944$, as shown in Fig. 13a. The logarithmic divergence of the period near the homoclinic bifurcation confirms this observation (see Fig. 13b).

On the other side of the homoclinic bifurcation, we find a branch of one-vortex unstable POs with symmetry $\sigma_x\sigma_y$ around $R_a \approx 0.96$. This family, which we call DPO_{T1a} , consists of exactly the dancing disclination type POs with the required braiding characteristics. While we currently do not understand the exact mechanism that connects the homoclinic bifurcation described above with the emergence of this branch, we hypothesize that the two are related due to their shared symmetry. Similarly, there exists another branch of periodic orbits invariant under the same symmetry, denoted DPO_{T1b} , which also exhibits dancing defects. This branch of POs can be continued down to activity as low as $R_a = 0.74$. A detailed analysis of the origin of these two branches of solutions is left for future work.

5. Secondary Bifurcations Associated with Higher Unstable Eigenvalues of LAN

So far, our analysis has been limited to bifurcations associated with the first unstable eigenspace of LAN. As the activity number is varied from $R_a \approx 0.85$ to $R_a \approx 4.5$, a total of eight (equal) pairs of real eigenvalues eventually cross the imaginary axis. The isotropy subgroups of these eight unstable 2D eigenspaces are listed in Table IV in the Appendix. While the study of all bifurcations is outside the scope of this work, we briefly discuss the bifurcations from the second unstable eigenspace, since these solutions play an important role in the turbulent regime we analyze later in this paper.

This second pair of unstable eigenvectors possesses the $\tau_x(L/2)$ symmetry. The sequence of bifurcations is analogous to those of the first pair, and the bifurcating solutions possess the extra $\tau_x(L/2)$ symmetry. The steady solution is a two-vortex equilibrium that looks like two copies of the one-vortex equilibrium stacked along the x -axis. Additionally, there exists a branch of periodic orbits, denoted as PO_{T2a} (see Fig. 15), with symmetry $\sigma_x\sigma_y\tau_x(L/2)$ that cycles between a LAN-like and two-vortex like state. We anticipate that solutions associated with higher modes could bifurcate from LAN through similar mechanisms.

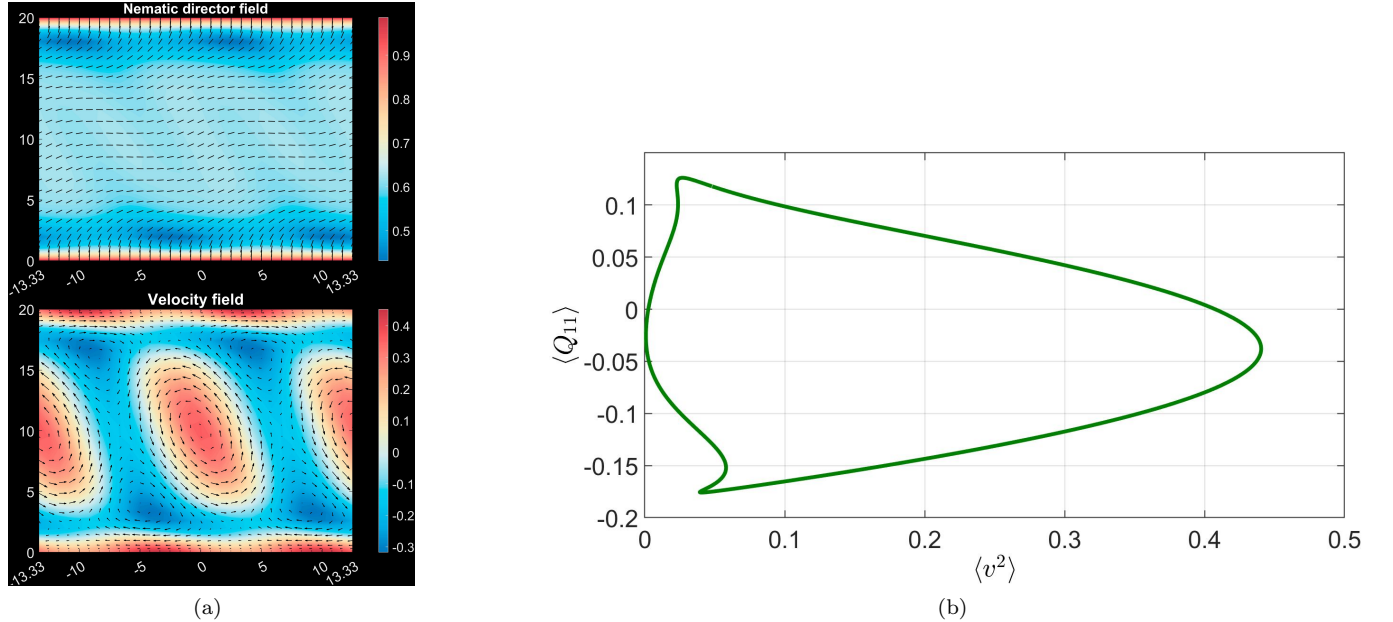


Figure 15: Visualization of PO_{T2a} at $R_a = 2.25$. (a) A snapshot of the nematic director and velocity fields, where its $\sigma_x\sigma_y\tau_x(L/2)$ symmetry is apparent. (b) Projection onto the reduced phase space: $(\langle Q_{11} \rangle, \langle v^2 \rangle)$. This PO lies in the $\langle u \rangle = 0$ subspace (i.e., no net streamwise flow) due to the $\sigma_x\sigma_y$ symmetry.

IV. TRANSIENT FLOW REVERSALS IN PRETURBULENT FLOW

In section III, we uncovered the origin of several key ECSs that emerge from, or are related to, bifurcations of the UNI and LAN equilibria. We now discuss how these ECSs and their invariant manifolds facilitate robust, transient flow reversals in the preturbulent regime, where reversals are characterized by switching between near-unidirectional states located in the regions $\langle u \rangle < 0$ (left) and $\langle u \rangle > 0$ (right), respectively. By transient, we mean that each trajectory switches direction a finite number of times before entering the basin of attraction of a regular attractor (i.e. a stable ECS) or a chaotic attractor. By robust, we mean that the reversal mechanism persists for an open interval of activity values.

A. Transient Reversal Dynamics at Low Activity: Organizing ECSs and Heteroclinic Connections

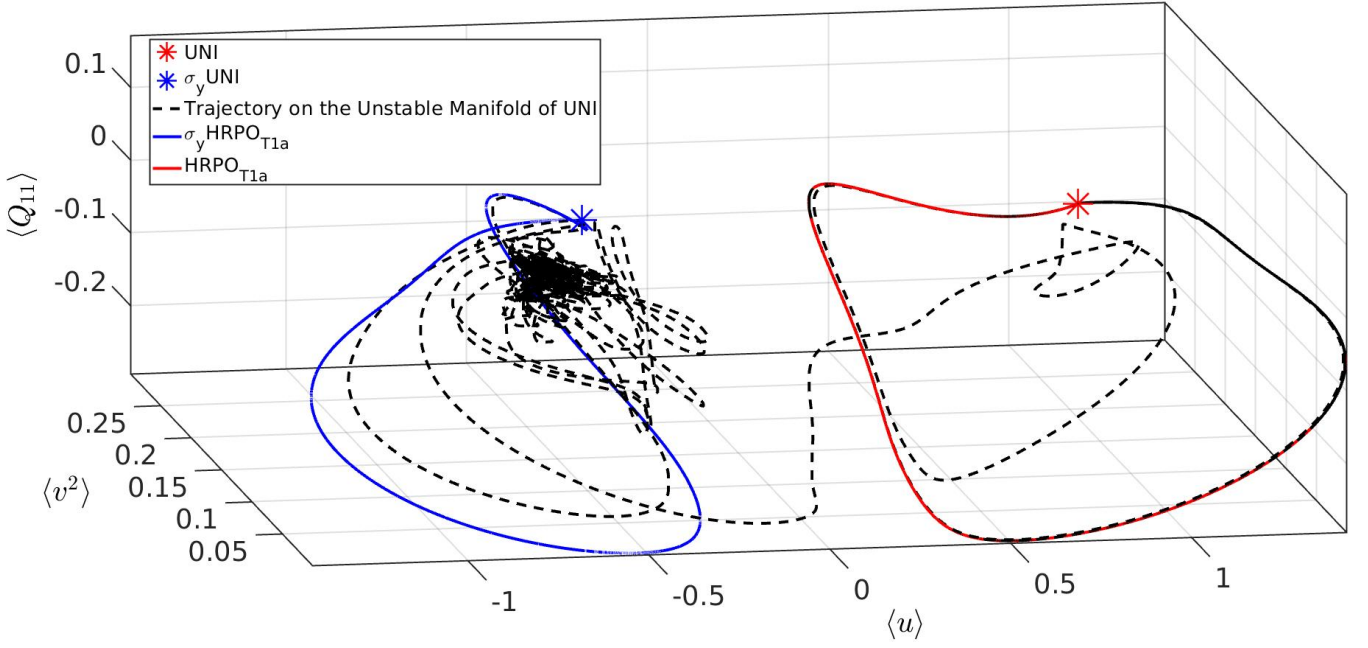
We focus on trajectories that begin near UNI or its symmetry counterpart σ_y UNI. When these ECSs are stable, all nearly uniaxial initial conditions decay to them. When these ECSs lose stability, the homoclinic-like RPOs (HRPO_{T1a} and $\sigma_y\text{HRPO}_{T1a}$) become the attractors instead, up to $R_a \approx 1.11$. Beyond this activity, and before the heteroclinic bifurcation that occurs at $R_a \approx 1.38$, the two RPOs are unstable. The unstable manifolds of these RPOs and the heteroclinic connections between these ECSs and the DPOs shape the flow between nearly uniaxial states.

At $R_a = 1.24$ for instance, these ECSs co-exist with a localized chaotic attractor (and its σ_y copy) that has been reported earlier [26]. Perturbing UNI along its four unstable directions reveals the two main mechanisms for flow reversals facilitated by heteroclinic connections. The first mechanism, which requires no mediators to cross from right to left, is shown in Fig. 16a. The trajectory shadows the heteroclinic connections $\text{UNI} \rightarrow \text{HRPO}_{T1a} \rightarrow \sigma_y\text{HRPO}_{T1a}$, and eventually settles into the localized chaotic attractor on the left. The second mechanism, shown in Fig. 16b, shadows the heteroclinic connections $\text{HRPO}_{T1a} \rightarrow \text{DPO}_{T1a}$ to end up in the same localized chaotic attractor. The rest of trajectories originating near UNI (resp. $\sigma_y\text{UNI}$) do not exhibit reversals and settle onto the chaotic attractor on the right (resp. left).

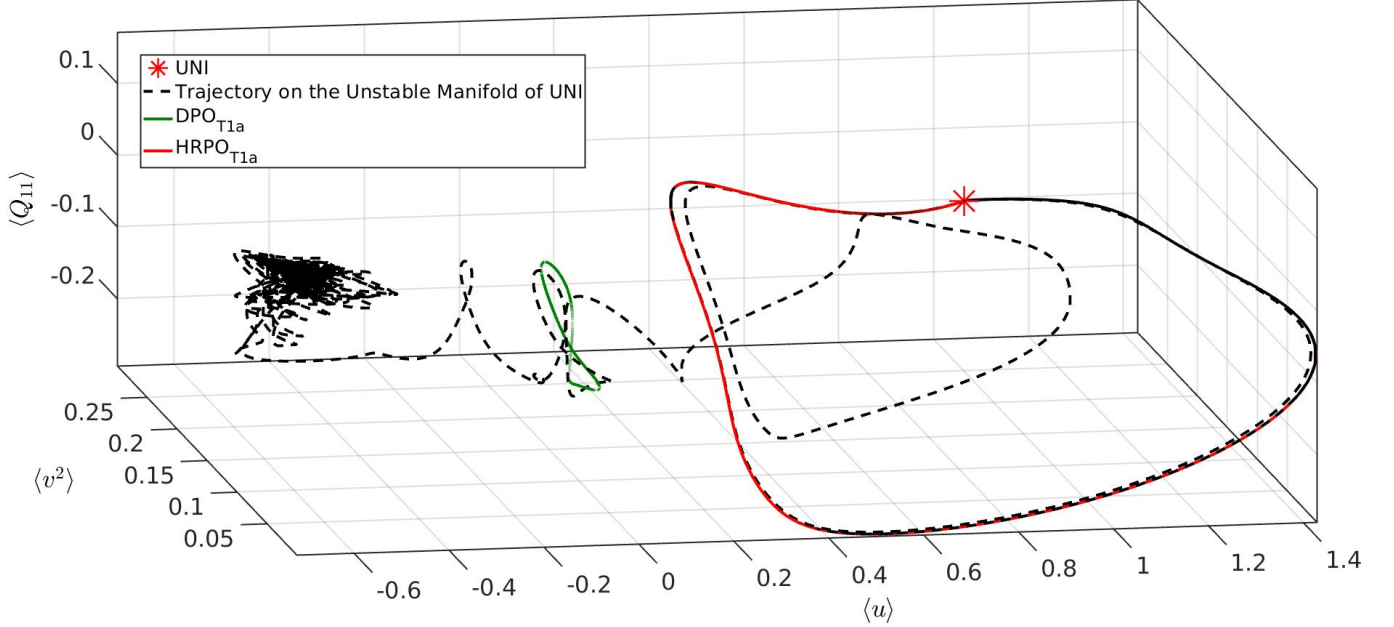
Increasing the activity further reveals additional reversal mechanisms. At $R_a = 1.5$, for instance, we observe that eight fundamental ECSs organize the reversal dynamics between left- and right-flowing states. These include the two heteroclinic-like HTPO_{T1a} and HTPO_{T1b} , the homoclinic-like HRPO_{T2a} , the DPO_{1a} and DPO_{1b} associated with LAN, and three additional RPOs. These new RPOs, which we call $\text{DRPO}_{T1a,b,c}$, likely emerge from bifurcations of the DPO branches. These are the drifting versions of dancing disclination solutions, as first reported in [26]. Interestingly, at this activity number, no localized chaotic attractor was found. Instead, the three DRPOs occupy approximately the same region of phase space that was previously occupied by the chaotic attractor, and DRPO_{T1c} is the only attractor in this region.

By perturbing UNI along its two pairs of unstable directions at $R_a = 1.5$, we obtain trajectories that initially shadow either HTPO_{T1b} or HRPO_{T2a} . In the first case, the initial transient consists of repeated reversals between the two nearly uniaxial flow states, due to the heteroclinic nature of HTPO_{T1b} . Eventually, the trajectory diverges from HTPO_{1b} and either moves directly to the region populated by the three DRPOs, or passes near the DPO_{T1a} before reaching a symmetry instance of the DRPO family as shown in Fig. 17a. In the second case, after transiently shadowing HRPO_{T2a} , a trajectory can undergo a reversal event by a direct heteroclinic connection to the DRPO_{T1a} copy on the opposite side, or via an intermediate heteroclinic connection to DPO_{T1a} . All trajectories at $R_a = 1.5$ eventually end up in the attractor DRPO_{T1c} or its σ_y copy.

In summary, for low activity numbers, three main types of reversal mechanisms are identified: the first involves heteroclinic connections originating from HRPOs or HTPOs to the relevant attractor; the second mechanism is similar but with DPOs serving as mediators; and the third arises when trajectories shadow either of the two HTPOs themselves. When both the HTPOs exist, we observe that HTPO_{T1b} is more dominant of the two in influencing trajectories originating from perturbations of UNI. Animations of representative reversal trajectories and their shadowed ECS



(a) Mechanism 1: Flow reversal with no DPO mediator. The black dashed trajectory, initialized near UNI along its unstable manifold, successively follows the heteroclinic connections $\text{UNI} \rightarrow \text{HRPO}_{T1a} \rightarrow \sigma_y \text{HRPO}_{T1a}$ and eventually settles into the localized chaotic attractor.



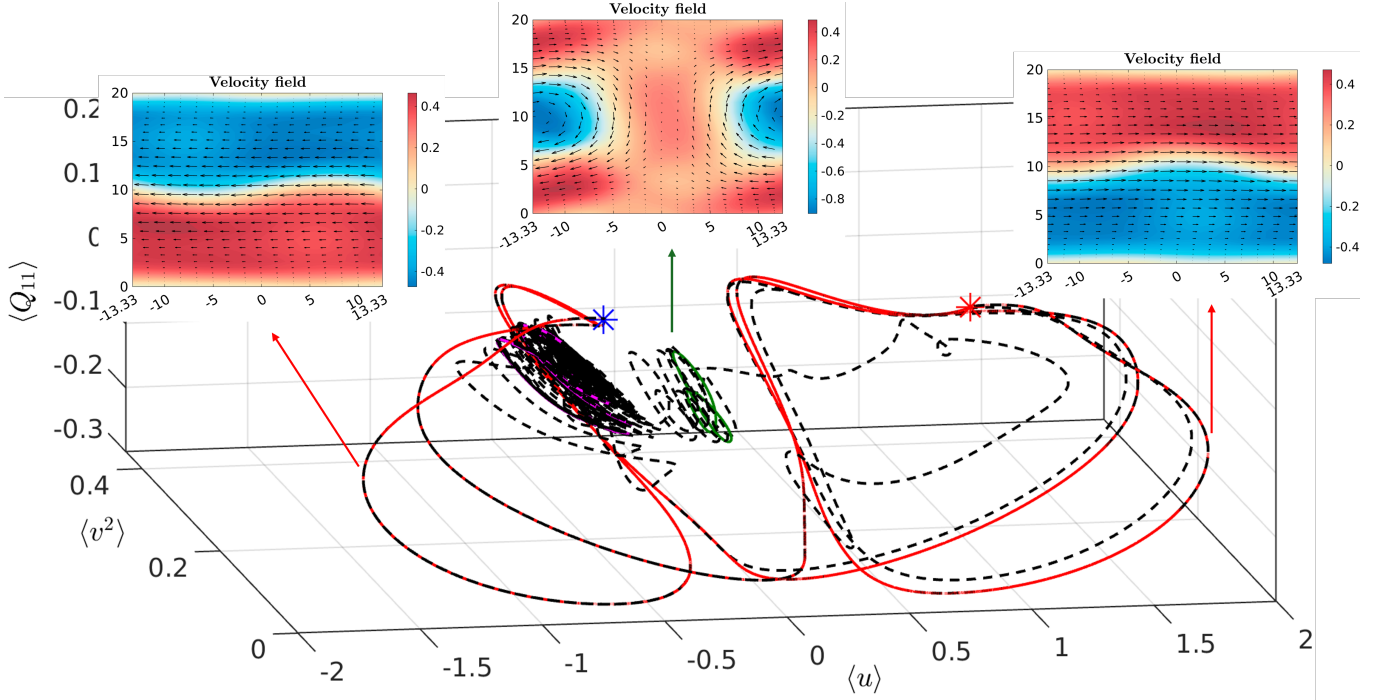
(b) Mechanism 2: Flow reversal using the DPO_{T1a} as mediator. The black dashed trajectory follows the heteroclinic connections $\text{UNI} \rightarrow \text{HRPO}_{T1a} \rightarrow \text{DPO}_{T1a}$ and settles into the localized chaotic attractor.

Figure 16: Two main mechanisms for flow reversals observed at $R_a = 1.24$ by perturbing UNI.

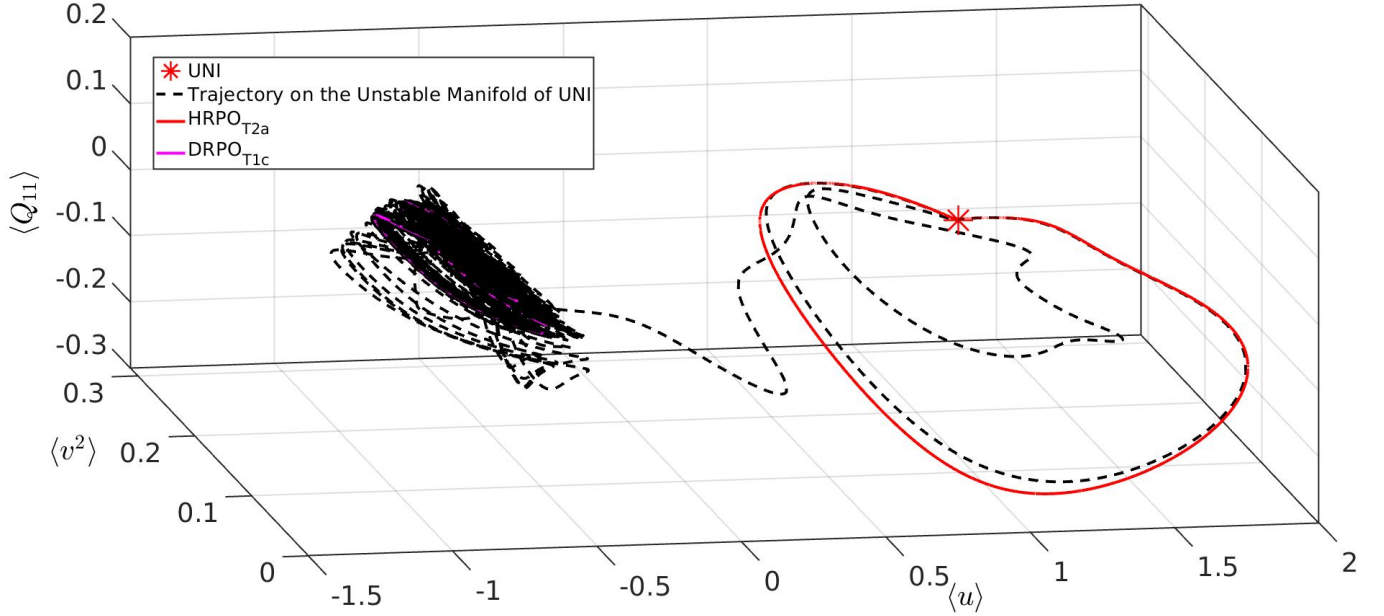
solutions are provided in the Supplemental Material.

B. Transient Flow Reversals at Higher Activity and the Path Toward Turbulence

While tracking bifurcations all the way into the turbulent regime is impractical, we make a few observations regarding the role of the various symmetries in shaping the phase space structure as the activity number is increased.



(a) Mechanism 3 via $HTPO_{T1b}$. The Black dashed trajectory, initiated on the unstable manifold of UNI, first shadows $HTPO_{T1b}$, and then follows the heteroclinic connections $HTPO_{T1b} \rightarrow DPO_{T1a} \rightarrow DRPO_{T1a} \rightarrow DRPO_{T1b} \rightarrow DRPO_{T1c}$. The various ECS visible in the figure are $HTPO_{T1b}$ (red), DPO_{T1b} (green) and $DRPO_{T1c}$ (magenta). Both $DRPO_{T1a}$ and $DRPO_{T1b}$ are hidden beneath the final segment near $DRPO_{T1c}$. Also shown are representative snapshots of UNI-like and one-vortex-like flow states during the reversal in this preturbulent regime.



(b) Mechanism 1 using $HRPO_{T2a}$. The black dashed trajectory follows the heteroclinic sequence $UNI \rightarrow HRPO_{T2a} \rightarrow DRPO_{T1a} \rightarrow DRPO_{T1b} \rightarrow DRPO_{T1c}$.

Figure 17: Main mechanisms of flow reversals at $R_a = 1.5$ observed by perturbing UNI along its four dimensional unstable subspace. (a) A mechanism that uses the $HTPO_{T1b}$ with DPO_{T1a} as the mediator. (b) A mechanism using $HRPO_{T2a}$ without $DPOs$ as mediators.

We have seen earlier that solutions with symmetries conjugated to $\sigma_x\sigma_y$, and branches bifurcating from them, provide mechanisms for reversal. By following the DPO_{T1a} branch into the higher activity region, we observe that at $R_a \approx 2.38$, this branch becomes stable. Then, at $R_a \approx 3.29$, it undergoes a period-doubling bifurcation that breaks the $\sigma_x\sigma_y$ symmetry, giving rise to a stable preperiodic orbit (see Fig. 18a). The resulting solution represents, by itself, a stable mechanism for periodic flow reversals about $\langle u \rangle = 0$. As the activity number reaches $R_a = 4.0$, new ECSs emerge from a sequence of bifurcations related not only to DPO_{T1a} but also to nearby solutions, which increasingly populate this region of phase space in the form of a localized chaotic attractor shown in Fig. 18b. This sequence preludes the birth of the set \mathcal{Y} at $R_a = 4.5$ (see Fig. 20), within which solutions related to DPO_{T1a} and their manifolds continue to play an important role in mediating reversals.

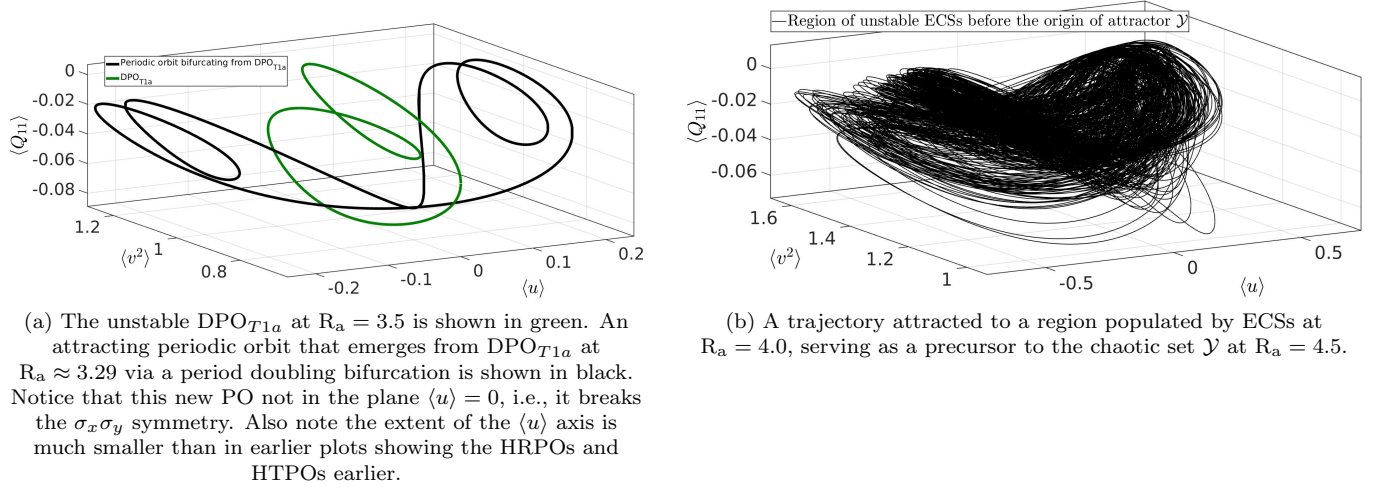


Figure 18: Phase space visualizations illustrating the evolution from a periodic orbit to the onset of the chaotic set \mathcal{Y} .

The other set of ECSs that remain relevant at higher activity are those with $\tau_x(L/2)$ symmetry, emerging from bifurcations of the UNI and LAN branches. In particular, at $R_a = 3.75$, there exists a periodic orbit that is stable within the invariant subspace under this symmetry and attracts perturbations of UNI along the second and third pairs of unstable eigenvectors. It seems to be related to a secondary bifurcation of PO_{T2a} that breaks the $\sigma_x\sigma_y$ symmetry. Interestingly, at $R_a \approx 4.0$, no ECSs within this subspace are stable, and a new chaotic set emerges. We denote this set by \mathcal{X} , as shown in Fig. 20. At this stage, trajectories initialized from UNI and perturbed within the four-dimensional subspace composed of the 2D second and third unstable eigenspaces can cross into the other region of phase space, near $\sigma_y\text{UNI}$, and switch recurrently between these two states.

The chaotic sets \mathcal{X} and \mathcal{Y} exhibit reversals between regions where the flow velocity has a mean value $\langle u \rangle$ that persistently oscillates about positive and negative values, respectively. In the following section, we analyze these attractors to elucidate the mechanisms responsible for flow reversals in the MFU at $R_a = 4.5$.

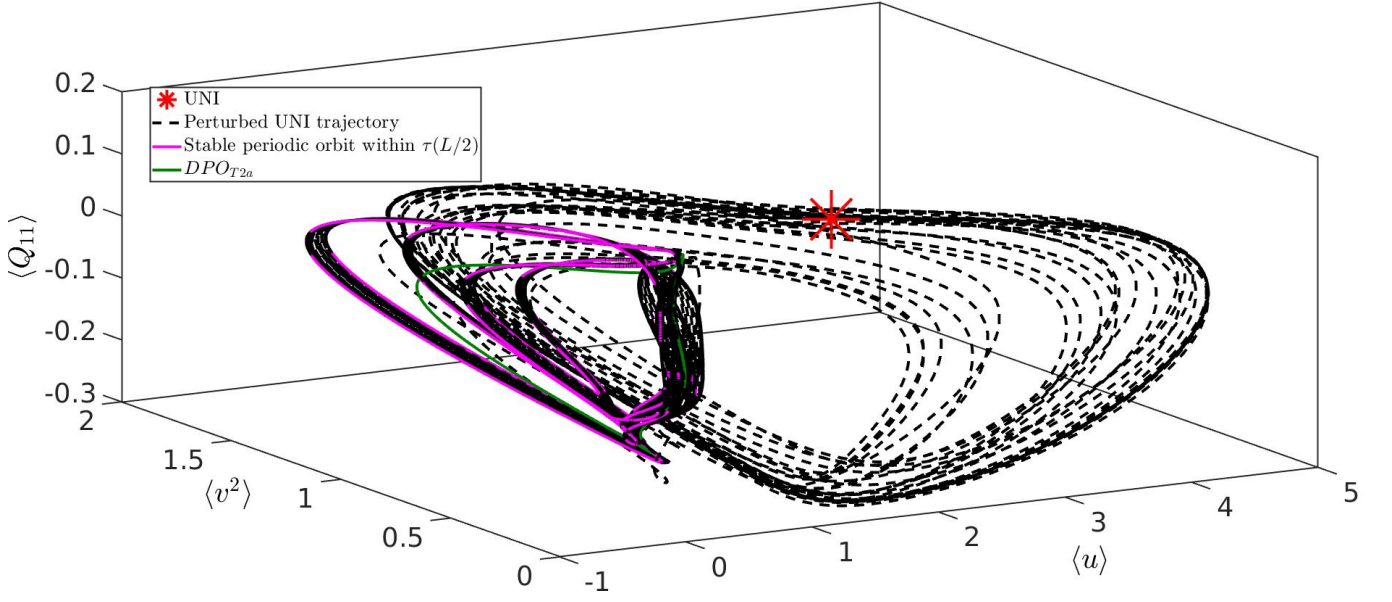


Figure 19: At $R_a = 3.75$, the black dashed trajectory perturbed from UNI settles into a periodic orbit (magenta) that is stable within the $\tau_x(L/2)$ invariant subspace. This periodic orbit seems to have originated from secondary bifurcations of $PO_{T_{2a}}$. The periodic orbit $PO_{T_{2a}}$ is shown in green.

V. FLOW REVERSAL MECHANISMS IN TURBULENCE: TWO-WAY PERSISTENT REVERSALS

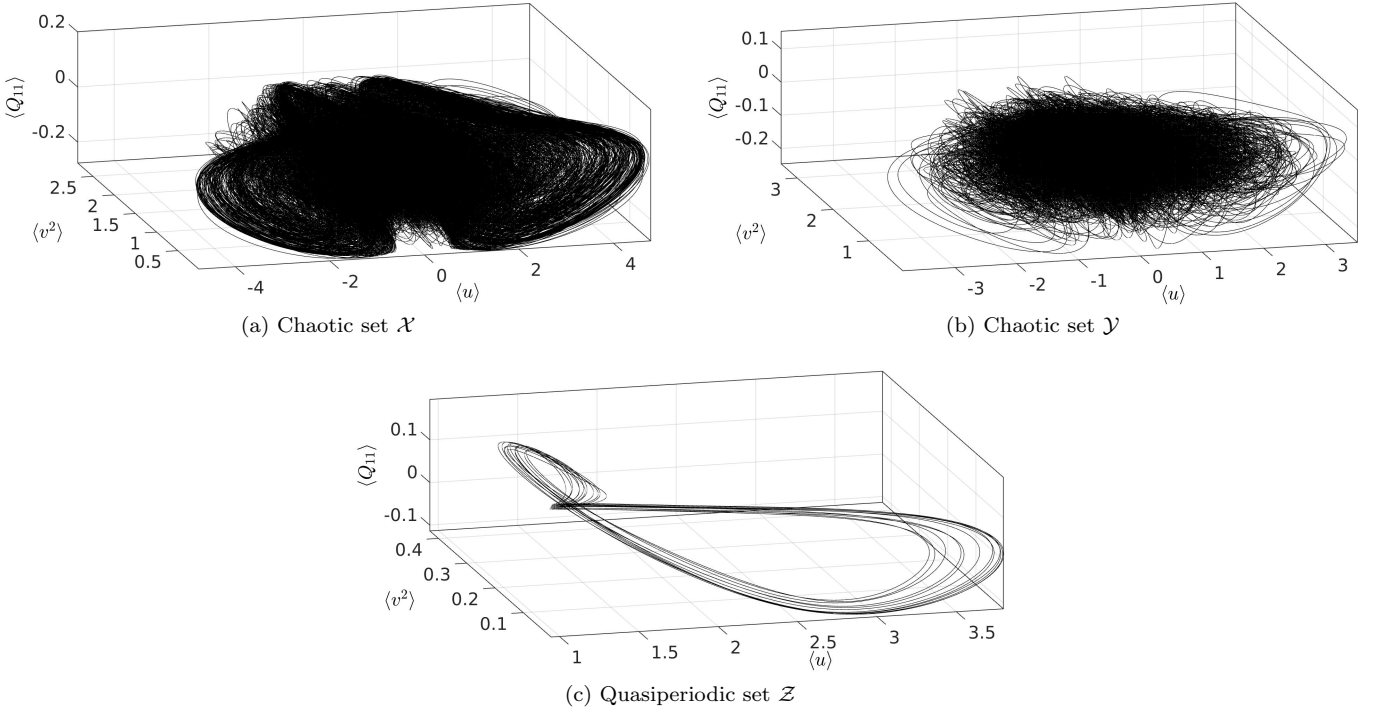


Figure 20: All perturbations of UNI along its unstable manifold in the MFU A end up in one of the three sets \mathcal{X} , \mathcal{Y} and \mathcal{Z} . The top row shows the chaotic sets \mathcal{X} and \mathcal{Y} . The bottom row shows the quasiperiodic set \mathcal{Z} .

The results presented for the preturbulent regime, where we have shown that the dynamical trajectories are shaped by the ECSs and their invariant manifolds, motivate us to investigate the nature of the reversal mechanisms within

the turbulent regime. In the original full-channel configuration (length \tilde{L}), however, Wagner *et al.* [27] explored the turbulent regime at $R_a = 4.5$, reporting no evidence of shadowing among the 210 distinct ECSs and their discrete-symmetry counterparts, leaving the role of ECSs in the dynamics still unclear. In contrast, our use of smaller domains as MFUs allows us to identify shadowing events in a simplified system with fewer solutions and reduced complexity. These detected shadowing events highlight the pathways through which chaotic trajectories undergo reversals. In this section, we consider two MFUs: the MFU A which has been analyzed throughout the previous sections with length $L_A = \tilde{L}/3$, and its halved version MFU B with $L_B = \tilde{L}/6$. We explore the following questions in the following:

- Q1: Where do typical trajectories end up at $R_a = 4.5$ in the two MFUs ?
- Q2: Do the trajectories that end up in one of the two chaotic sets \mathcal{X} or \mathcal{Y} shadow the ECSs embedded in those sets at $R_a = 4.5$?
- Q3: What are the symmetries and possible origins of ECSs embedded in the chaotic sets ?

The UNI in the MFU A at $R_a = 4.5$ has seven complex pairs of unstable eigenvalues. Perturbations of the UNI within the union of eigenspaces corresponding to the first, fourth and fifth pairs evolve towards the chaotic set \mathcal{Y} , while perturbations within the union of eigenspaces of the second and third pairs evolve towards the chaotic set \mathcal{X} . In the remaining two directions, perturbations lead to a stable quasiperiodic orbit in the MFU, denoted by \mathcal{Z} , see Fig. 20.

We find that an arbitrary perturbation (i.e., with no symmetry) always ends up in \mathcal{Y} , indicating that in MFU A, \mathcal{Y} is the only almost-global attractor while the other two sets \mathcal{X} and \mathcal{Z} are saddles. Motivated by the apparent two-fold translation (i.e., $\tau_x(L_A/2)$) symmetry of \mathcal{X} itself, we verify that in fact, all initial conditions with $\tau_x(L/2)$ symmetry end up in \mathcal{X} in MFU A. Hence, we also analyze dynamics in the smaller MFU B, where \mathcal{Y} is eliminated due to lack of two-fold translation symmetry, and we find that the halved-version of \mathcal{X} is the only almost-global attractor that attracts arbitrary initial conditions almost surely. The quasiperiodic \mathcal{Z} , while still present in MFU B, again only attracts a measure zero set of trajectories that have the additional translation symmetry. Table I summarizes this discussion and answers Q1 posed above. Now we turn to answering Q2 and Q3.

A. Establishing shadowing within the chaotic sets \mathcal{X} and \mathcal{Y}

To establish shadowing, we perform long-time simulations ($t = 30000\tau$) in MFU A within each of the two chaotic sets and focus on the final segment, $[29000\tau, 30000\tau]$, where transient effects have long decayed. Both chaotic sets exhibit persistent flow reversals between two nonzero mean flow states, as evidenced by their reduced phase space projections and the time series of representative trajectories over this interval. We analyze shadowing events involving a dominating set of 75 ECSs in MFU A. Within this set, we identify four symmetry-based families: 40 ECSs with no additional translation symmetry (T1), 32 ECSs invariant under $\tau_x(L_A/2)$ (T2), one ECS invariant under $\tau_x(L_A/3)$ (T3), and two ECSs invariant under $\tau_x(L_A/4)$ (T4). Each family includes the corresponding symmetry-related counterparts, and we investigate how these families contribute to organizing the dynamics within the chaotic attractors.

For the plots in this section, we color the ECS based on the spatial average of the streamwise velocity $\langle u \rangle$ as follows:

- ECSs confined to $\langle u \rangle > 0$ (red),
- ECSs confined to $\langle u \rangle < 0$ (blue),
- ECSs crossing the subspace $\langle u \rangle = 0$ (green).

To establish shadowing and identify shadowed ECSs, we follow a two step approach [72]. In the first step, for the final 1000τ window within these attractors, we analyze the distances between a typical turbulent trajectory and every ECS (including translation-symmetry-related copies) using a continuous-symmetry-reduced distance [27],

$$d(X_1(t), X_E) = \min_{\substack{0 \leq \ell < L \\ 0 \leq s \leq T}} \|\tau_x(\ell)X_1(t) - X_E(s)\|_2 \quad (11)$$

where $X_1(t)$ is the turbulent trajectory and $X_E(t)$ is the trajectory of the corresponding ECS. At each time step, we identify the ECS with the minimum distance to the turbulent trajectory. The turbulent trajectory should exhibit dynamics similar to those of the ECS during the shadowing event [31, 73]. In the second step, we confirm shadowing by comparing the dynamical evolutions with the trajectory for the ECSs selected as closest to the trajectory, as we discuss next.

	Length	\mathcal{X}	\mathcal{Y}	\mathcal{Z}
MFU A	$L_A = \tilde{L}/3$	Chaotic saddle $\tau_x(L_A/2)$ symmetric	Chaotic attractor No symmetry	Quasiperiodic saddle $\tau_x(L_A/4)$ symmetric
MFU B	$L_B = \tilde{L}/6$	Chaotic attractor No symmetry	Doesn't exist –	Quasiperiodic saddle $\tau_x(L_B/2)$ symmetric

Table I: Properties of the three invariant sets in the two MFUs. For MFU B, the entries refer to the corresponding sets truncated to the reduced domain.

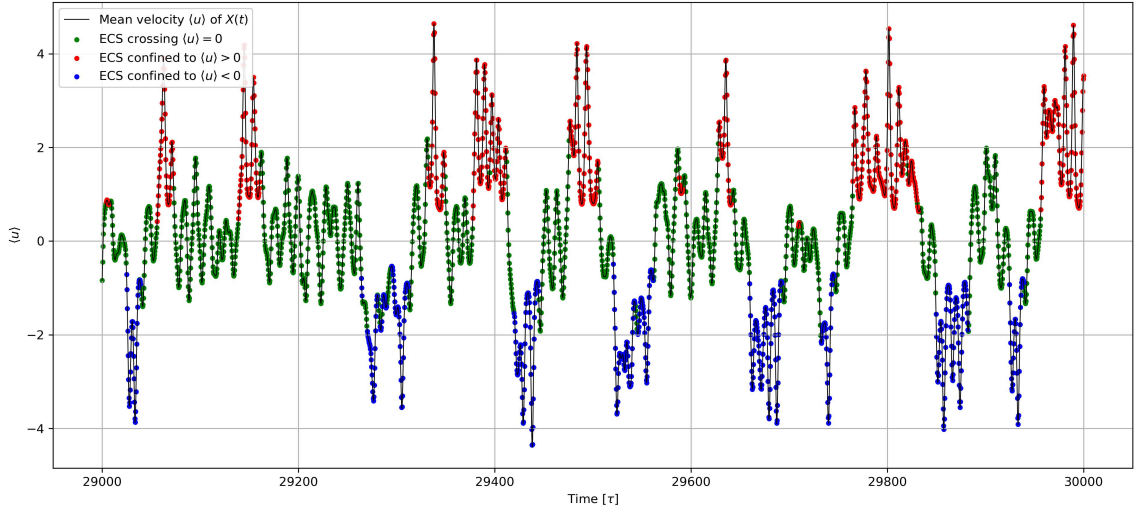
B. Chaotic Set \mathcal{X}

1. Dominant ECSs Within \mathcal{X}

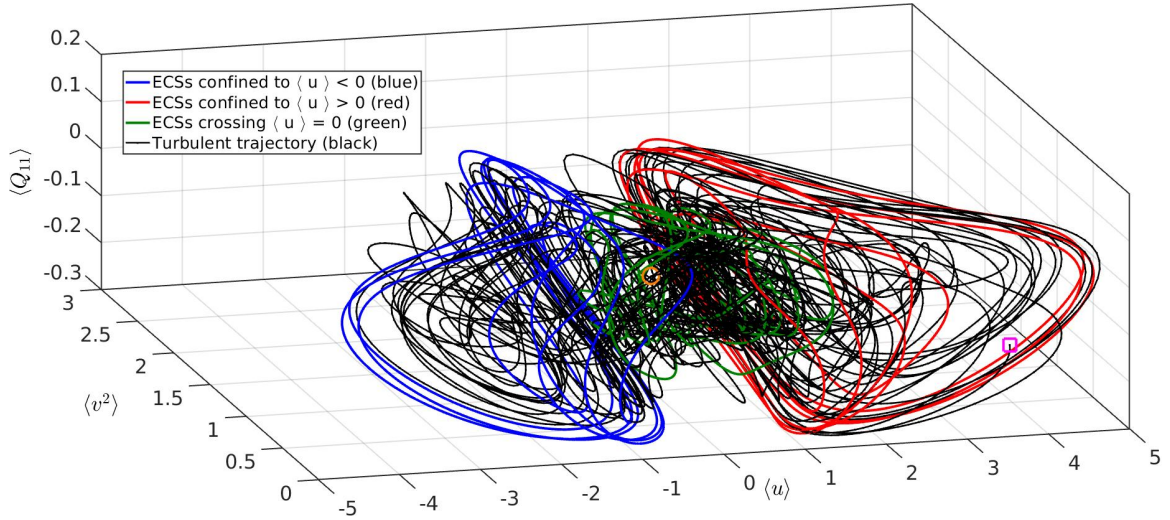
We consider a typical trajectory $X(t)$ lying in \mathcal{X} in MFU A over the interval $[29000\tau, 30000\tau]$. This segment of the trajectory exhibits eleven flow reversals. The mean streamwise velocity $\langle u \rangle$ fluctuates around zero, with extended excursions near $\langle u \rangle = -2$ (net negative flow) and $\langle u \rangle = 2$ (net positive flow). To investigate the underlying structure, we record the closest ECS to the trajectory every 0.4τ , yielding 2501 comparison points. These ECSs are color-coded as discussed above. As shown in Fig. 21, when the trajectory transitions between red and blue regions, it typically passes near a green ECS.

Across the 2,501 points, 40 of the 75 ECSs (along with their symmetry copies) appear as the closest state at least once. To isolate the most dynamically significant structures, we focus on the ten most frequently encountered ECSs. Together, these ten ECSs account for approximately 62% of all occurrences (see Table VI in Appendix). As anticipated, each of these ten ECSs are invariant under $\tau_x(L_A/2)$ symmetry.

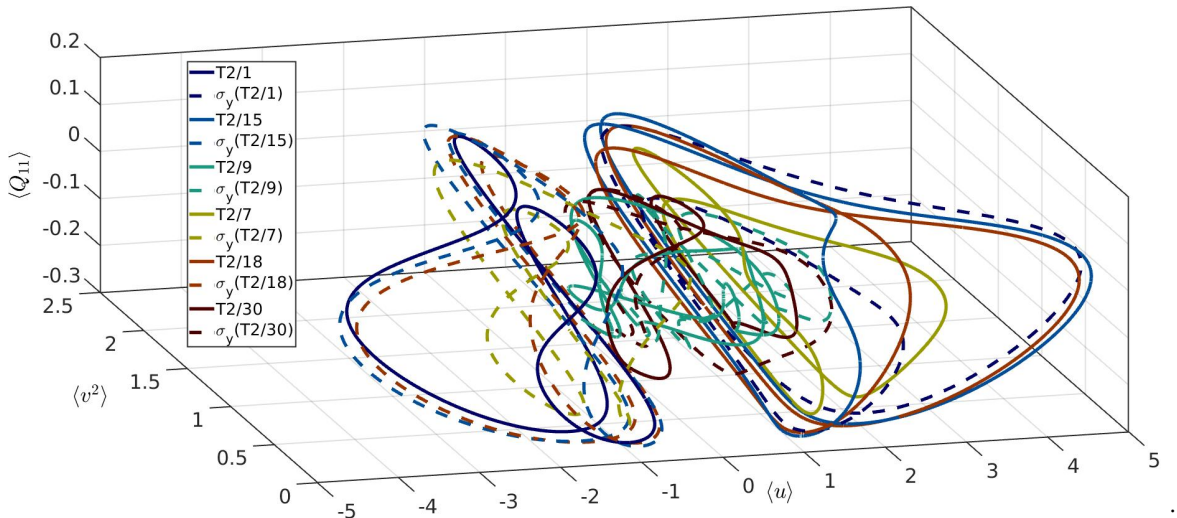
These ten ECSs serve as a reduced representation that captures the essential skeleton of the attractor \mathcal{X} 's dynamics. Six of these ('Group 2', shown in green) are natural candidates for mediating transitions between the red and blue regions, i.e., for enabling reversals. Figure 22 shows the distance plot between the trajectory and these ECSs, highlighting the paths of reversals. The remaining four ECSs ('Group 1', shown in red/blue), along with those from the green category, are closely approximated by the trajectory. For example, in the interval $[29000\tau, 29200\tau]$, during the first reversal of the series (see also Fig. 21a), the distance plot shows that the trajectory first approaches the blue ECS group, with the mean velocity oscillating around $\langle u \rangle \approx -2$. It then nears some ECSs of the green group, where $\langle u \rangle \approx 0$, before finally transitioning to a state where the mean velocity oscillates around $\langle u \rangle \approx 2$ and closely follows the red ECS group.



(a) Time series of $\langle u \rangle$ along the turbulent trajectory $X(t)$ over the interval $29000\tau \leq t \leq 30000\tau$. Various shadowing events are also marked, colored by the region occupied by the corresponding shadowed ECS. The encounters with ECSs that lie completely in the half-space ($\langle u \rangle > 0$) are in red, with ECSs that lie completely in the half-space ($\langle u \rangle < 0$) are in blue, and with ECSs that lie on both sides of the hyperplane ($\langle u \rangle = 0$) are shown in green.



(b) Reduced phase space projection showing the segment turbulent trajectory $X(t)$ in the interval $29000\tau \leq t \leq 30000\tau$ (black) and the six main ECSs (and their symmetry copies). The color scheme for the ECSs is the same as in (a). The orange circle indicates the beginning of the segment ($t = 29000\tau$) and the magenta square indicates the end of the segment ($t = 30000\tau$).



(c) Reduced phase space portrait showing the six main ECSs (and their symmetry copies) shadowed by the turbulent trajectory, along with their symmetry-related copies under σ_y .

Figure 21: Flow reversals and the relationship between the turbulent trajectory and the shadowed ECSs.

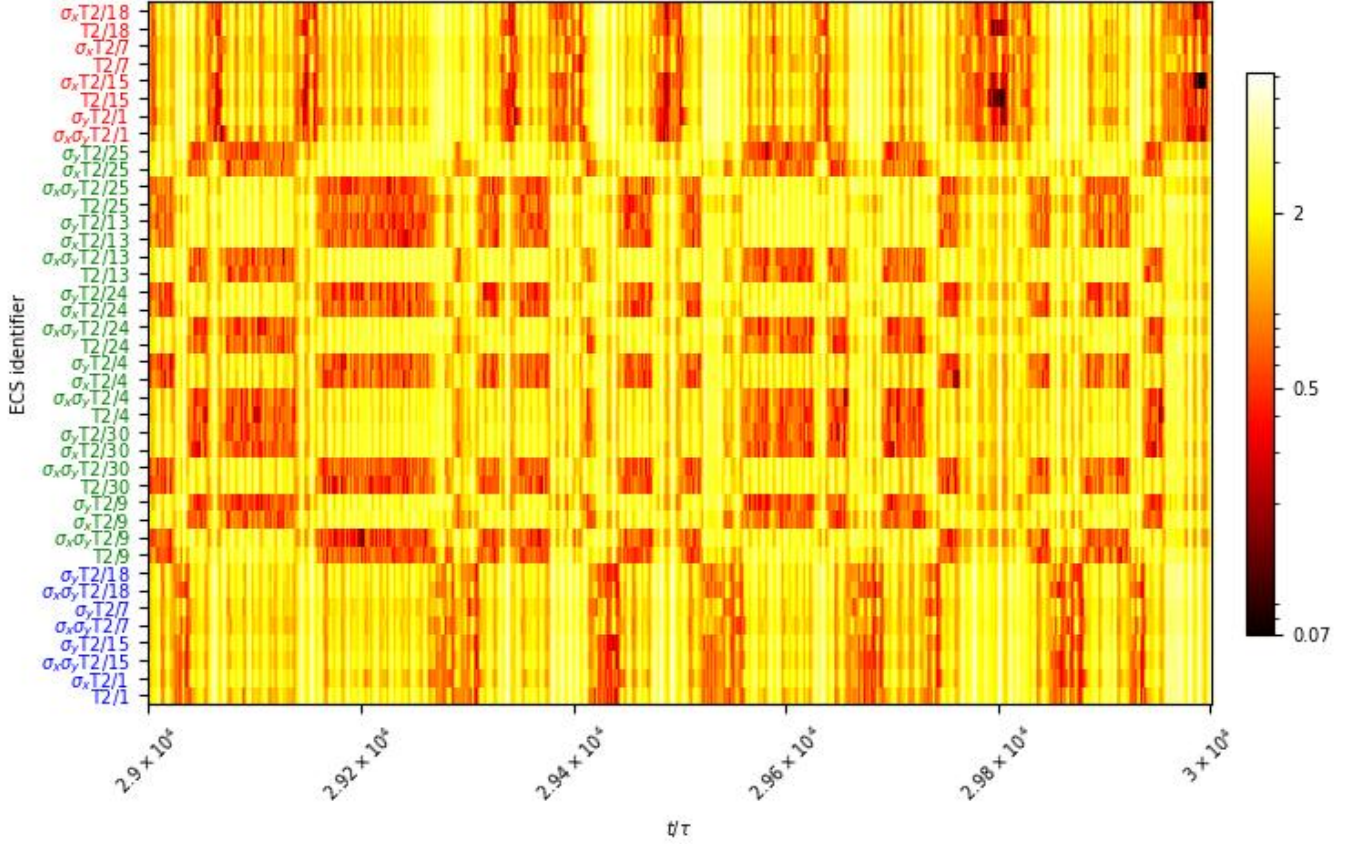


Figure 22: Symmetry-reduced distance plot showing the closest encounters between the chaotic trajectory $X(t)$ and the ten most relevant ECSs and their symmetry copies. The ECS list on the left follows the same color scheme as in Fig. 21(a). The plot shows a clear pattern of repeated transitions (i.e., reversals) between the Group 1 ‘left flowing’ (blue) and ‘right flowing’ (red) ECSs, via the Group 2 intermediate (green) ECSs.

2. Shadowing in \mathcal{X}

Among the above chosen subset of ECSs, we identify the closest ECS at each time step within the interval $[29000\tau, 30000\tau]$, and assess whether these close encounters represent genuine shadowing events. To make this determination, we compare the dynamics of the trajectory with those of the ECSs. Specifically, we utilize the time parameter s associated with each ECS, along with the streamwise translation ℓ , which is applied to obtain the closest translated version of the ECS as defined in Equation 11. A shadowing event is characterized by synchronized evolution between the ECS and the turbulent trajectory. Thus, during a shadowing event, we expect $\frac{ds}{dt} \approx 1$ and $\frac{d\ell}{dt} \approx 0$, indicating that the ECS evolves at nearly the same rate as the trajectory and requires minimal translation to remain aligned with the turbulent trajectory.

Since turbulent trajectories inevitably depart from the ECS along its unstable manifold, we adopt a relaxed criterion to identify approximate shadowing. Specifically, the criterion is considered satisfied when

$$0.5 \leq \frac{ds}{dt} \leq 1.5, \quad (12)$$

as illustrated in Fig. 23. In such cases, we typically observe

$$\frac{d\ell}{dt} < 1, \quad (13)$$

which corresponds to a shift of less than 4% of the channel length. Time derivatives are computed using central differences for interior points and forward/backward differences at endpoints.

For relative periodic orbit ECSs, we additionally account for the discrete jumps in s and ℓ at the orbit period T :

$$\tau_x(\ell_0)X_E(s = T) = X_E(s = 0), \quad \text{so that} \quad s \rightarrow s + T, \quad \ell \rightarrow \ell + \ell_0, \quad (14)$$

which preserves continuity in the symmetry-reduced representation of the RPO and allows consistent computation of the derivatives.

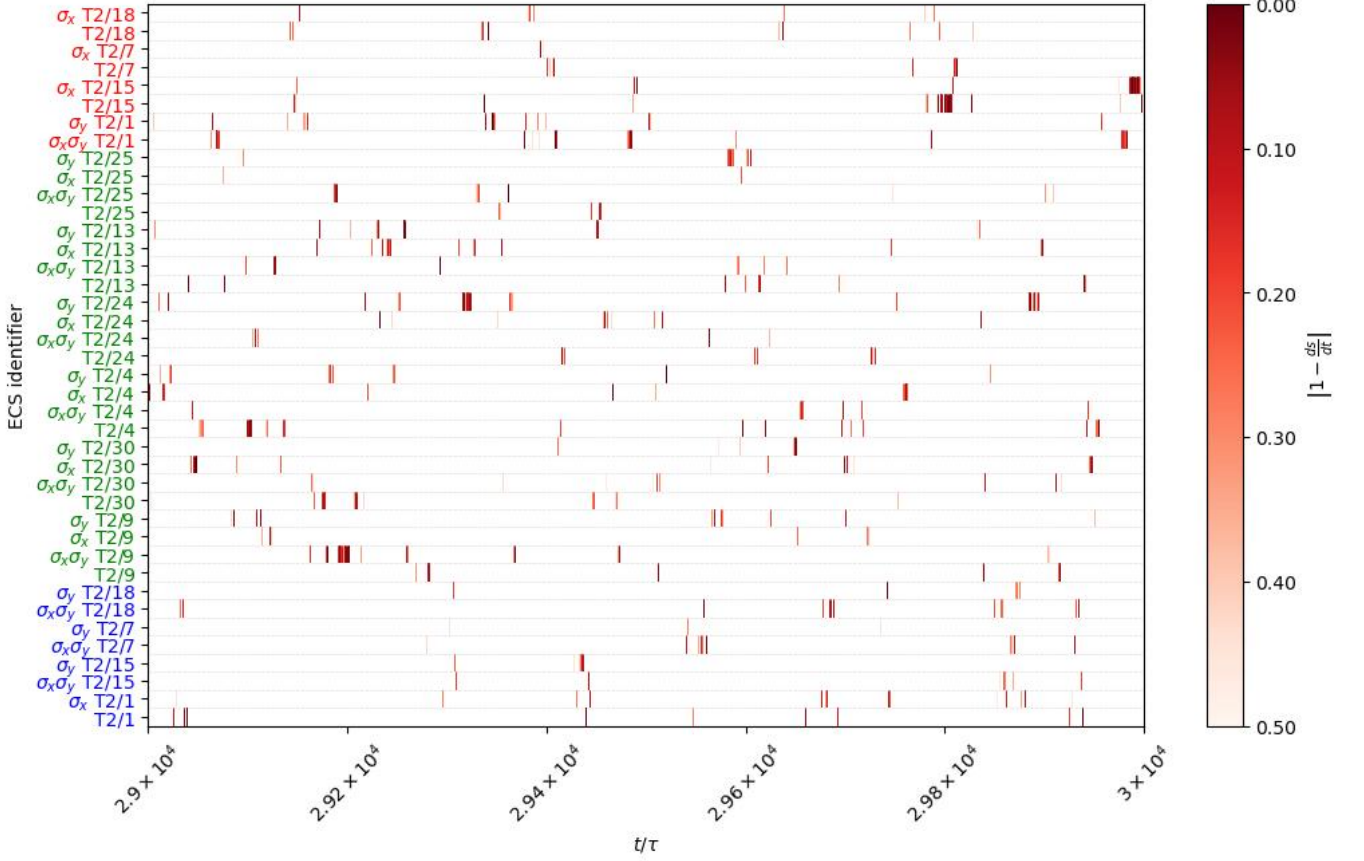


Figure 23: The dynamic shadowing criterion evaluated along the trajectory $X(t)$ relative to the closest ECS $X_E(s)$ at discrete times (with $\delta t = 0.4\tau$) within the interval $[29000\tau, 30000\tau]$. The plot marks instances where the dynamical similarity measure $\frac{ds}{dt}$ lies in the interval $[0.5, 1.5]$, thereby satisfying the criterion. The closer its value is to 1, the stronger the shadowing event.

Shadowing is typically most evident when the distance between the turbulent trajectory and an ECS remains within a small range (typically between 0.07 and 0.3). In the interval $[29099.2\tau, 29104.4\tau]$ (see Fig. 24(a)), the ECS closest to $X(t)$ is T2/4, with an average distance $\langle d \rangle \approx 0.247$ and average rates $\langle |\frac{ds}{dt}| \rangle \approx 1.055$ and $\langle |\frac{d\ell}{dt}| \rangle \approx 0.101$. During this interval, the trajectory reaches the ECS within a minimum distance of $d \approx 0.2$ at $t = 29102\tau$, where $\frac{ds}{dt} \approx 1$ and $\frac{d\ell}{dt} \approx -0.005$, which are the optimal values of these indicators within this interval. Taken together, the consistently small distance, near-unity $\frac{ds}{dt}$, and small $\frac{d\ell}{dt}$ throughout this interval provide strong confirmation of a shadowing event.

Another clear shadowing event occurs in the interval $[29799.2\tau, 29806.8\tau]$ (see Fig. 24(b)). In this case, the closest ECS is T2/15, with average distance and rates $\langle d \rangle \approx 0.126$, $\langle |\frac{ds}{dt}| \rangle \approx 0.989$, and $\langle |\frac{d\ell}{dt}| \rangle \approx 0.183$. At $t = 29805.6\tau$, the

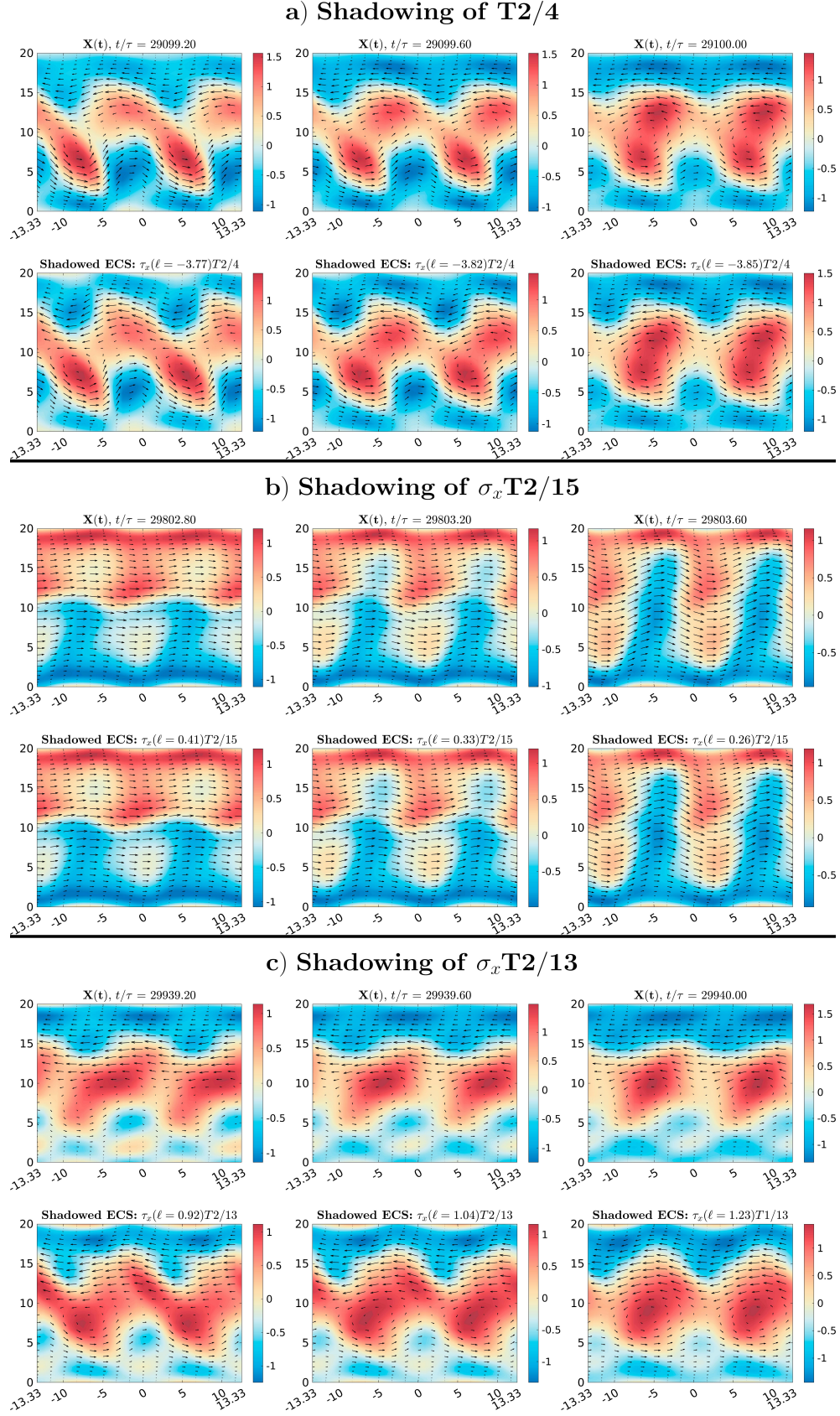


Figure 24: Three snapshots for three different confirmed shadowing events of trajectory $X(t)$. The first row of each event shows sequential snapshots of the turbulent trajectory, while the second row shows sequential snapshots (at the same times) of the shadowed ECS. Notice the translation l is almost constant during each event, which implies that the *same* translated copy an ECS is being shadowed throughout the time interval.

trajectory has $d \approx 0.105$, $\frac{ds}{dt} \approx 1.025$, and $\frac{d\ell}{dt} \approx 0.017$.

When the shadowing criteria are satisfied at larger distances, the resemblance to the ECS is generally weaker. For example, around $t = 29939.6\tau$ (see Fig. 24c), when the turbulent trajectory is in the red region, it does not approach the ECS T2/13 closer than 0.453, yet the temporal evolution remains similar, with $\frac{ds}{dt} \approx 0.813$ and $\frac{d\ell}{dt} \approx 0.391$. Although the resemblance to the ECS is not as strong as in cases with smaller distances, these example suggest that, even at relatively large distances, traces of shadowing can still be detected. This could indicate that the trajectory is closely shadowing another, unconsidered but dynamically related ECS associated with the considered one, or possibly shadowing an invariant manifold instead. Therefore, the analysis of shadowing reveals different nuances that must be taken into account due to the complexity of the phase space geometry.

Observable reconstruction: Additional indirect evidence for shadowing comes from reconstruction of observables along a turbulent trajectory using ECS data. Motivated by periodic orbit theory [59], several recent works [74–76] have proposed approximating inertial turbulent statistics using a collection of invariant solutions, such as unstable periodic and relative periodic orbits. Adopting this perspective, we approximate a physical observable \mathcal{O} in the active nematic system along a turbulent trajectory $X(t)$ by a weighted superposition of ECS contributions,

$$\mathcal{O}(X(t)) \approx \sum_i w_i(t) \mathcal{O}(X_{E_i}(s_i(t))),$$

where $X_{E_i}(s)$ denotes the state along the i -th ECS, $s_i(t)$ is the phase that minimizes the distance to $X(t)$ at time t , and $w_i(t)$ represents the instantaneous weight assigned to that ECS. As a minimal realization, we define the weights using a nearest-ECS criterion: at each time t , the ECS closest (in phase space) to the turbulent state is assigned unit weight, while all others are set to zero. We use three spatially averaged observables: the kinetic energy, enstrophy, and Frank elastic energy. These quantities have been previously used to characterize scaling behavior and statistical properties of active turbulent flows [21, 77]. We define them as follows:

$$E_k = \frac{1}{2A} \int_A (U^2 + V^2) dx dy, \quad (15)$$

$$\mathcal{E} = \frac{1}{2A} \int_A (\partial_y U - \partial_x V)^2 dx dy, \quad (16)$$

$$E_{\text{Frank}} = \frac{1}{2A} \int_A (|\nabla Q_{AA}|^2 + |\nabla Q_{AB}|^2) dx dy, \quad (17)$$

where A is the channel area.

Our approximation captures the trends of all three observables remarkably well, as illustrated by the 8τ moving average time series in Fig. 25. The kinetic energy is reproduced with particularly high fidelity: the correlation between the turbulent signal and its ECS-based approximation is 0.991, and their time averages are 4.946 and 4.746, respectively, corresponding to a relative error of about 4.1%.

Although enstrophy and Frank elastic energy are harder to reconstruct because they depend on spatial derivatives of the velocity field and nematic director field, the time series in Fig. 25 nevertheless reproduces their overall trends reasonably well. Local agreement improves markedly during intervals of stronger shadowing; for instance, around $t = 29100\tau$ and $t = 29800\tau$. In general, however, the ECS-based approximation tends to underestimate both enstrophy and Frank energy.

Quantitatively, enstrophy exhibits a correlation of 0.848 between the turbulent trajectory and its ECS approximation, with temporal averages $\langle \mathcal{E} \rangle = 0.436$ and 0.400, corresponding to a relative error of 8.3%. The Frank energy shows a correlation of 0.656, with temporal averages $\langle E_{\text{Frank}} \rangle = 0.02896$ and 0.0278, yielding a relative error of approximately 4.0%. These results indicate that even observables sensitive to finer spatial structures are well captured, providing further evidence that ECSs form the backbone of active turbulence in the minimal flow unit.

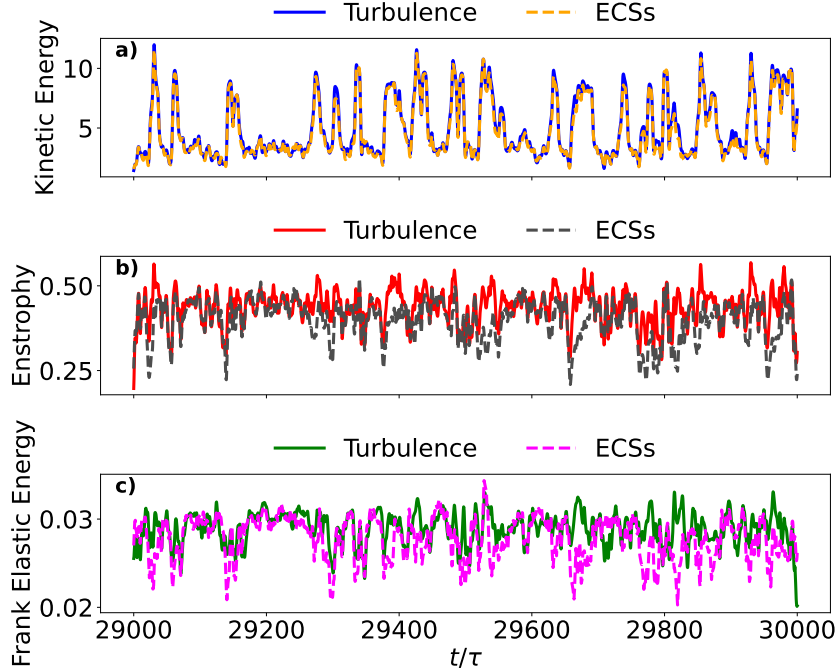


Figure 25: Moving averages (with window 8τ) of each observable, with solid curves showing the turbulent time series and dashed curves the corresponding ECS-based reconstructions.

3. Reversal Mechanisms and Heteroclinic connections

The shadowing events confirmed above hint at mechanisms similar to those discussed for the preturbulent regime in Section IV. Consider, for instance, the first clear reversal event in $X(t)$, occurring within the interval $[29034\tau, 29062.8\tau]$ (see Fig. 21a). The system transitions from a leftward to a rightward unidirectional flow, while passing close to a two-vortex like ECS. Figure 26 illustrates three representative snapshots capturing the key stages of this reversal event, along with their corresponding shadowed ECSs, highlighting how the trajectory temporarily aligns with these coherent structures. Figure 27 complements this view by showing the reduced phase space representation of the same event.

To obtain more insight into the reversal dynamics, the network of heteroclinic connections among the ECSs needs to be studied. However, even in the reduced representation involving a set of 40 ECSs (modulo symmetries), the transition pathways between the blue, green, and red regions are too complicated to be explicitly traced. But some aspects of the phase space geometry become clearer when we focus on specific pairs of ECSs.

First, the Group 2 ECSs play a role analogous to that of the ‘intermediary’ DPOs in the preturbulent regime. These ECSs are likely originated from solutions invariant under symmetries conjugate to $\sigma_x\sigma_y$ and $\tau_x(L_A/2)$ in the preturbulent regime. These ECSs in the turbulent regime have slightly broken $\sigma_x\sigma_y$ symmetry, but retain the two-fold $\tau_x(L_A/2)$ translational symmetry. Supporting evidence includes their similarity to PO_{T2a} in the reduced phase space. Second, the Group 1 ECSs play a role analogous to that of HRPOs, and form the structural backbone for generating left- and right-flowing, nearly uniaxial states. Their phase space structures suggests that these ECSs are most likely the result of symmetry-breaking bifurcations of the HRPOs. The Group 1 ECS retain the homoclinic-like structure in phase space, have broken the shift-reflect symmetries of their preturbulent counterparts, but still possess the two-fold $\tau_x(L_A/2)$ translation symmetry.

To move beyond qualitative resemblance, we quantify residual symmetry in the turbulent ECSs by measuring, along each ECS orbit $X_E(t)$, distances to the appropriate symmetry-related images $\tau_x(\ell)\sigma_x X_E(t)$ and $\tau_x(-\ell)\sigma_x\sigma_y\tau_x(\ell)X_E(t)$,

Shadowing in Flow Reversal within $[29034\tau, 29062.8\tau]$

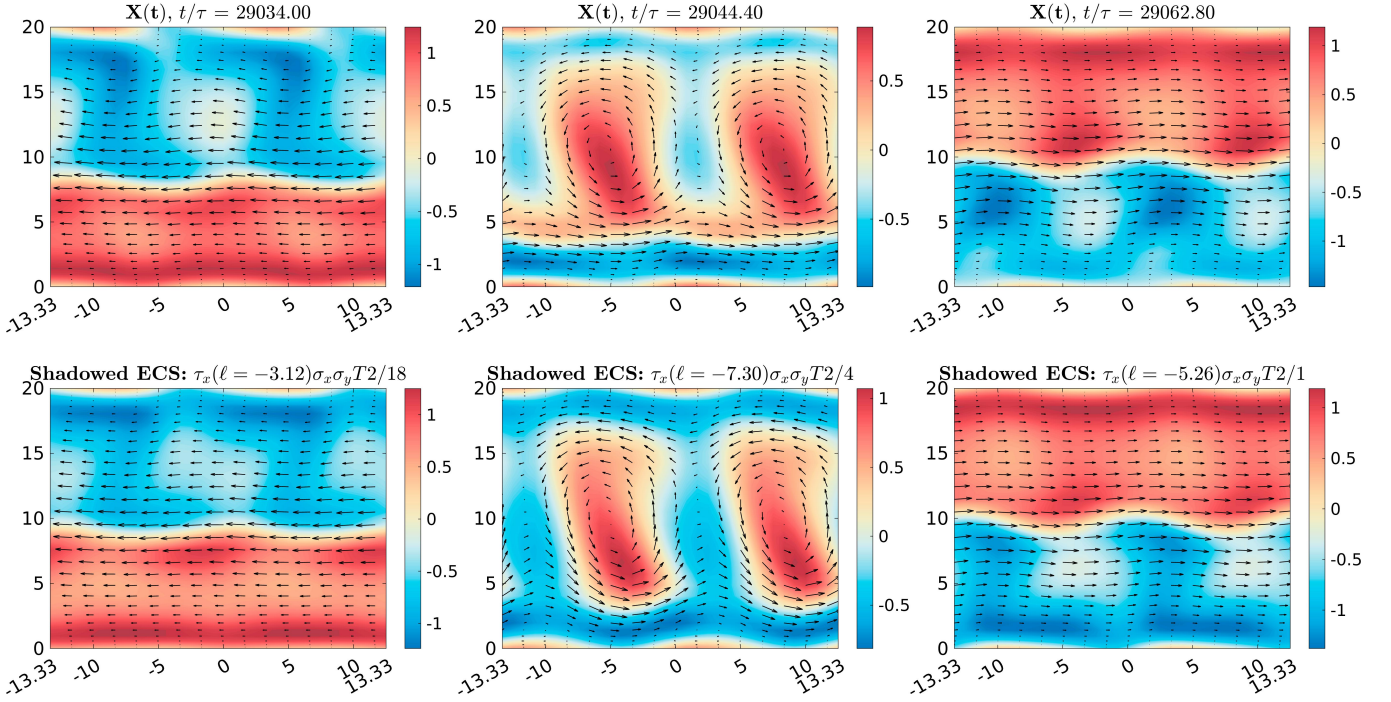


Figure 26: Top row: Velocity field snapshots during the first reversal event for a turbulent trajectory $X(t)$, lying in attractor $\mathcal{X}(t)$, during the interval $[29034\tau, 29062.8\tau]$ resembling the left UNI, two-vortex lattice and right UNI solutions, respectively. Bottom row: Velocity field snapshots of the ECSs shadowed during the reversal shown at the respective times.

for $\ell \in [0, L]$. Since both group 1 and 2 ECSs have two-fold translation symmetry, we work in the half domain MFU B with $L = L_B$. For each snapshot we minimize over l , and use the minimizing shift and the corresponding distance as a remanent symmetry signature, see Fig. 28. We find that Group 1 ECSs come markedly closer to their $l = L/2$ shift-reflect images, consistent with their descent from the unstable UNI eigenspace. Group 2 ECSs instead remain closer to images under the conjugates of $\sigma_x \sigma_y$, supporting their interpretation as descendants of LAN-related branches.

The heteroclinic connections between these groups are the likely mechanisms through which turbulence exhibits flow reversals. Indeed, we observe that heteroclinic connections may exist between pairs of ECSs from different regions that are shadowed sequentially. For example, the red ECS $\sigma_x \sigma_y T2/1$ is shadowed during the interval $[20067.20\tau, 29073.6\tau]$, and immediately afterward, the green ECS $\sigma_y T2/30$ is shadowed during $[29072.80\tau, 29073.6\tau]$. This suggests a heteroclinic connection between these two ECSs. However, within the green region, the turbulent trajectory sequentially (and sometimes simultaneously) shadows several ECSs, including $\sigma_y T2/30$, $\sigma_x T2/25$, $T2/13$, $\sigma_y T2/9$, $\sigma_x T2/30$, $\sigma_x \sigma_y T2/4$, and $\sigma_x \sigma_y T2/13$. Consequently, identifying a heteroclinic connection to a target green ECS is challenging, as shadowing events at the red/green and blue/green boundaries involve multiple ECSs and are not sharply defined. Although we cannot conclusively verify a heteroclinic connection between $\sigma_x \sigma_y T2/1$ and $\sigma_y T2/30$, the turbulent trajectory shadows the unstable manifold of the former ECS and eventually approaches the latter. Throughout the subsequent exploration of the green region, the trajectory continues to follow the unstable manifold, as illustrated by the segment of $X(t)$ and a nearby trajectory in Fig. 29 within the interval $[29064.0\tau, 29094.4\tau]$.

The previous example illustrates how the ECSs and their invariant manifolds shape the dynamics of transitions. To obtain evidence of connections between the green and blue/red ECSs, we perform our computations in MFU B. Recall that in MFU B, \mathcal{X} is the only attractor. Additionally, the ECSs and connections that exist in MFU B and determine the attractor \mathcal{X} dynamics are necessarily those that possess $\tau_x(L_A/2)$ symmetry in MFU A.

In this MFU B based calculation, we focus on the two most relevant Group 1 (blue/red) ECSs and the three most

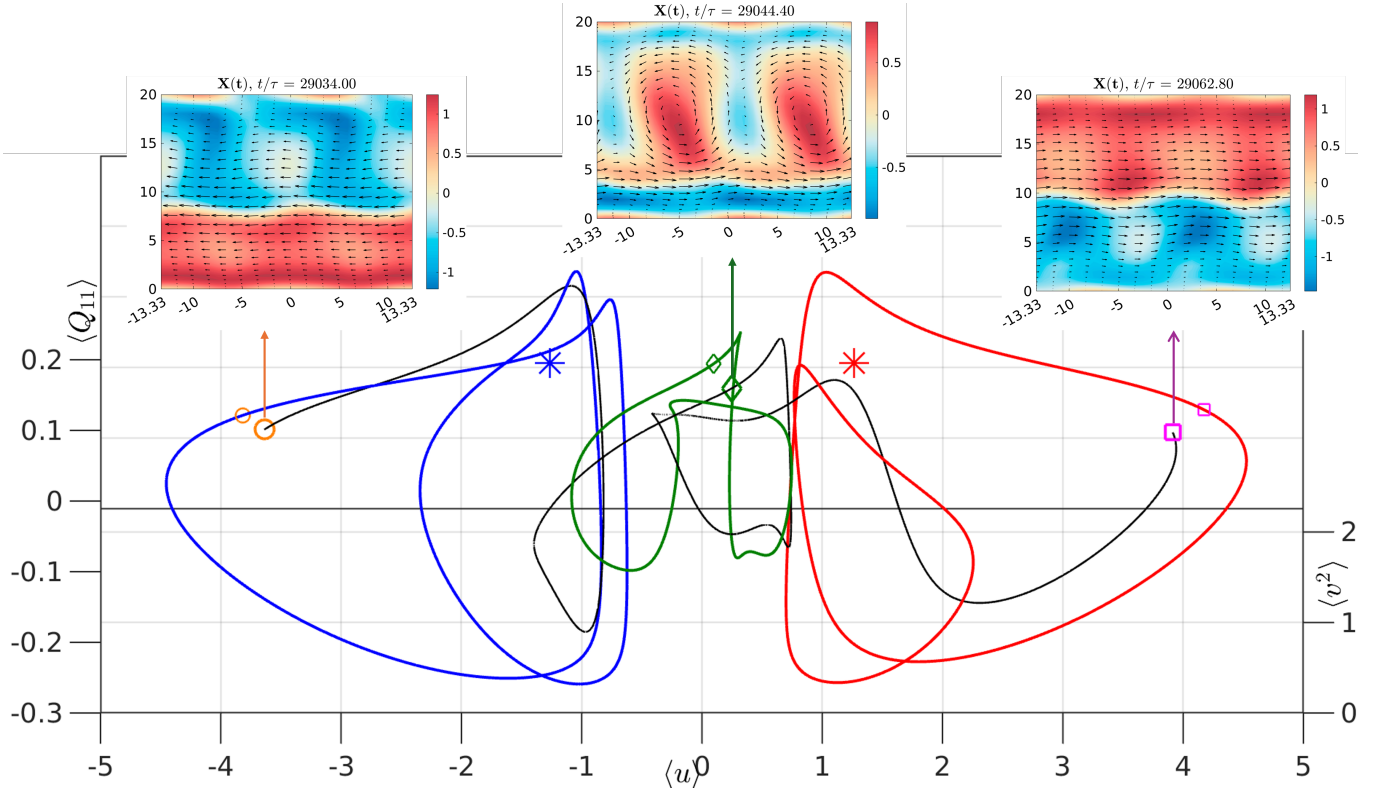


Figure 27: Shadowing and reversals of Fig. 26 in the reduced phase space. A segment of the turbulent trajectory $X(t)$ is shown in black, while the shadowed left-flowing ECS $\sigma_x \sigma_y T2/18$ is shown in blue, the two-vortex ECS $\sigma_x \sigma_y T2/4$ is shown in green, and the right-flowing $\sigma_x \sigma_y T2/1$ is shown in red. The larger circle, rhombus, and square mark the locations of the snapshots (inset) along the turbulent trajectory, while the smaller circle, rhombus, and square indicate the respective locations along the shadowed ECSs. Additionally, the red and blue asterisks show the UNI and σ_y UNI, respectively. An animation of this reversal event is provided in the Supplemental Material.

relevant Group 2 (green) ECSs (and their symmetry counterparts). In this smaller domain, the RPOs T2/1 and T2/15 each have two unstable directions, while the RPOs T2/9, T2/30, and T2/4 have three. We consider the dominant unstable direction to generate a sample of trajectories within each unstable manifold. Several of these trajectories pass nearby and shadow other ECSs, providing evidence of heteroclinic connections. Table II lists few of the pairs of ECSs connected by such trajectories, together with the corresponding minimum distances and shadowing time intervals. The Figs. 30a and 30b highlight two such examples.

Notice that the paths from the green to the red/blue ECSs are clearer than those from the red/blue to the green ECSs. This is related to the fact that the green region is populated by a larger number of unstable ECSs that interact with each other in a more complex manner. For example, the minimum distances between the trajectory on the unstable manifold of T2/30 that shadows T2/15 and the trajectory from T2/9 to T2/1 are on the order of 10^{-3} and 10^{-2} , respectively (see Table II), which is remarkable given the level of simplification used to identify them. In contrast, the trajectories originating from the unstable manifolds of T2/1 and T2/15 do not get sufficiently close to a heteroclinic trajectory to confirm a connection; nevertheless, they clearly illustrate the dynamic paths from

ECS	$\sigma_x \tau_x(\ell)$			$\tau_x(-\ell) \sigma_x \sigma_y \tau_x(\ell)$		
	Min	Avg	Med	Min	Avg	Med
Group 1						
T2/1	0.228	1.280	0.632	1.485	3.847	2.990
T2/15	0.119	0.863	0.443	1.381	3.609	2.919
T2/7	0.712	2.084	1.702	1.505	3.101	2.686
T2/18	0.059	0.711	0.534	1.349	3.728	2.750
Group 2						
T2/9	1.226	3.347	3.366	0.479	1.838	1.699
T2/30	1.333	3.193	2.889	0.347	1.472	1.277
T2/4	0.816	3.002	2.577	0.175	0.992	0.686
T2/24	1.674	3.386	3.486	0.357	1.081	0.973
T2/13	2.098	3.531	3.595	0.230	1.315	1.032
T2/25	1.708	3.329	3.209	0.476	2.000	1.779

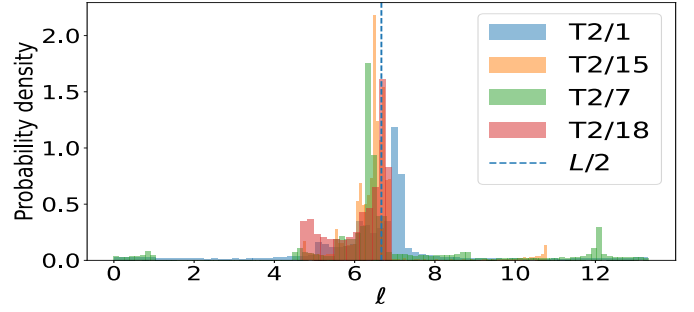


Figure 28: Remanent symmetry analysis based on turbulent ECS orbit data in MFU B. Top: Minimum, mean, and median distances between snapshots along each ECS orbit and their symmetry-related images under the two symmetry types. The results indicate that the dominant approximate (remanent) symmetry is shift-reflect ($\sigma_x \tau_x(L_B/2)$) for Group 1, whereas for Group 2 it is a symmetry conjugate to the reflection $\sigma_x \sigma_y$. Bottom: Distributions of the optimal shifts ℓ for Group 1 ECSs, showing strong peaks near $L_B/2 \approx 6.667$.

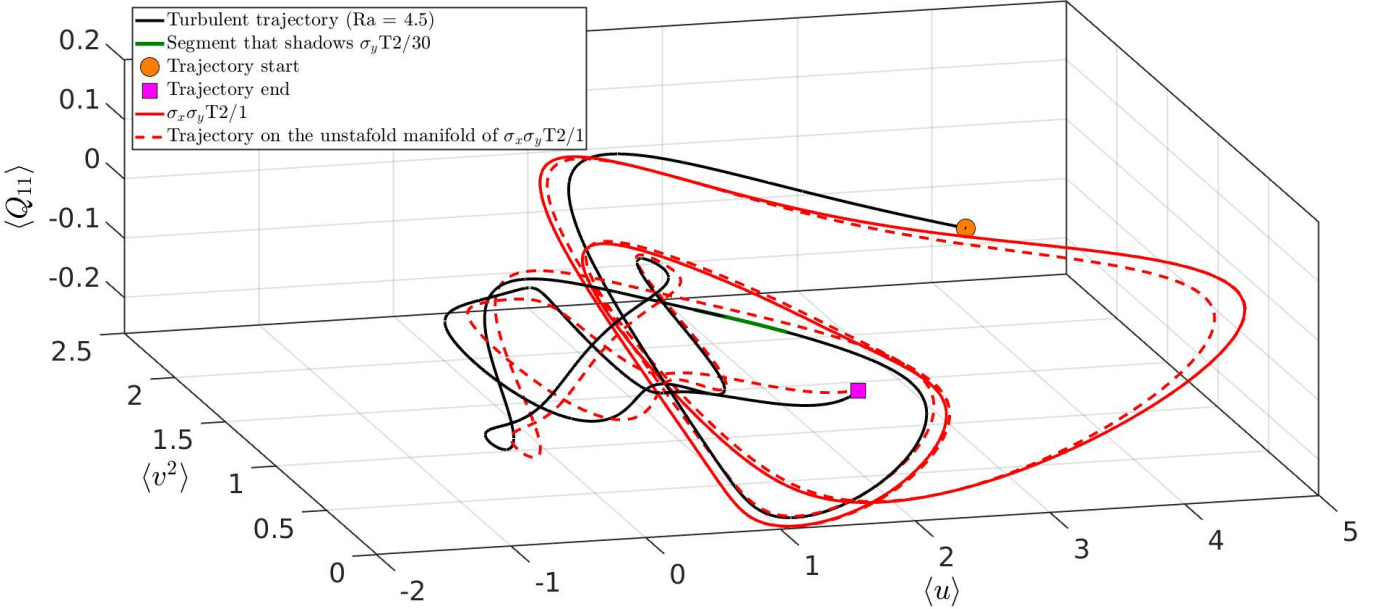


Figure 29: Shadowing of the unstable manifold of a ECS by a turbulent trajectory in \mathcal{X} . The turbulent trajectory (black), shadows a trajectory (red dashed) on the unstable manifold of a ECS, $\sigma_x \sigma_y T2/1$, during $[29064\tau, 29094.4\tau]$. The ECS itself is shown in solid red. The later segment of the turbulent trajectory where it shadows a second ECS, $\sigma_y T2/30$, is shown in green. This latter ECS omitted from the plot for clarity. An animation of this shadowing event is provided in the Supplemental Material.

the red/blue to the green regions by exhibiting a clear shadowing of the latter. These results demonstrate that the unstable manifold of the source ECS eventually shadows the target ECS. This finding confirms that the ECSs and their invariant manifolds constitute the scaffold underlying reversals in the turbulent set \mathcal{X} .

Since \mathcal{X} is the only attractor in MFU B, the above discussion implies that (a) arbitrary trajectories in MFU B ultimately converge to \mathcal{X} , and (b) trajectories on this attractor repeatedly shadow various ECSs and portions of their invariant manifolds.

C. Chaotic Set \mathcal{Y}

1. Dominant ECSs in \mathcal{Y}

We now consider a trajectory $Y(t)$ within the chaotic set \mathcal{Y} over the interval $[29000\tau, 30000\tau]$ in MFU A. Several key differences are evident when compared to a typical trajectory $X(t)$ in \mathcal{X} . First, the oscillations in $Y(t)$ are shorter,

Table II: Examples of trajectories on the unstable manifolds of source ECSs that eventually shadow target ECSs. These trajectories connect the red/blue (left-flowing/right-flowing) group of ECSs to the green (intermediate) group of ECSs. Some of these trajectories appear to approach heteroclinic connections between the source and target pairs.

Source ECS	Target ECS	Type	Min. distance	Shadowing interval
T2/9	$\sigma_x\sigma_y$ T2/1	green \rightarrow red	0.043	10.4 τ
T2/9	σ_y T2/15	green \rightarrow blue	0.053	22.4 τ
T2/30	σ_y T2/1	green \rightarrow red	0.061	12.8 τ
T2/30	$\sigma_x\sigma_y$ T2/15	green \rightarrow blue	0.009	19.6 τ
T2/4	$\sigma_x\sigma_y$ T2/1	green \rightarrow red	0.062	12.4 τ
T2/4	σ_y T2/15	green \rightarrow blue	0.010	22.4 τ
T2/15	σ_y T2/9	red \rightarrow green	0.106	13.2 τ
T2/15	σ_x T2/30	red \rightarrow green	0.15	13.6 τ
T2/15	T2/4	red \rightarrow green	0.115	9.6 τ
T2/1	$\sigma_x\sigma_y$ T2/9	blue \rightarrow green	0.157	14.8 τ
T2/1	T2/30	blue \rightarrow green	0.106	14 τ
T2/1	σ_x T2/4	blue \rightarrow green	0.167	16 τ

and the maximum value of $|\langle u \rangle|$ is about 3, compared to about 4 for $X(t)$. This suggests a less pronounced reversal scenario, with the separation between the blue/red and green regions being less distinct than in $X(t)$. Second, while $Y(t)$ occasionally approximates blue/red ECSs when near $\langle u \rangle \approx 0$, this occurs less frequently than in $X(t)$. Thus, the overlap between the green ECSs and blue/red ECSs is more significant in $Y(t)$, preventing a clear distinction of ECS groups that mediate the reversals. Third, and most importantly, the minimum distances between the trajectory and the ECSs are larger for $Y(t)$ than for $X(t)$.

In general, the shadowing of the ECSs is less pronounced in $Y(t)$, as shown in Table VII in the Appendix for the fifteen most frequent visited ECS groups. For example, the minimum distance from the trajectory to the most frequently visited ECS is 0.308, whereas the minimum distance to the most frequent visited ECSs for $X(t)$ is only 0.119. Notice that we also needed to include more ECSs to cover about 62% of the closest approaches in $Y(t)$ than we did for $X(t)$.

The fact that the set of 75 ECSs is not exhaustive may explain why we do not observe a clearer picture of the dynamical reversals for \mathcal{Y} . Indeed, the distance plot in Fig. 32, for the fifteen most visited ECS groups, shows no clear pattern or contrast between regions, unlike the plot in Fig. 22, which may be attributed to the absence of ECSs that have not yet been computed. The attractor \mathcal{Y} is not constrained by the $\tau_x(L/2)$ symmetry of \mathcal{X} . The additional complexity arises in part from this doubling of the effective MFU length. This is consistent with the principal component analysis (PCA) of the corresponding trajectories (see Table VIII): for $X(t)$, nearly 85% of the variance is captured by just the first two principal components (PCs), and 90% is reached with four; in contrast, $Y(t)$ requires eight components to explain 90% of the variance, indicating that it explores a significantly higher-dimensional region of phase space.

2. Shadowing in \mathcal{Y}

Although the reversal dynamics are not fully captured due to the reduced set of relevant ECSs and the inherent complexity of the chaotic set \mathcal{Y} , our analysis still partly uncovers the underlying deterministic skeleton. Figure 33 shows that shadowing events are less frequent than those of the X -trajectory. Nevertheless, some of these events exhibit dynamics that closely resemble the behavior of the corresponding ECSs, as illustrated in the examples presented in Fig. 34.

The first example occurs in the interval $[29065.2\tau, 29066.4\tau]$, where $Y(t)$ shadows σ_y T1/2, with $\langle d \rangle \approx 0.443$, $\langle |ds/dt| \rangle \approx 0.921$, and $\langle |dl/dt| \rangle \approx 0.392$. In Fig. 34a, we show three consecutive snapshots from this interval, corresponding to the moment when the distance reaches its minimum value $d \approx 0.393$. The second example in

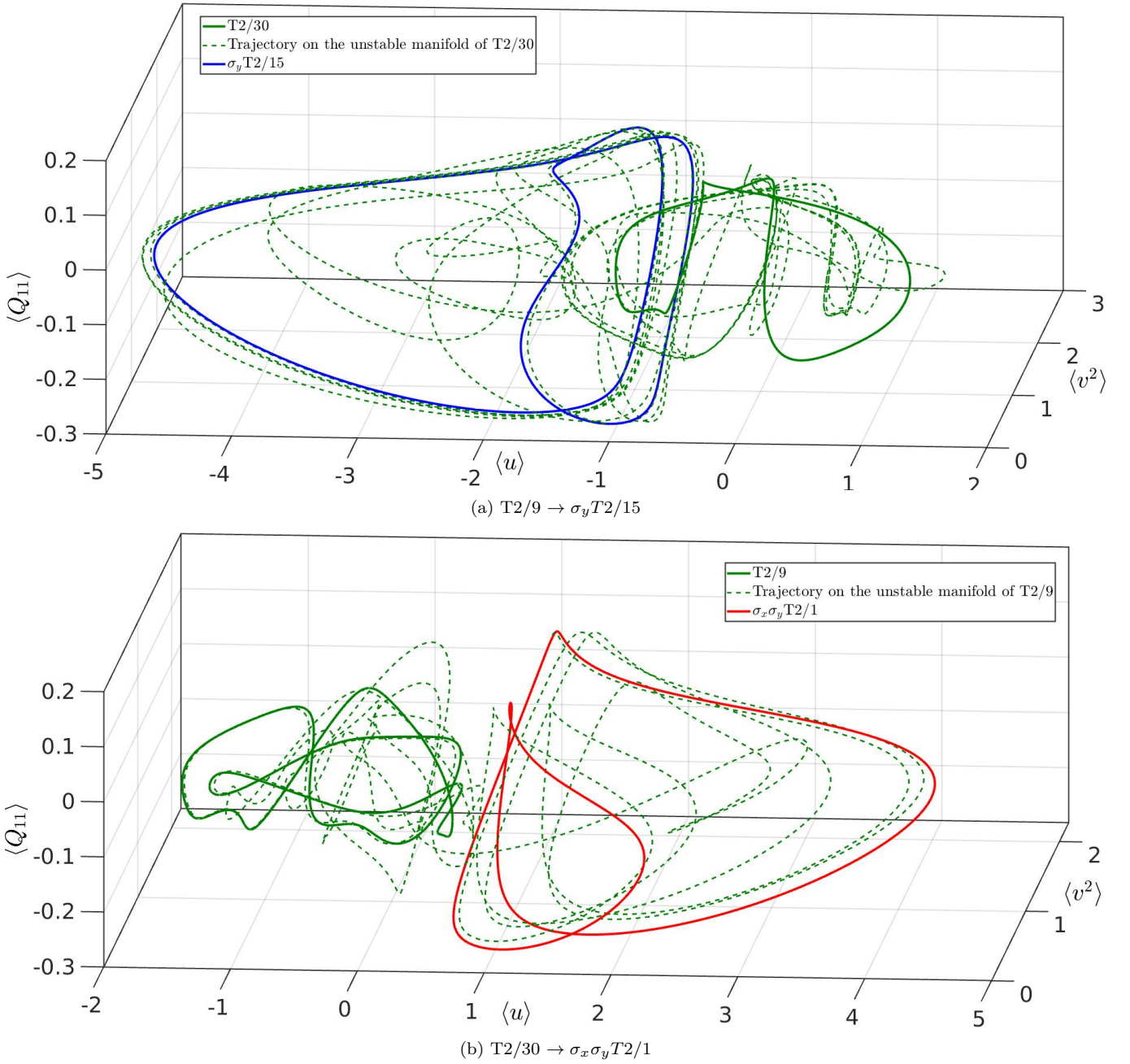


Figure 30: Examples of trajectories on the unstable manifolds of intermediary (green) ECSs $T2/30$ and $T2/9$ that eventually shadow the left-flowing $\sigma_y T2/15$ (blue) and right-flowing $\sigma_x \sigma_y T2/1$ (red) ECSs, respectively. The minimum distance between a trajectory and the target ECS was found to be 0.043. These results provide strong evidence for the existence of the corresponding heteroclinic connections.

Fig. 34 is a shadowing of $\sigma_x T1/3$ within the interval $[29602.8\tau, 29603.6\tau]$. In this case, $\langle d \rangle \approx 0.304$, $\langle |ds/dt| \rangle \approx 1.363$, and $\langle |dl/dt| \rangle \approx 0.724$. Interestingly, although the trajectory approaches this ECS more closely than in the previous example, the dynamics are less synchronized with the ECS. Finally, we discuss a shadowing event in the interval $[29944\tau, 29947.2\tau]$, where $\langle d \rangle \approx 0.365$, $\langle |ds/dt| \rangle \approx 0.927$, and $\langle |dl/dt| \rangle \approx 0.267$. The trajectory approaches the ECS to a minimum distance of $d \approx 0.308$ at $t = 29946.4$, which corresponds to one of the snapshots shown in the figure. Notice, however, that these shadowing confirmations are less pronounced than our findings in the more constrained attractor \mathcal{X} .

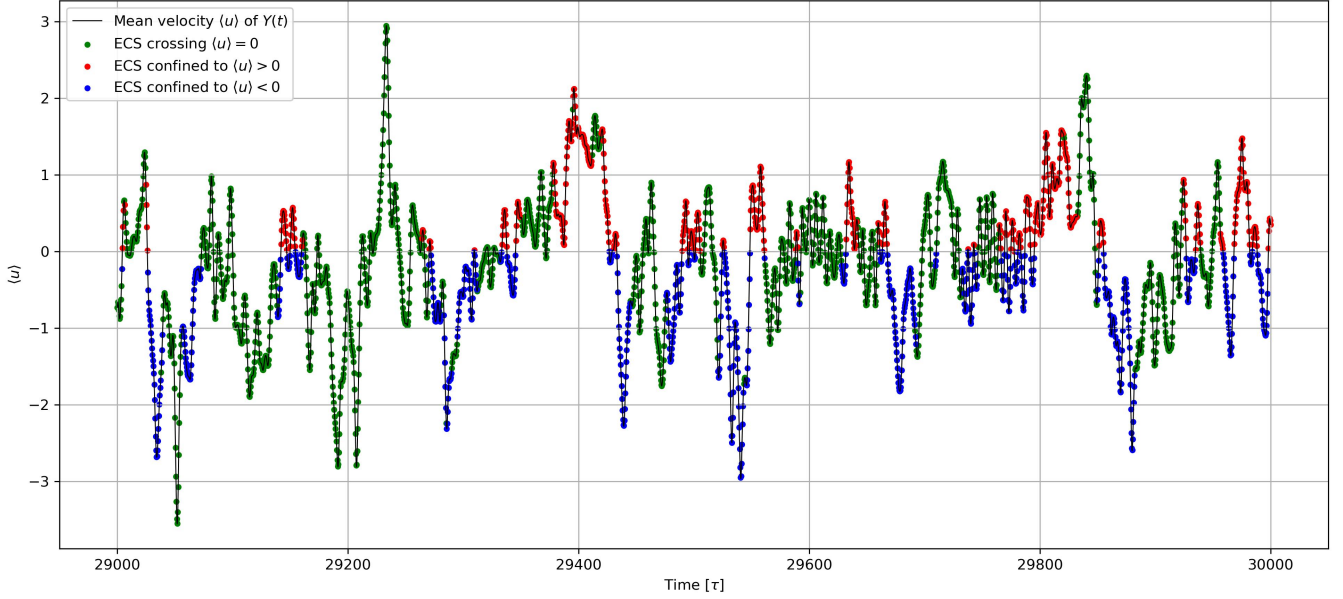


Figure 31: Time series of $\langle u \rangle$ along the turbulent trajectory $Y(t)$. Various shadowing events are also marked, colored by the region occupied by the corresponding shadowed ECS, using the same color scheme as in Fig. 21(a).

The confirmed shadowing events suggest that the turbulence could follow paths that are broadly similar to those observed in the previous trajectory case. Specifically, we expect that the blue and red ECSs shape the nearly uniaxial flow, while the green ECSs mediate the transitions. However, as mentioned, the description with the ECS in hand remains incomplete. Consider, for example, the interval $[29400\tau, 29600\tau]$ (see Fig. 35 for a detailed view and Fig. 31 for the broader time series). Around $t = 29412\tau$, the mean velocity $\langle u \rangle$ of the trajectory $Y(t)$ oscillates around $\langle u \rangle \approx 1.5$, showing an unclear shadowing of $\sigma_y T1/13$ with a distance $d \approx 0.585$. Following this, brief oscillations occur with successive approximations to the red, green, and blue ECSs. During this interval, there is a clear brief shadowing of the green ECS $\sigma_x T1/3$ at $t = 29449.20$ with a minimum distance $d \approx 0.295$. The trajectory eventually reaches the longest and clearest oscillation in the blue region, where at $t = 29537.6$, it satisfies the shadowing criterion for T1/13 with a distance $d \approx 0.787$. These three instants highlight the incomplete nature of our description: the large distances to the hypothetically shadowed ECSs when the trajectory is nearly unidirectional, along with the multiple ill-defined oscillations in between, illustrate the gaps in our current understanding.

Overall, the ECS based description of reversals is less clear here than in the case of $X(t)$. Nevertheless, the shadowing evidence indicates that ECSs and their invariant manifolds may still organize the dynamics within this attractor in a manner similar to what was observed for $X(t)$. A more comprehensive search for additional and potentially more intricate ECSs with longer time periods is therefore needed to resolve the gaps in our current understanding. Resolving these questions will be the subject of future work.

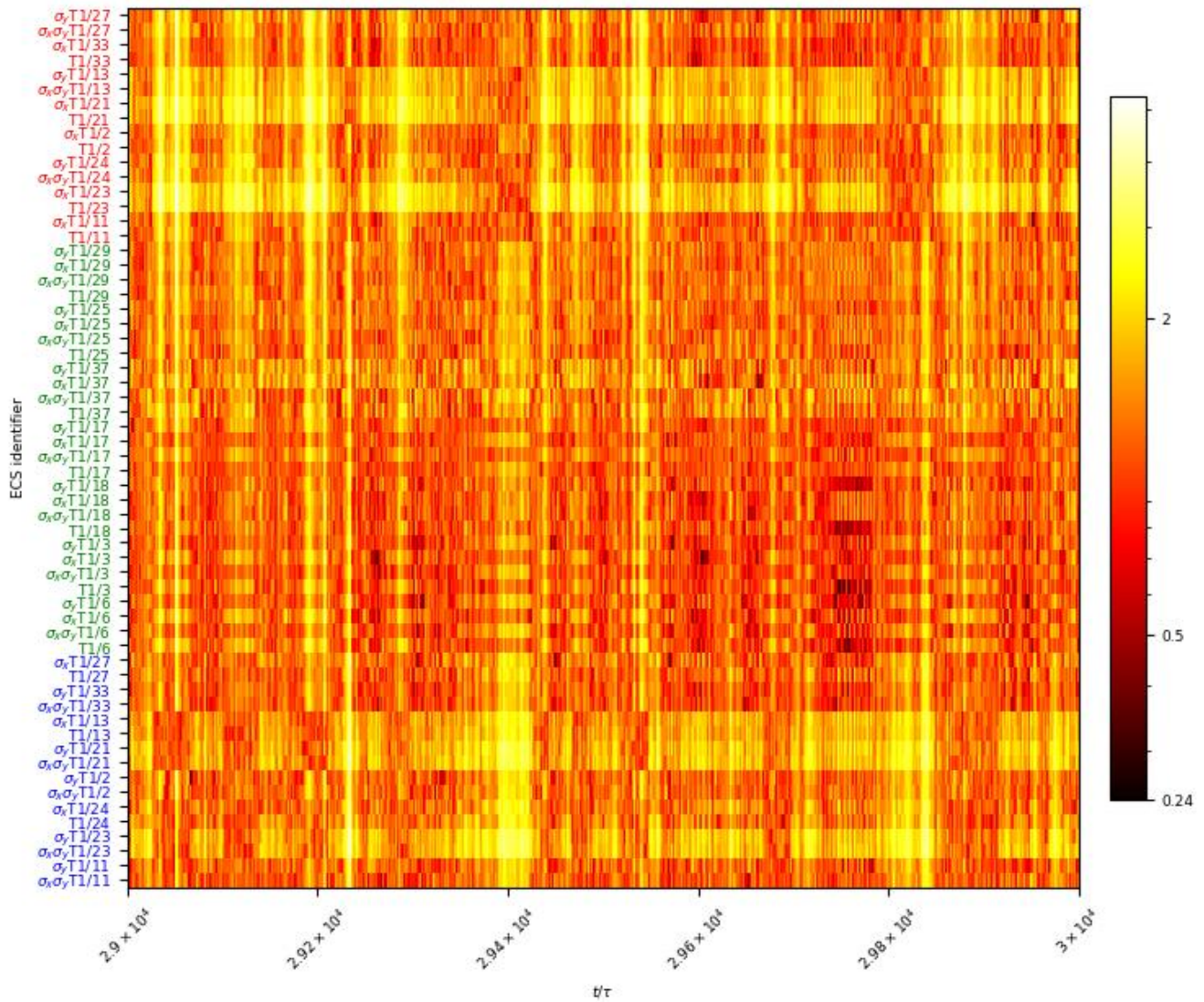


Figure 32: Symmetry-reduced distance plot showing the closest approaches between the turbulent trajectory $Y(t)$ and 15 dynamically relevant ECSs (and their symmetry counterparts). Together, these ECSs account for more than 60% of all shadowing events. In contrast to the trajectory $X(t)$ (see Fig. 22) where the shadowing events were well separated in time, here the shadowing of the green ECSs and the red/blue ECSs appears to occur concurrently. The minimum distance attained is 0.24, roughly three times larger than the smallest distance observed for $X(t)$.

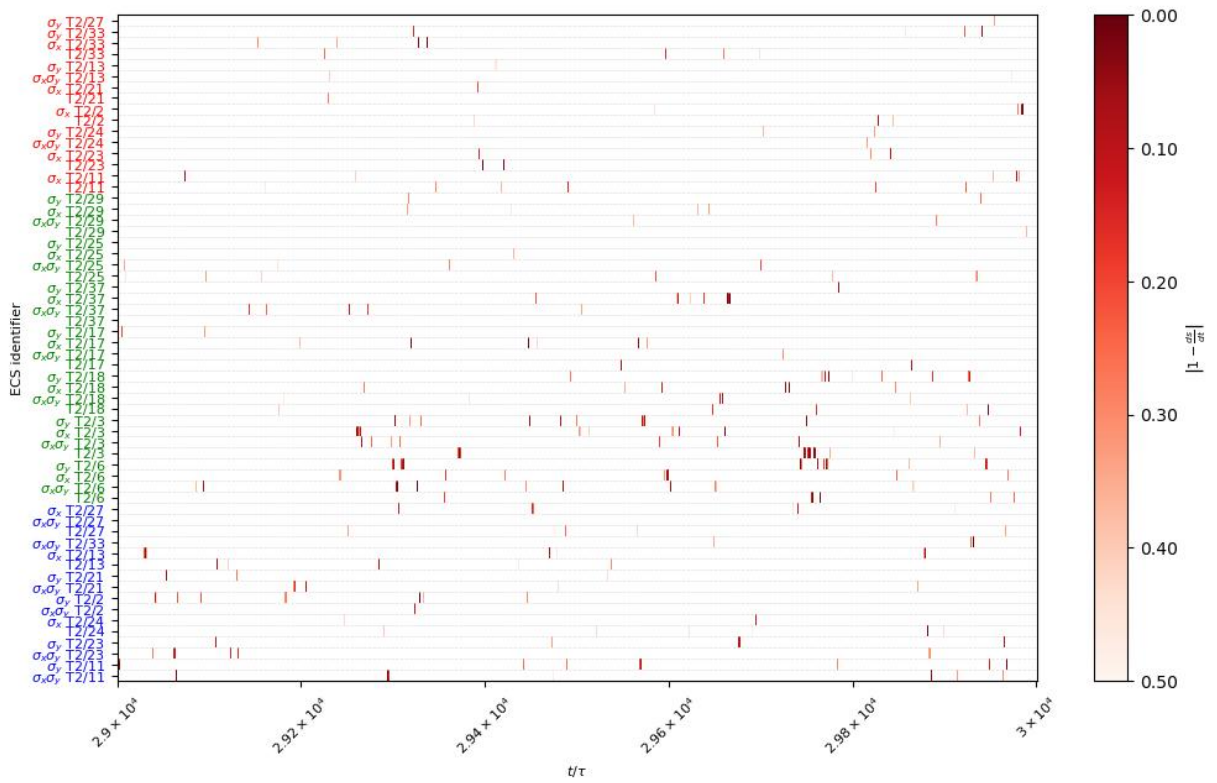


Figure 33: The dynamic shadowing criterion evaluated along the trajectory $Y(t)$ at discrete times (with $\delta t = 0.4\tau$) within the interval $[29000\tau, 30000\tau]$. The plot marks instances where the dynamical similarity measure $\frac{ds}{dt}$ lies in the interval $[0.5, 1.5]$, thereby satisfying the criterion. Although fewer shadowing events are detected than for $X(t)$, their presence points to similar underlying dynamics and motivates the search for additional ECSs to account for the remaining gaps.

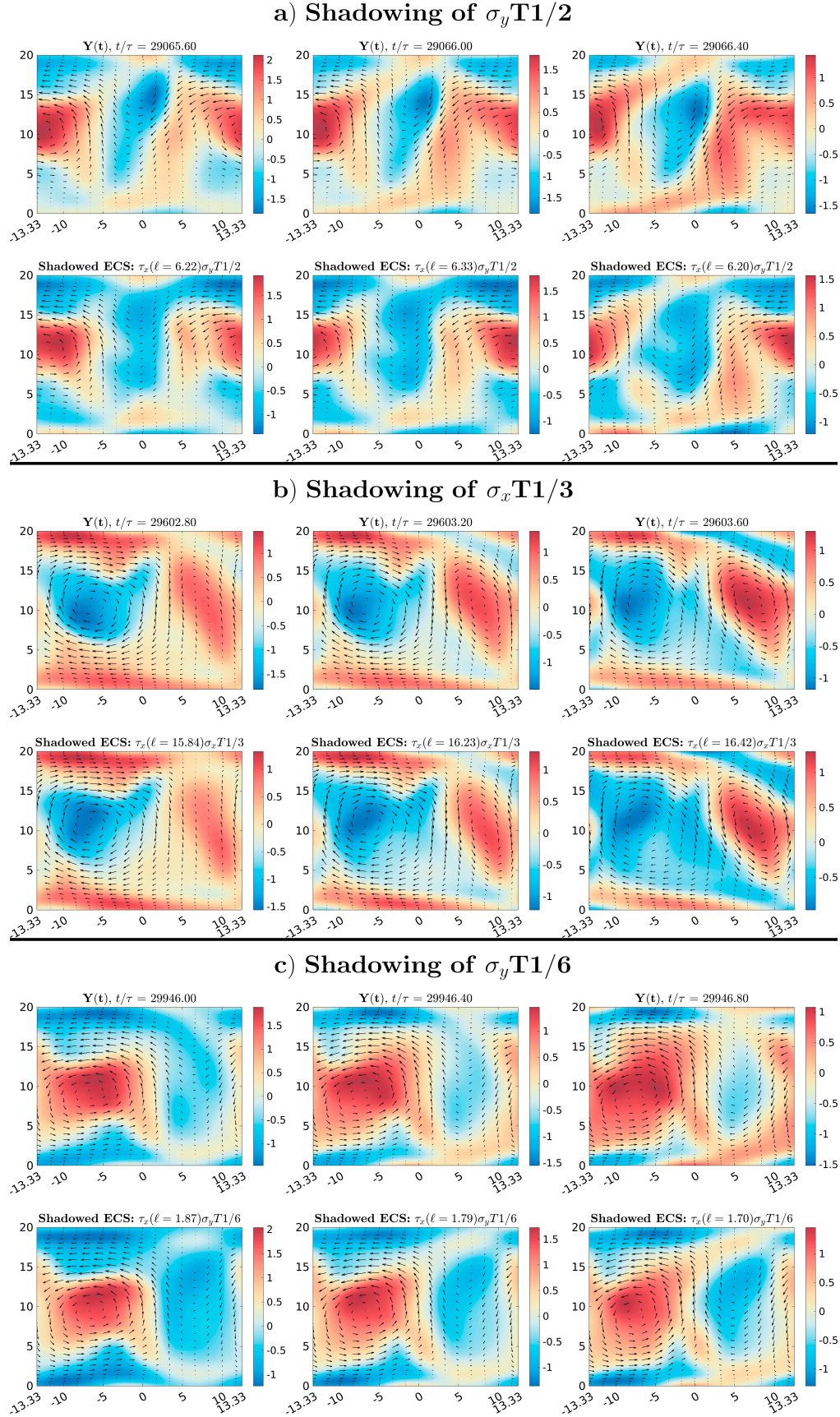


Figure 34: Velocity field snapshots of three confirmed shadowing events for the trajectory $Y(t)$. The first row of every event shows three sequential snapshots (with $\delta t = 0.4\tau$) of the turbulent trajectory. The second row of every event corresponds to sequential snapshots (at the same times) of the shadowed ECS.

Shadowing in Flow Reversal [29412 τ , 29537.6 τ]

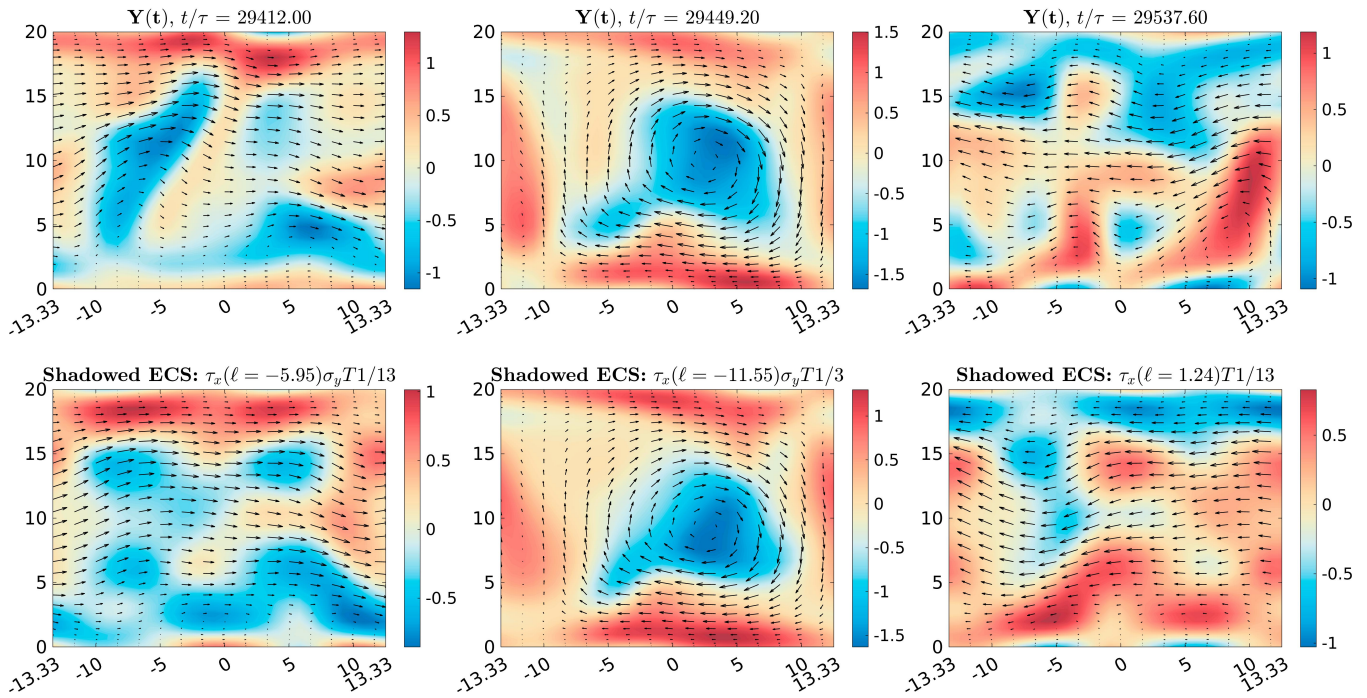


Figure 35: Top row: Velocity field snapshots during the first reversal event for a turbulent trajectory $Y(t)$, evolving in the attractor $\mathcal{Y}(t)$, during the interval $[29412\tau, 29537.6\tau]$. Bottom row: Velocity field snapshots of the ECSs shadowed during this reversal, shown at the corresponding times. The resemblance between the turbulent flow and the shadowed ECS is noticeably weaker in snapshots where the flow is nearly unidirectional

VI. DISCUSSION AND CONCLUSIONS

Taking an infinite-dimensional dynamical systems perspective on active turbulence, we have studied a hydrodynamic model of active nematics in a minimal channel geometry. The dynamics in the smallest domain we consider is complex enough to sustain active turbulence, yet, as we have shown, simple enough that the phase space transport is organized around $\mathcal{O}(10)$ ECSs and the heteroclinic network connecting them.

Through an equivariant bifurcation analysis, we clarified the origin of several key solutions reported in earlier works and uncovered their role in shaping the global dynamics of the preturbulent regime. In this regime, three mechanisms for transient reversals are identified, involving either one of the two y -reflection-related copies of RPOs that are nearly homoclinic to the two uniaxial states, or the symmetric PO that is nearly heteroclinic to the two uniaxial states. Typical reversals involve a heteroclinic connection between one of the above mentioned ECSs (all unstable) and an attractor. Some reversals are mediated by a vortex-dominated PO. The homoclinic-like and heteroclinic-like ECSs possess the shift-reflect symmetry, and some of them additionally have discrete translation symmetries. All vortex-dominated POs have the x - y reflection symmetry, with some again possessing discrete translation symmetries.

In the active turbulent regime in the original domain, we find that a subset of persistent flow reversals involve homoclinic-like RPOs that have slightly broken shift-reflect symmetry, but retain the discrete translation symmetry of their preturbulent counterparts. These reversals are mediated by vortex-dominated ECSs which are RPOs that have broken x - y reflection symmetry yet still inherit the discrete translation symmetries of the preturbulent periodic orbits from which they originate. Building on this, we identify a smaller minimal flow unit corresponding to a *fundamental domain* [78], i.e., the smallest domain in which the lone turbulent attractor (\mathcal{X}) is organized by ECSs that no longer possess any residual spatial symmetries. In this domain, we establish robust shadowing of the dominating ECSs by typical turbulent trajectories via the use of symmetry-reduced distance and dynamical similarity measures.

Although our concrete computations are performed for a Beris–Edwards Q-tensor model, much of the structure we uncover relies only on symmetries that are shared across a broad class of continuum descriptions of active nematics. In particular, the local bifurcation analysis depends primarily on translational and reflection symmetries, and the nematic head–tail symmetry, and not on the precise forms of the equations [33]. The catalog of symmetry types of steady and time-periodic solutions and their bifurcations depends only on the total symmetry group G and the representation on the critical eigenspaces, and therefore should be robust across all modeling choices that are expected to have these same symmetries [32]. We therefore expect the ECS families and reversal pathways identified here to be robust under variations in constitutive parameters and even under modest changes of the modeling framework. Repeating the presented analyses using different models will shift bifurcation points and stability boundaries, but the underlying symmetry-based organization and the existence of low-dimensional ECS skeletons mediating reversals should persist.

While shadowing of coherent structures is clearly observed and quantified in the smallest domain, conclusively establishing the same phenomenon in the original domain proved more challenging, owing to its richer dynamics, the larger dimension of the turbulent attractor, and our inability to compute a more complete set of ECSs. This difficulty is only expected to worsen in longer channels. Future work will focus on closing this gap and clarifying the role of invariant solutions in active nematic turbulence across a wider range of spatial and temporal scales. To do this, we will make use of recent advances in machine learning approaches [79–81] that have successfully employed autoencoders to compute ECSs in challenging inertial turbulent flow settings.

ACKNOWLEDGMENTS

This material is based upon work supported by the U.S. Department of Energy, Office of Science, Office of Basic Energy Sciences under award number DE-SC0022280. This work was completed utilizing the Holland Computing Center of the University of Nebraska, which receives support from the UNL Office of Research and Innovation, and the Nebraska Research Initiative.

APPENDIX

1. Isotropy subgroups of unstable eigenspaces of UNI and LAN

Table III: Isotropy groups of the unstable eigenspaces of UNI in $L = L_A$. All eigenvalues are complex. The R_a column indicates the approximate activity values at which each two-dimensional unstable eigenspace emerges. From $R_a \approx 3.7$ to 4.5, no additional local bifurcations from UNI are observed.

Complex pair	Generators	Group elements	Group structure	R_a
1st	$\{\sigma_x \tau_x(L/2)\}$	$\{e, \sigma_x \tau_x(L/2)\}$	\mathbb{Z}_2	0.71
2nd	$\{\sigma_x \tau_x(L/4)\}$	$\{e, \sigma_x \tau_x(L/4), \tau_x(L/2), \sigma_x \tau_x(3L/4)\}$	\mathbb{Z}_4	0.97
3rd	$\{\sigma_x \tau_x(L/2), \tau_x(L/3)\}$	$\{e, \tau_x(L/3), \tau_x(2L/3), \sigma_x \tau_x(L/6), \sigma_x \tau_x(L/2), \sigma_x \tau_x(5L/6)\}$	D_3	1.79
4th	$\{\sigma_x, \tau_x(L/2)\}$	$\{e, \sigma_x, \tau_x(L/2), \sigma_x \tau_x(L/2)\}$	$D_2 \cong \mathbb{Z}_2 \times \mathbb{Z}_2$	2.05
5th	$\{\sigma_x, \tau_x(L/3)\}$	$\{e, \tau_x(L/3), \tau_x(2L/3), \sigma_x, \sigma_x \tau_x(L/3), \sigma_x \tau_x(2L/3)\}$	$\mathbb{Z}_6 \cong \mathbb{Z}_2 \times \mathbb{Z}_3$	2.5
6th	$\{\sigma_x \tau_x(L/8)\}$	$\{e, \sigma_x \tau_x(L/8), \tau_x(L/4), \sigma_x \tau_x(3L/8), \tau_x(L/2), \sigma_x \tau_x(5L/8), \tau_x(3L/4), \sigma_x \tau_x(7L/8)\}$	\mathbb{Z}_8	3.01
7th	$\{\sigma_x, \tau_x(L/4)\}$	$\{e, \tau_x(L/4), \tau_x(L/2), \tau_x(3L/4), \sigma_x, \sigma_x \tau_x(L/4), \sigma_x \tau_x(L/2), \sigma_x \tau_x(3L/4)\}$	$\mathbb{Z}_2 \times \mathbb{Z}_4$	3.7

Table IV: Isotropy groups of the unstable eigenspaces of LAN in $L = L_A$. Each real eigenvalue has multiplicity two. The R_a column indicates the approximate activity values at which each two-dimensional unstable eigenspace emerges.

Real pair	Generators	Group elements	Group structure	R_a
1st	$\{e\}$	$\{e\}$	Trivial group	0.85
2nd	$\{\tau_x(L/2)\}$	$\{e, \tau_x(L/2)\}$	\mathbb{Z}_2	1.25
3rd	$\{\tau_x(L/3)\}$	$\{e, \tau_x(L/3), \tau_x(2L/3)\}$	\mathbb{Z}_3	2.11
4th	$\{\tau_x(L/2)\}$	$\{e, \tau_x(L/2)\}$	\mathbb{Z}_2	2.51
5th	$\{\tau_x(L/3)\}$	$\{e, \tau_x(L/3), \tau_x(2L/3)\}$	\mathbb{Z}_3	3.10
6th	$\{\tau_x(L/4)\}$	$\{e, \tau_x(L/4), \tau_x(L/2), \tau_x(3L/4)\}$	\mathbb{Z}_4	3.30
7th	$\{\tau_x(L/4)\}$	$\{e, \tau_x(L/4), \tau_x(L/2), \tau_x(3L/4)\}$	\mathbb{Z}_4	4.21
8th	$\{e\}$	$\{e\}$	Trivial group	4.36

2. Symmetry classification: isotropy subgroups of the main ECS solutions

For ECSs in the preturbulent regime, the subscript is of the form Tmx , where the number m labels the originating unstable eigenspace, while the letter x ($=a, b, c, \dots$) distinguishes different RPOs arising from the same eigenpair.

Each ECS in the turbulent regime is denoted Tk/n , where k specifies the discrete translation symmetry $\tau_x(L_A/k)$, and n indexes the different ECSs within that symmetry class.

Table V: Main ECSs and their symmetries. All discrete translation symmetries refer to MFU A, with $L = L_A = \tilde{L}/3$.

Description	Name	Symmetry generator	Comment
Homoclinic-like RPO from 1st unstable pair of UNI	HRPO $_{T1a}$	$\sigma_x \tau_x(L/2)$	Preturbulent regime.
Homoclinic-like RPO from 2nd unstable pair of UNI	HRPO $_{T2a}$	$\sigma_x \tau_x(L/4)$	Preturbulent regime.
Heteroclinic-like PO from 1st unstable pair of UNI	HTPO $_{T1a}$	$\sigma_x \tau_x(L/2)$	Preturbulent regime.
Heteroclinic-like PO from 1st unstable pair of UNI	HTPO $_{T1b}$	$\sigma_x \tau_x(L/2)$	Preturbulent regime.
One-Vortex PO from LAN	DPO $_{T1a}$	conjugated to $\sigma_x \sigma_y$	Preturbulent regime. Conjugation is by streamwise translation τ_x .
RPOs possibly bifurcated from DPO family	DRPO $_{T1a,b,c}$	\mathbb{I}	Preturbulent regime.
Two-Vortex PO from LAN	PO $_{T2a}$	conjugated to $\sigma_x \sigma_y \tau_x(L/2)$	Preturbulent regime. Conjugation is by streamwise translation τ_x .
Homoclinic-like RPO	$T2/1, T2/15, T2/18, T2/7$	$\tau_x(L/2)$	Turbulent regime. Probable origin: HRPO $_{T2a}$ while breaking $\sigma_x \tau_x(L/4)$ symmetry
Vortex lattice RPO	$T2/9, T2/30, T2/4, T2/24, T2/13, T2/25$	$\tau_x(L/2)$	Turbulent regime. Probable origin: PO $_{T2a}$ while breaking $\sigma_x \sigma_y$ symmetry

3. Shadowing in Turbulent Regime: Additional information

Table VI: Top 10 ECS groups ranked by frequency of minimum distance occurrences of trajectory $X(t)$. These groups cover approximately 62% of all minimum distance instances.

ECS Group	Freq.	Rel. Freq.	Cum. Freq.	Cum. %	Min Min Dist.	Max Min Dist.	Avg Min Dist.	Region
T2/1	257	0.103	257	0.103	0.119	0.940	0.465	blue/red
T2/15	204	0.082	461	0.184	0.070	0.809	0.331	blue/red
T2/9	181	0.072	642	0.257	0.113	0.770	0.396	green
T2/7	161	0.064	803	0.321	0.256	1.132	0.561	blue/red
T2/18	134	0.054	937	0.375	0.139	1.056	0.513	blue/red
T2/30	134	0.054	1071	0.428	0.203	0.607	0.341	green
T2/4	133	0.053	1204	0.481	0.154	0.761	0.329	green
T2/24	118	0.047	1322	0.529	0.244	0.648	0.394	green
T2/13	116	0.046	1438	0.575	0.207	0.835	0.396	green
T2/25	110	0.044	1548	0.619	0.153	0.807	0.412	green

Table VII: Top 15 ECS groups ranked by frequency of minimum distance occurrences of trajectory $Y(t)$. These groups cover approximately 62% of all ‘closest approach’ instances.

Trajectory ID	Freq. Rel.	Freq. Cum.	Freq. Cum. %	Min Min Dist.	Max Min Dist.	Avg Min Dist.	Region
T1/6	167	0.067	167	0.067	0.308	1.046	0.593 blue/red
T1/3	158	0.063	325	0.130	0.243	1.011	0.611 green
T1/11	158	0.063	483	0.193	0.306	0.996	0.678 blue/red
T1/18	144	0.058	627	0.251	0.399	1.027	0.662 blue/red
T1/23	113	0.045	740	0.296	0.572	1.039	0.790 green
T1/24	108	0.043	848	0.339	0.533	1.010	0.742 green
T1/17	101	0.040	949	0.379	0.465	0.965	0.694 blue/red
T1/2	99	0.040	1048	0.419	0.393	1.009	0.660 green
T1/37	85	0.034	1133	0.453	0.299	0.955	0.652 blue/red
T1/21	78	0.031	1211	0.484	0.556	1.011	0.782 green
T1/25	77	0.031	1288	0.515	0.489	1.036	0.724 green
T1/13	74	0.030	1362	0.545	0.539	1.104	0.772 green
T1/33	71	0.028	1433	0.573	0.424	0.879	0.624 blue/red
T1/29	61	0.024	1494	0.597	0.596	0.927	0.742 green
T1/27	59	0.024	1553	0.621	0.320	0.870	0.610 blue/red

Table VIII: PCA results comparing the two trajectories embedded in chaotic sets \mathcal{X} and \mathcal{Y} , respectively

PCA Metric	$X(t)$	$Y(t)$
Number of time steps analyzed	2501	2501
Number of components explaining 90% variance	4	8
Number of components explaining 95% variance	6	12
Total number of components (time points)	2501	2501
Variance explained by PC1 (%)	60.37	28.41
Variance explained by PC2 (%)	24.40	18.11
Variance explained by PC3 (%)	4.28	16.01
Variance explained by PC4 (%)	4.13	15.32
Variance explained by PC5 (%)	1.61	3.62
Variance explained by PC6 (%)	1.25	3.05

REFERENCES

- [1] S. Ramaswamy, Active fluids, *Nature Reviews Physics* **1**, 640 (2019).
- [2] C. Kurzthaler, L. Gentile, and H. A. Stone, *Out-of-equilibrium Soft Matter: Active Fluids* (Royal Society of Chemistry, 2023).
- [3] R. Alert, J. Casademunt, and J.-F. Joanny, Active turbulence, *Annual Review of Condensed Matter Physics* **13**, 143 (2022).
- [4] A. Doostmohammadi, T. N. Shendruk, K. Thijssen, and J. M. Yeomans, Onset of meso-scale turbulence in active nematics, *Nature Communications* **8**, 10.1038/ncomms15326 (2017).
- [5] M. C. Marchetti, J. F. Joanny, S. Ramaswamy, T. B. Liverpool, J. Prost, M. Rao, and R. A. Simha, Hydrodynamics of soft active matter, *Reviews of Modern Physics* **85**, 1143 (2013).
- [6] M. Varghese, *Active Nematics in Three Dimensions A Dissertation Presented to The Faculty of the Graduate School of Arts and Sciences*, Ph.D. thesis, Brandeis University (2021).
- [7] M. Golden, R. O. Grigoriev, J. Nambisan, and A. Fernandez-Nieves, Physically informed data-driven modeling of active nematics, *Science Advances* **9** (2023).
- [8] C. Joshi, S. Ray, L. M. Lemma, M. Varghese, G. Sharp, Z. Dogic, A. Baskaran, and M. F. Hagan, Data-driven discovery of active nematic hydrodynamics, *Physical Review Letters* **129**, 258001 (2022).
- [9] T. N. Shendruk, A. Doostmohammadi, K. Thijssen, and J. M. Yeomans, Dancing disclinations in confined active nematics, *Soft Matter* **13**, 3853 (2017).
- [10] M. Hillebrand and R. Alert, Discontinuous transition to active nematic turbulence, arXiv preprint arXiv:2501.06085 (2025).
- [11] R. Aditi Simha and S. Ramaswamy, Hydrodynamic fluctuations and instabilities in ordered suspensions of self-propelled particles, *Phys. Rev. Lett.* **89**, 058101 (2002).
- [12] G. Duclos, C. Blanch-Mercader, V. Yashunsky, G. Salbreux, J.-F. Joanny, J. Prost, and P. Silberzan, Spontaneous shear flow in confined cellular nematics, *Nature Physics* **14**, 728 (2018).
- [13] L. Giomi, L. Mahadevan, B. Chakraborty, and M. Hagan, Banding, excitability and chaos in active nematic suspensions, *Nonlinearity* **25**, 2245 (2012).
- [14] F. Mori, S. Bhattacharyya, J. M. Yeomans, and S. P. Thampi, Viscoelastic confinement induces periodic flow reversals in active nematics, *Physical Review E* **108**, 064611 (2023).
- [15] L. Ohm and M. J. Shelley, Weakly nonlinear analysis of pattern formation in active suspensions, *Journal of Fluid Mechanics* **942**, A53 (2022).
- [16] I. Lavi, R. Alert, J.-F. Joanny, and J. Casademunt, Nonlinear spontaneous flow instability in active nematics, *Physical Review Letters* **134**, 238301 (2025).
- [17] J. Walton, G. McKay, M. Grinfeld, and N. J. Mottram, Pressure-driven changes to spontaneous flow in active nematic liquid crystals, *European Physical Journal E* **43**, 10.1140/epje/i2020-11973-8 (2020).
- [18] B. Martínez-Prat, J. Ignés-Mullol, J. Casademunt, and F. Sagués, Selection mechanism at the onset of active turbulence, *Nature physics* **15**, 362 (2019).
- [19] Z. You, A. Baskaran, and M. C. Marchetti, Nonreciprocity as a generic route to traveling states, *Proceedings of the National Academy of Sciences* **117**, 19767 (2020).
- [20] F. Brauns and M. C. Marchetti, Nonreciprocal pattern formation of conserved fields, *Physical Review X* **14**, 021014 (2024).
- [21] R. Alert, J.-F. Joanny, and J. Casademunt, Universal scaling of active nematic turbulence, *Nature Physics* **16**, 682 (2020).
- [22] L. Giomi, Geometry and topology of turbulence in active nematics, *Phys. Rev. X* **5**, 031003 (2015).
- [23] M. Linkmann, M. C. Marchetti, G. Boffetta, and B. Eckhardt, Condensate formation and multiscale dynamics in two-dimensional active suspensions, *Phys. Rev. E* **101**, 022609 (2020).
- [24] S. P. Thampi, Channel confined active nematics, *Current Opinion in Colloid & Interface Science* , 101613 (2022).
- [25] R. J. Henshaw, O. G. Martin, and J. S. Guasto, Dynamic mode structure of active turbulence, *Physical Review Fluids* **8**, 023101 (2023).
- [26] C. G. Wagner, M. M. Norton, J. S. Park, and P. Grover, Exact coherent structures and phase space geometry of preturbulent 2d active nematic channel flow, *Physical Review Letters* **128**, 10.1103/PhysRevLett.128.028003 (2022).
- [27] C. G. Wagner, R. H. Pallock, J. S. Park, M. M. Norton, and P. Grover, Exploring regular and turbulent flow states in active nematic channel flow via exact coherent structures and their invariant manifolds, *Physical Review Fluids* **8**, 10.1103/PhysRevFluids.8.124401 (2023).
- [28] E. Hopf, A mathematical example displaying features of turbulence, *Commun. Pure Appl. Math.* **1**, 303 (1948).

- [29] D. Ruelle and F. Takens, On the nature of turbulence, *Les rencontres physiciens-mathématiciens de Strasbourg-RCP25* **12**, 1 (1971).
- [30] M. D. Graham and D. Floryan, Exact coherent states and the nonlinear dynamics of wall-bounded turbulent flows, *Annu. Rev. Fluid Mech.* **53** (2020).
- [31] C. J. Crowley, J. L. Pughe-Sanford, W. Toler, M. C. Krygier, R. O. Grigoriev, and M. F. Schatz, Turbulence tracks recurrent solutions, *Proceedings of the National Academy of Sciences of the United States of America* **119**, e2120665119 (2022).
- [32] M. Golubitsky and I. Stewart, *The Symmetry Perspective: From Equilibrium to Chaos in Phase Space and Physical Space*, Vol. 200 (Birkhäuser Verlag, 2002).
- [33] A. Marzorati and S. Turzi, Bifurcation analysis of spontaneous flows in active nematic fluids, *Journal of Physics A: Mathematical and Theoretical* **56**, 10.1088/1751-8121/ace408 (2023).
- [34] L. Giomi, L. Mahadevan, B. Chakraborty, and M. F. Hagan, Banding, excitability and chaos in active nematic suspensions, *Nonlinearity* **25**, 2245 (2012).
- [35] S. P. Thampi, R. Golestanian, and J. M. Yeomans, Vorticity, defects and correlations in active turbulence, *Philosophical Transactions of the Royal Society A: Mathematical, Physical and Engineering Sciences* **372**, 10.1098/rsta.2013.0366 (2014).
- [36] C. Wagner and P. Grover, <https://github.com/DynamicalSystemsLab-UNL/ECSAct> (2022).
- [37] K. J. Burns, G. M. Vasil, J. S. Oishi, D. Lecoanet, and B. P. Brown, Dedalus: A flexible framework for numerical simulations with spectral methods, *Phys. Rev. Res.* **2**, 023068 (2020).
- [38] D. Viswanath, Recurrent motions within plane Couette turbulence, *J. Fluid. Mech.* **580**, 339 (2007).
- [39] C. Doré, *Active nematic films under confinement: harnessing topological defects, shaping active flows and designing autonomous microfluidic machines*, Phd thesis, Université Paris sciences et lettres, Paris, France (2022), nNT: 2022UPSLS066, tel-04080803.
- [40] D. Nishiguchi, S. Shiratani, K. A. Takeuchi, and I. S. Aranson, Vortex reversal is a precursor of confined bacterial turbulence, *Proceedings of the National Academy of Sciences* **122**, e2414446122 (2025).
- [41] G. A. Glatzmaier, R. S. Coe, L. Hongre, and P. H. Roberts, The role of the earth's mantle in controlling the frequency of geomagnetic reversals, *Nature* **401**, 885 (1999).
- [42] F. F. Araujo, S. Grossmann, and D. Lohse, Wind reversals in turbulent rayleigh-bénard convection, *Physical Review Letters* **95**, 084502 (2005).
- [43] J. Sommeria, Experimental study of the two-dimensional inverse energy cascade in a square box, *Journal of Fluid Mechanics* **170**, 139 (1986).
- [44] R. Yang and P. J. Schmid, Complex-network modeling of reversal events in two-dimensional turbulent thermal convection, *Journal of Fluid Mechanics* **1011**, 10.1017/jfm.2025.371 (2025).
- [45] G. Ahlers, S. Grossmann, and D. Lohse, Heat transfer and large scale dynamics in turbulent rayleigh-bénard convection, *Reviews of modern physics* **81**, 503 (2009).
- [46] P. K. Mishra, A. K. De, M. K. Verma, and V. Eswaran, Dynamics of reorientations and reversals of large-scale flow in rayleigh-bénard convection, *Journal of Fluid Mechanics* **668**, 480 (2011).
- [47] K. Bai, D. Ji, and E. Brown, Ability of a low-dimensional model to predict geometry-dependent dynamics of large-scale coherent structures in turbulence, *Physical Review E* **93**, 023117 (2016).
- [48] M. Krupa, Robust heteroclinic cycles, *Journal of Nonlinear Science* **7**, 129 (1997).
- [49] T. Kreilos, G. Veble, T. M. Schneider, and B. Eckhardt, Edge states for the turbulence transition in the asymptotic suction boundary layer, *Journal of Fluid Mechanics* **726**, 100 (2013).
- [50] D. Armbruster, J. Guckenheimer, and P. Holmes, Heteroclinic cycles and modulated travelling waves in systems with $o(2)$ symmetry, *Physica D: Nonlinear Phenomena* **29**, 257 (1988).
- [51] P. Holmes, Symmetries, heteroclinic cycles and intermittency in fluid flow, in *Turbulence in Fluid Flows: A Dynamical Systems Approach* (Springer, 1993) pp. 49–58.
- [52] W. S. Koon, M. W. Lo, J. E. Marsden, and S. D. Ross, Heteroclinic connections between periodic orbits and resonance transitions in celestial mechanics, *Chaos: An Interdisciplinary Journal of Nonlinear Science* **10**, 427 (2000).
- [53] F. Gabern, W. Koon, J. E. Marsden, S. Ross, and T. Yanao, Application of tube dynamics to non-statistical reaction processes, *Few-Body Systems* **38**, 167 (2006).
- [54] B. Suri, Predictive framework for flow reversals and excursions in turbulence, *Physical Review Letters* **133**, 10.1103/PhysRevLett.133.154002 (2024).

- [55] J. Jimenez and A. N. D. P. Moin, *The minimal flow unit in near-wall turbulence*, Tech. Rep. (1991).
- [56] G. Kawahara, M. Uhlmann, and L. V. Veen, The significance of simple invariant solutions in turbulent flows, *Annual Review of Fluid Mechanics* **44**, 203 (2011).
- [57] P. Chossat and R. Lauterbach, *Methods in Equivariant Bifurcations and Dynamical Systems*, Vol. 15 (World Scientific Publishing Co. Pte. Ltd., 2000).
- [58] R. Hoyle, *Pattern Formation: An introduction to methods* (University Press, Cambridge, 2006).
- [59] P. Cvitanović, C. R. Artuso, R. M. Gregor, and T. G. Vattay, *Chaos: Classical and Quantum*, Tech. Rep. (2024).
- [60] A. Opathalage, M. M. Norton, M. P. Juniper, B. Langeslay, S. A. Aghvami, S. Fraden, and Z. Dogic, Self-organized dynamics and the transition to turbulence of confined active nematics, *Proceedings of the National Academy of Sciences of the United States of America* **116**, 4788 (2019).
- [61] R. Ramaswamy and F. Jülicher, Activity induces traveling waves, vortices and spatiotemporal chaos in a model actomyosin layer, *Scientific Reports* **6**, 10.1038/srep20838 (2016).
- [62] L. Giomi, L. Mahadevan, B. Chakraborty, and M. F. Hagan, Excitable patterns in active nematics, *Physical Review Letters* **106**, 10.1103/PhysRevLett.106.218101 (2011).
- [63] M. Krupa, Bifurcations of relative equilibria, *SIAM journal on Mathematical Analysis* **21**, 1453 (1990).
- [64] V. Guillemin and A. Pollack, *Differential topology*, Vol. 370 (American Mathematical Society, 2025).
- [65] S. H. Strogatz, *Nonlinear dynamics and chaos: with applications to physics, biology, chemistry, and engineering* (Chapman and Hall/CRC, 2024).
- [66] M. Dellnitz and C. Heinrich, Admissible symmetry increasing bifurcations, *Nonlinearity* **8**, 1039 (1995).
- [67] P. Chossat and M. Golubitsky, Symmetry-increasing bifurcation of chaotic attractors, *Physica D: Nonlinear Phenomena* **32**, 423 (1988).
- [68] A. J. Tan, E. Roberts, S. A. Smith, U. A. Olvera, J. Arteaga, S. Fortini, K. A. Mitchell, and L. S. Hirst, Topological chaos in active nematics, *Nature Physics* **15**, 1033 (2019).
- [69] B. Klein, A. J. S. Franco, M. M. H. Sabbir, M. J. Deutsch, R. Kliegman, R. L. Selinger, K. A. Mitchell, and D. A. Beller, Spontaneous optimal mixing via defect-vortex coupling in confined active nematics, *arXiv preprint arXiv:2503.10880* (2025).
- [70] K. A. Mitchell, M. M. H. Sabbir, K. Geumhan, S. A. Smith, B. Klein, and D. A. Beller, Maximally mixing active nematics, *Physical Review E* **109**, 10.1103/PhysRevE.109.014606 (2024).
- [71] M. Kness, L. S. Tuckerman, and D. Barkley, Symmetry-breaking bifurcations in one-dimensional excitable media, *Physical Review A* **46**, 5054 (1992).
- [72] M. C. Krygier, J. L. Pughe-Sanford, and R. O. Grigoriev, Exact coherent structures and shadowing in turbulent Taylor-Couette flow, *Journal of Fluid Mechanics* **923**, 10.1017/jfm.2021.522 (2021).
- [73] C. J. Crowley, J. L. Pughe-Sanford, W. Toler, R. O. Grigoriev, and M. F. Schatz, Observing a dynamical skeleton of turbulence in Taylor-Couette flow experiments, *Philosophical Transactions of the Royal Society A: Mathematical, Physical and Engineering Sciences* **381**, 10.1098/rsta.2022.0137 (2023).
- [74] B. Suri, L. Kageorge, R. O. Grigoriev, and M. F. Schatz, Capturing turbulent dynamics and statistics in experiments with unstable periodic orbits, *Physical Review Letters* **125**, 064501 (2020).
- [75] G. Yalniz, B. Hof, and N. B. Budanur, Coarse graining the state space of a turbulent flow using periodic orbits, *Physical Review Letters* **126**, 244502 (2021).
- [76] J. Page, P. Norgaard, M. P. Brenner, and R. R. Kerswell, Recurrent flow patterns as a basis for two-dimensional turbulence: predicting statistics from structures, *Proceedings of the National Academy of Sciences* **121**, e2320007121 (2024).
- [77] Z. Krajnik, Z. Kos, and M. Ravnik, Spectral energy analysis of bulk three-dimensional active nematic turbulence, *Soft Matter* **16**, 9059 (2020).
- [78] P. Cvitanović and B. Eckhardt, Symmetry decomposition of chaotic dynamics, *Nonlinearity* **6**, 277 (1993).
- [79] A. J. Linot and M. D. Graham, Dynamics of a data-driven low-dimensional model of turbulent minimal Couette flow, *Journal of Fluid Mechanics* **973**, A42 (2023).
- [80] P. Beck, J. P. Parker, and T. M. Schneider, Machine-aided guessing and gluing of unstable periodic orbits, *arXiv preprint arXiv:2409.03033* (2024).
- [81] J. Page, Computation of simple invariant solutions in fluid turbulence with the aid of deep learning: J. page, *Nonlinear dynamics*, 1 (2025).